

SEIRA optofluidics of sub-monolayers of biomolecules in nL-volumes

vorgelegt von
M. Sc. Physik
Christoph Andreas Kratz
geboren in Hamburg

von der Fakultät II — Mathematik und Naturwissenschaften
der Technischen Universität Berlin
zur Erlangung des akademischen Grades
Doctor rerum naturalium
(Dr. rer. nat.)

genehmigte Dissertation

Promotionsausschuss:

Vorsitzender: Prof. Dr. rer. nat. Peter Hildebrandt

1. Gutachter: Prof Dr. rer. nat. Norbert Esser
2. Gutachter: PD Dr. rer. nat. Karsten Hinrichs
3. Gutachter: Prof Dr. rer. nat. Joachim Heberle

Tag der wissenschaftlichen Aussprache: 26.11.2018

Berlin 2019

To my wonderful wife and children.

Abstract

Optofluidics enables one to analyze minute amount of samples and facilitates new ways in the analysis of biological samples which are often only available in small amounts and should be used as economically as possible. The integration of *in situ* IR spectroscopy for the detection in optofluidics however is in a very early stage. In particular integration of SEIRA spectroscopy with metal island film substrates in optofluidics has not been reported yet. A flavor for the application potential of the technique is presented by a variety of performed studies with *in situ* IR and SEIRA spectroscopy of protein secondary structures and changes therein, protein aggregates, cells, (bio-) functional surfaces and ultrathin films.

This thesis presents research and the invention of a novel concept of an optofluidic platform for *in situ* SEIRA spectroscopy, which illustrates that highly sensitive measurements in nL sample volumes with sub-monolayer sensitivity is feasible. The formations of self-assembled monolayers (SAMs) of the molecules 4-mercaptobenzonitrile and glutathione have been studied as model systems allowing one to determine adsorption kinetics. Sub-monolayer coverage down to a limit of detection of less than 15 ng/cm² can be monitored with a time resolution of minutes for a whole spectrum, corresponding to a limit of detection mass of only a few picograms of material in the detection area. The possibility to measure the dissociation/protonation of a 1.2 nm thick monolayer of glutathione in response to a change in the environmental pH could be shown for the steady-state as well as for the dynamics of the protonation process. The binding and the kinetics of the recognition of streptavidin on a biotinylated enhancement substrate was investigated as a model system for protein analysis. Experimental *in situ* SEIRA spectra showed that the vibrational signatures of amide I and amide II and changes thereof can be assessed during the adsorption process. These vibrational bands can be used to obtain information on the secondary structure of the protein and possible changes in the structure in response to the binding process.

Different aspects concerning the employed enhancement substrates of metal island films have been investigated in the pursuit of the development of the optofluidic platform. Substrates with a gradient in gold film thickness have been utilized to study the correlation between morphology, enhancement and optical properties of different island films on a single substrate. Such substrates allow one to reduce the influences of substrate properties, pre-treatment, deposition and functionalization in the analysis of different morphologies. The possibility for an *a priori* quantification of the enhancement, independent of the molecule of interest, by analyzing the vibrational signature of the native oxide of the silicon substrate has been examined. The analysis indicated a correlation between the enhancement of the vibrational signature and the enhancement of the vibrational bands. Furthermore a novel route to obtain surface functionalization of enhancement substrates by the formation of hybrid substrates has been investigated, pairing functionalized graphene and gold island film substrates. The conservation of the enhancement properties of the substrate after the transfer process could be shown and the substrates were successfully applied in *ex situ* and *in situ* experiments.

The results of this thesis illustrate the research possibilities of the novel developed concept for integrating *in situ* SEIRA spectroscopy in optofluidics. The obtained vibrational fingerprint of the molecules gives access to rich information which in combination with optical modeling and simulation will in the future enable one to investigate a myriad of different processes as protein-protein interaction, receptor-ligand binding or processes in lipid-membranes. The concept may also be of interest in the development of future structure sensitive sensing concepts, where in addition to the identification and quantification of a protein also its secondary structure can be analyzed.

Zusammenfassung

Anwendungen im Bereich der Optofluidik ermöglichen durch die Integration optischer Messmethoden mit mikrofluidischen Komponenten das große Potential dieser Methoden für die Analyse kleinste Probenmengen im sub- μL -Bereich nutzbar zu machen. Dies ist insbesondere für die Analyse von biologischen Proben von hoher Relevanz, welche oft nur in kleinen Mengen verfügbar sind und so sparsam wie möglich eingesetzt werden sollten, und ermöglicht die Entwicklung neuartiger Ansätze und Methoden in diesem Bereich. Die Integration der *in situ* Infrarot (IR) Spektroskopie als Detektionstechnik in der Optofluidik fand hierbei auf Grund unterschiedlicher Herausforderungen in der Umsetzung solcher Konzepte bisher jedoch nur eine geringe Resonanz trotz der hohen Informationstiefe die diese Methode bieten könnte. Insbesondere der Einsatz von signalverstärkenden Konzepten wie der oberflächenverstärkten Infrarot (SEIRA) Spektroskopie mit Metall-Insellfilm-Substraten, welche hochempfindliche Messungen erlauben würden, wurde bisher nicht realisiert. Ein Eindruck des Anwendungspotentials der optofluidischen IR und SEIRA Spektroskopie für die Untersuchung der Sekundärstruktur von Proteinen und deren Änderung, Proteinaggregate, Zellen und der Eigenschaften von biofunktionale Oberflächen und ultra-dünnen Filmen kann aus einer Vielzahl von durchgeführten Studien an makroskopischen Flusszellen gewonnen werden.

Diese Arbeit präsentiert das neuartige Konzept einer optofluidischen Plattform für die *in situ* SEIRA Spektroskopie mit der hochsensitive Messungen mit sub-monolagen Empfindlichkeit in nL Probenvolumen ermöglicht werden. Die selbstorganisierte Formierung von Monolagen und deren Kinetik wurde für die Modellmoleküle 4-Mercaptobenzonitril und Glutathion untersucht. Eine Empfindlichkeit für Sub-Monolagen-Bedeckungen der Oberfläche konnte auf einer Zeitskala von Minuten für die Aufnahme eines gesamten Spektrums bis zu einer Nachweisgrenze von 15 ng/cm^2 gezeigt werden. Diese Nachweisgrenze entspricht einer mit der Detektionsfläche gewichteten Nachweisgrenze von wenigen Picogramm des nachzuweisenden Moleküls. Die Möglichkeit die Dissoziation/Protonierung einer 1.2 nm dicken Monolage von Glutathion in Folge einer Veränderung des pH Wertes der Umgebung der Monolage zu messen, konnte sowohl im Gleichgewichtszustand als auch für die Dynamik der Protonierung gezeigt werden. Der Nachweis sowie eine Untersuchung der Anbindungskinetik von Streptavidin an eine Biotin-funktionalisierte Verstärkungsfläche diente als Modellsystem für die Analyse von Proteinen. Die gemessenen *in situ* SEIRA Spektren zeigten, dass die Schwingungssignatur der Amide I und Amide II Banden und Veränderungen derselbigen während des Adsorptionsprozesses detektiert werden können. Diese Vibrationsbanden können verwendet werden, um Informationen über die Sekundärstruktur des Proteins und mögliche Veränderungen dieser Struktur als Folge des Adsorptionsprozesses zu untersuchen.

Für die Entwicklung der optofluidischen Plattform wurden unterschiedliche Eigenschaften der eingesetzten Metall-Insellfilm-Substrate, die als Verstärkungssubstrate verwendet wurden, untersucht. Substrate mit einem Gradienten in der Dicke des Goldfilmes wurden verwendet um die Korrelation zwischen der Morphologie, der Verstärkung und den optischen Eigenschaften verschiedener Insellfilme auf einem einzigen Substrate zu untersuchen. Solch ein Substrat erlaubt es hierbei die Einflüsse der Substrateigenschaften, der Vorbehandlung, der Deposition und der Funktionalisierung in der Untersuchung der unterschiedlichen Morphologie zu verringern. Die Möglichkeit einer *a priori* Quantifizierung der Verstärkung, unabhängig vom Zielmolekül, mittels der Analyse der Schwingungssignatur des nativen Oxids wurde untersucht. Hierbei konnte ein Anhaltspunkt für eine Korrelation zwischen der Verstärkung der Schwingungssignatur des nativen Oxids und der Verstärkung der Schwingungsbanden von organischen Molekülen gefunden werden. Des Weiteren wurde eine neue Möglichkeit der Oberflächenfunktionalisierung von Verstärkungssubstraten, durch die Formierung eines Hybridsubstrates durch den Transfer von funktionalisiertem Graphen auf Gold-Insellfilm-Substraten, untersucht. Hierbei konnte die Erhaltung der Verstärkungseigenschaften nach dem Transfer so wie die Anwendung in *ex situ* und *in situ* Experimenten gezeigt werden.

Zusammenfassung

Die Ergebnisse dieser Arbeit zeigen die Möglichkeiten des entwickelten Konzeptes für die Integration der SEIRA Spektroskopie in der Optofluidik auf. Die gemessenen IR Spektren der Moleküle ermöglichen einen Zugang zu einer Vielzahl an Informationen, welche in Kombination mit optischen Modellen und Simulationen in der Zukunft die Möglichkeit eröffnen unterschiedlichen Prozessen wie Protein-Protein Wechselwirkungen, Rezeptor-Ligand Bindungen oder Prozesse in Lipid-Membranen zu untersuchen. Darüber hinaus kann das vorgestellte Konzept auch einen Beitrag in der Entwicklung zukünftiger Struktur-sensitiver Sensorkonzepten leisten, welche neben der Identifizierung und Quantifizierung von Proteinen auch einen Zugang zu Informationen über die Sekundärstruktur bieten.

List of publications

Parts of this work are published in the following articles and are reprinted with permission:

- Furchner, A., Kratz, C., Gkogkou, D., Ketelsen, H., & Hinrichs, K. Infrared-spectroscopic single-shot laser mapping ellipsometry: Proof of concept for fast investigations of structured surfaces and interactions in organic thin films. (2017) *Applied Surface Science*. 421: 440-445 DOI: 10.1016/j.apsusc.2016.08.140
- Kratz, C., Oates, T. W. H., & Hinrichs, K. Optimization and quantification of surface enhanced infrared absorption using gradient gold island films. (2016) *Thin Solid Films*, 617, 33-37. DOI: 10.1016/j.tsf.2016.02.019
- Janasek, D., Hinrichs, K., Kratz, C., Oates, T. W. H., (2016) Vorrichtung zur Detektion und Charakterisierung von organischen Molekülen in einem flüssigen Probenvolumen. German Patent Proposal: 10 2016 101 001.4, 21.01.2016.
- Rösicke, F., Gluba, M. A., Shaykhutdinov, T., Sun, G., Kratz, C., Rappich, J., Hinrichs, K., & Nickel, N. H., (2017). Functionalization of any substrate using covalently modified large area CVD graphene. *Chemical Communications*, 53(67), 9308-9311. DOI: 10.1039/C7CC03951D
- Hinrichs, K., Shaykhutdinov, T., Kratz, C., Rösicke, F., Schöniger, C., Arenz, C., Nickel, N. H., and Rappich, J., (2018), Electrochemical Modification of Large Area Graphene and Characterization by Vibrational Spectroscopy in *Encyclopedia of Interfacial Chemistry*, ed. K. Wandelt, Elsevier, Oxford, 2018, pp. 80-94.
- Kratz, C., Furchner, A., Oates, T. W. H., Janasek, D., Hinrichs, K., (2018) Nanoliter sensing for IR bioanalytics, (2018) *ACS sensors* 3(2): 299-303. DOI: 10.1021/acssensors.7b00902

Contribution at academic conferences and workshops

- Kratz, C., Oates, T. W. H., Janasek, D. & Hinrichs, K., 'Microfluidic cells in IR-microscopy for biosensing', (2015), 79. DPG Frühjahrstagung, Berlin, Germany, Oral presentation
- Kratz, C., Oates, T. W. H., Janasek, D. & Hinrichs, K., 'Microfluidic cells in IR-microscopy for biosensor applications', (2015), BIOMATSEN - International Congress on Biomaterials and Biosensors, Fethiye, Mugla, Turkey, Oral presentation
- Kratz, C., Oates, T. W. H., Janasek, D. & Hinrichs, K., 'Verstärkungssubstrate für mikrofluidische Anwendungen in der IR-Mikroskopie', (2015), 18. Tagung Festkörperanalytik, Vienna, Austria, Poster presentation
- Kratz, C., Oates, T. W. H., Janasek, D. & Hinrichs, K., 'Gradient gold island films for the optimization and quantification of surface enhanced infrared absorption', (2016), 80. DPG Frühjahrstagung, Regensburg, Germany, Oral presentation
- Kratz, C., Janasek, D. & Hinrichs, K., 'Integration of enhancement substrates and microfluidics in FT-IR microscopy for biosensing', (2016), Biosensors 2016, Göteborg, Sweden, Poster presentation
- Kratz, C., Janasek, D. & Hinrichs, K., 'Integration of enhancement substrates and microfluidic in IR-microscopy for in-situ studies of solid liquid interfaces', (2016), ICSE-7, Berlin, Germany, Poster presentation
- Kratz, C., Gkogkou, D., Rösicke, F., Shaykhutdinov, T., Oates, T. W. H., Furchner, A., Rappich, J., Hinrichs, K., 'Functionalized enhancement biosensor substrates for vibrational spectroscopy applications', (2016) Micro Photonics, Berlin, Germany
- Hinrichs, K., Kroning, A., Shaykhutdinov, T., Kratz, C. & Furchner, A., 'Correlation of IR spectra with thin-film structure at solid water interfaces', (2016), 15th Dresden Polymer Discussion, Dresden, Germany
- Kratz, C., Gkogkou, D., Rösicke, F., Shaykhutdinov, T., Oates, T., Furchner, A., Rappich, J. & Hinrichs, K., 'Functionalized Metallic Island Substrates for Enhanced Raman and IR Microscopic Biosensing', (2017), 15th European Conference on Organized Films (ECOF15), Dresden, Germany
- Rösicke, F., Gluba, M. A., Kratz, C., Shaykhutdinov, T., Nickel, N. H., Rappich, J. & Hinrichs, K., 'Transfer and characterization of covalently modified large area graphene', (2017), DPG Tagung, Dresden, Germany.
- Kratz, C., Oates, T. W. H., Janasek, D. & Hinrichs, K., 'Optofluidic platform for enhanced IR microscopic biosensing', (2017), 11th Workshop on FT-IR Spectroscopy in Microbiological and Medical Diagnostics, Berlin, Germany, Poster presentation
- Gkogkou, D., Kratz, C., Esser, N., Speiser, E. & Hinrichs, K. 'Metal thin films as plasmonic support for surface enhanced vibrational spectroscopy and optofluidics' (2018), 82. DPG-Frühjahrstagung, Berlin, Germany
- Kratz, C., Janasek, D., Rösicke, F., Oates, T., Rappich, J. & Hinrichs, K., 'In-situ nanoliter IR biosensing with hybrid graphene functionalized plasmonic enhancement substrates', (2018), 28th Anniversary World Congress on Biosensors: Biosensors 2018, Miami, USA, poster presentation
- Hinrichs, K., Janasek, D., Oates, T. & Kratz, C., 'Optofluidic platform for enhanced IR microscopic sensing', (2018) Handlungsfeldkonferenz BioMedizinische Optik und Augenoptik Workshop PHOTONICS IN BIOMED - ON - A - CHIP.

Table of content

Abstract	I
Zusammenfassung.....	III
List of publications	V
Contribution at academic conferences and workshops.....	VI
Table of content	VII
1. Motivation: <i>In situ</i> μ l-infrared spectroscopy.....	1
2. Experimental and Theoretical Methods.....	5
2.1. IR microscopy	6
2.2. Ellipsometry.....	8
2.2.1. Fundamentals.....	8
2.2.2. UV-Vis ellipsometry.....	10
2.2.3. IR Ellipsometry.....	10
2.3. Enhancement substrates.....	11
2.3.1. Fundamentals.....	11
2.3.2. Fabrication.....	14
2.3.3. Line shape of vibrational bands in SEIRA spectroscopy	17
2.3.4. Enhancement factor.....	18
2.4. Data analysis & Optical modeling	21
2.4.1. General considerations	21
2.4.2. Direct inversion of ellipsometric measurements	21
2.4.3. Optical simulation	21
2.4.4. Theoretical optical model for metal-island films	24
2.5. Surface preparation & modification.....	29
2.5.1. Self-assembled monolayers (SAM)	29
2.5.2. Transfer of pre-functionalized graphene	32
2.6. Microfluidics.....	33
3. Realization of an optofluidic platform for IR microscopy	36
3.1. Layout of the optofluidic platform.....	37
3.2. Effective measurement area in <i>in situ</i> measurements	38
3.3. Measurements with the optofluidic platform	39
4. Results & Discussion.....	41
4.1. Enhancement substrates.....	42
4.1.1. Correlation between island film morphology and enhancement properties of metal island film substrates.....	43
4.1.2. <i>A priori</i> quantification of SEIRA enhancement.....	48

Table of content

4.1.3.	Self-assembled monolayer formation on contaminated surfaces	53
4.1.4.	Plasmonic resonance shift by monolayer adsorption	56
4.1.5.	Optical modeling of <i>ex situ</i> SEIRA reflectivity spectra.....	58
4.2.	<i>In situ</i> IR microscopy in microfluidic volumes	63
4.2.1.	Online <i>in situ</i> reaction monitoring.....	63
4.2.2.	<i>In situ</i> monitoring of monolayer assembly with SEIRA spectroscopy	66
4.2.3.	<i>In situ</i> study of changes in the ionization state of glutathione dissociation in dependence on environmental pH.....	70
4.2.4.	<i>In situ</i> study of surface immobilization of streptavidin on a biotinylated enhancement substrate	72
4.3.	Hybrid sensor substrates obtained by pairing pre-functionalized graphene with enhancement substrates.....	75
4.3.1.	Characterization of the effect of the graphene on the enhancement properties of the enhancement substrate	76
4.3.2.	Hybrid substrates for <i>ex situ</i> applications	79
4.3.3.	Comparative study of (4-nitrobenzyl) mercaptane binding on gold island film and on p-MP graphene	81
5.	Summary & conclusion.....	85
6.	Outlook	91
	References.....	97
	List of abbreviations	109
	List of figures	111
	List of tables.....	117
	List of chemicals	119
	Acknowledgements	121
	Statement of authorship	123

1. Motivation: *In situ* μ l-infrared spectroscopy

The flourishing field of optofluidics has strongly influenced the development of novel label-free biological sensors and introduced new ideas in the analysis of minute sample volumes.¹⁻⁷ Optofluidic devices combine the advantages of fast, label-free and non-destructive optical detection with the handling possibility of nL to μ L sample volumes of microfluidics.^{1, 3} Different optical detection techniques have been successfully demonstrated as read-out techniques for such devices. Techniques sensitive to refractive index changes of the sensor surface probed by evanescent fields, plasmonics (surface plasmon resonances (SPR) or localized surface plasmon resonances (LSPR)) or with resonant (nano-) cavities have been integrated in optofluidics.⁷ These techniques show highly promising performances down to the single molecule level. However, the sensitivity towards changes in the refractive index may be highly sensitive but in contrast to the approach presented here, it neither allows for the direct identification of the analyte nor provides specific information on the analyte as *e.g.* the secondary structure of a protein or the interaction of the analyte with the sensor surface. These information's, which are accessible by the presented concept, are however potentially highly relevant for investigations of disease mechanism as well as in the analysis of the mode of action of treatments as well as in the research and analysis of drugs and antibiotics. Furthermore the information's provided by the presented concept may be of high relevance in the development of future technologies for personalized medicine as they provide a new access path towards the investigation of molecular interactions.

Vibrational spectroscopy techniques like the complementary techniques of Raman and IR spectroscopy may provide such information by probing the vibrational properties of the analyte.⁸⁻¹¹ Surface enhanced Raman scattering (SERS) has already been successfully demonstrated for the detection in optofluidics also showing high sensitivities.¹²⁻¹⁴ The application of *in situ* infrared (IR) spectroscopy for the detection in optofluidic is however in a very early stage. Existing applications and studies utilizing IR spectroscopy may give a flavor for possible applications of this technique in optofluidics if it can be successfully applied. IR spectroscopy has been employed in the study of protein secondary structures and changes thereof¹⁵⁻²², protein aggregates, cells²³⁻³³ and the analysis of (ultra) thin films³⁴⁻⁵⁰. Its applicability to investigate processes at the solid—liquid interface of (bio-) functional surfaces as *e.g.* adsorption/desorption kinetics^{51, 52} or stimuli dependent changes within the surface has been successfully demonstrated.^{35, 36, 40, 43, 47, 49} With these abilities all the functionalization steps in the preparation of the sensor surface may be individually assessed, giving the possibility to gain an understanding of the underlying interaction processes and elucidating the working principles of the sensor. It may also open up the potential to study protein-protein interactions, receptor-ligand binding and other molecular interactions. Despite this potential only very few examples for the usage of IR spectroscopy on microfluidic devices have been reported in the literature employing either transmission^{33, 53-60} or attenuated total reflection (ATR)⁶¹⁻⁶⁵ geometries for the measurement.

The application of IR spectroscopy in an optofluidic device is complicated by several challenges. On the one hand the high absorption of the mostly aqueous environment of biological samples and that of the polymeric materials used for the microfluidic chips is problematic.⁵³ The absorption strongly limits the application of measurement in transmission geometry as microfluidic chips have to be specifically designed and fabricated from IR transparent materials and the channel depth may not exceed approximately 10 μ m. This challenge can be solved by using either an ATR geometry or by measuring the specular reflection at the solid—liquid interface. On the other hand the sensitivity of IR spectroscopy in specular reflection decreases as the sampling area reaches dimensions compatible with microfluidic channels.

Motivation: In situ μ l-infrared spectroscopy

A way to increase the sensitivity of conventional IR spectroscopy is presented by utilizing the effect of surface enhanced infrared absorption (SEIRA) provided by plasmonic nanostructured surfaces. The SEIRA effect can be used to gain a signal enhancement of 10^1 - 10^3 for metal-island film substrates^{20, 37, 52, 66-76} and can reach enhancement factors of 10^7 for specifically tailored plasmonic nano-antennas.⁷⁷⁻⁸⁶ Metal island films for SEIRA typically have a thickness of a few nm and are compatible to thin film preparation techniques. The metal island film substrates can be treated in the theoretical framework of optical simulations if represented by a suitable optical model. The utilization of metal island films for SEIRA spectroscopy in optofluidics however has not been reported yet.

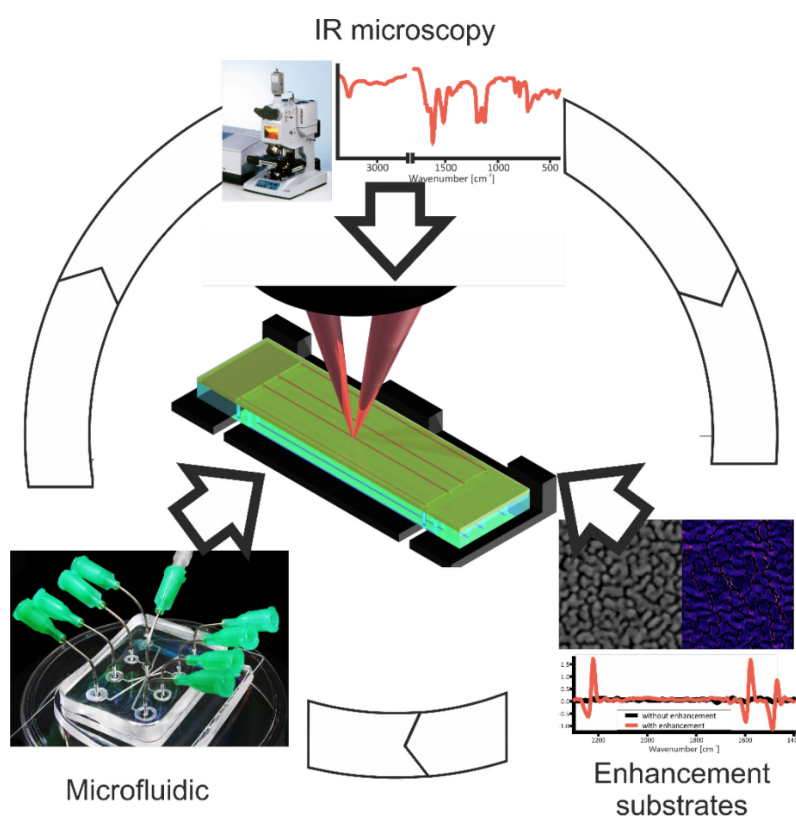


Figure 1-1: General concept of an optofluidic platform for enhanced IR spectroscopy.

The aim of this thesis was therefore to investigate the possibility of applying *in situ* SEIRA spectroscopy for the analysis of nL to μ L sample volumes with sub-monolayer sensitivity for the analysis of processes at the solid—liquid interface.⁸⁷ Model systems have been investigated to show that adsorption kinetics of self-assembled monolayers (SAM) can be determined, chemical changes on the monolayer level can be monitored and protein recognition on functionalized substrate can be achieved. A reproducible limit of detection (LOD) of less than 15 ng/cm^2 and a limit of detection mass (LOD_M) in the range of a few picograms could be demonstrated. For these investigations a novel optofluidic platform was developed which enables the integration of enhancement substrates for surface enhanced IR absorption (SEIRA) spectroscopy with a microfluidic chip (Figure 1-1).

The properties and characteristics of the employed enhancement substrates of gold island films on silicon have been investigated in the pursuit of this development. In particular the possibilities for optimization and pre-assessment of the enhancement have been studied. The correlation of the island film morphology, plasmonic and enhancement properties was investigated using substrates with a gradient in gold layer thickness.⁸⁸ The vibrational signature of the native oxide on the silicon has been investigated for its suitability for an *a priori* determination of the enhancement.

Motivation: In situ μ l-infrared spectroscopy

In the surface functionalization of the enhancement substrates a novel strategy for the formation of hybrid sensor substrates by a transfer of pre-functionalized graphene onto SEIRA templates has been evaluated. Conservation of the enhancement properties of the template and functionality of the hybrid substrates was demonstrated in *ex situ* and *in situ* experiments. In addition, a correlation between the shift in the plasmonic resonance of the substrates and the thickness and optical properties of the absorbed layer has been observed. A comparison between experimental results and results from optical modeling indicated that the analysis of the plasmonic resonance shift may provide a complementary access to sample properties such as film thickness.

An optofluidic platform for highly sensitive SEIRA spectroscopy at the solid—liquid interface using sample volumes in the order of a few μ L or less has a plethora of different applications. Especially in cases where samples are sparsely available as *e.g.* proteins or enzymes isolated from biological samples the low sample consumption is of high interest. The possibility to use microfluidic chips of various design and materials may increase and facilitate the dissemination of the developed concept in the future. The presented concept makes it possible to mimic physiological conditions as *e.g.* flow-conditions or pressure in blood vessels and investigate the effect of *e.g.* flow velocity and molecular concentration on reactions at bio-interfaces like cell membranes. The ability to perform studies under *in situ* conditions will enable one to investigate the influence of external stimuli as *e.g.* changes in environmental conditions or the effect of oxidative stress *e.g.* on the secondary structure of proteins or binding kinetics. Furthermore interactions between molecules as *e.g.* receptor—ligand interactions can potentially be studied. The concept of the optofluidic platform with surface enhanced sensitivity is also ideal to study interactions in lipid membranes and membrane proteins. Conformational changes in the membrane and of the protein secondary structure of ion channels, ligand-gated ion channel transmembrane proteins or the effect of pore-forming toxins may be studied under controlled *in situ* conditions. Moreover all steps in the formation of a biosensor from the preparation of the initial surface functionalization up to the binding of the target molecule can be investigated and evaluated directly in the optofluidic platform. This may open up the possibility to evaluate, develop and optimize *e.g.* novel surface immobilization strategies for applications with other optical detection techniques. Additionally the demonstrated high sensitivity makes the presented platform an interesting candidate for the future development of novel label-free and non-destructive biosensing strategies *e.g.* if the secondary structure of the protein under analysis is of diagnostic interest.

The thesis is divided into six chapters. Following the introduction the second chapter deals with the employed experimental techniques used for measurement and characterization and gives a short theoretical introduction. Topics of enhancement substrates, data analysis and optical modeling, materials and chemical preparation as well as microfluidics are presented. The third chapter presents the developed optofluidic platform. In the fourth chapter the results of the studies performed for the thesis are shown and discussed. The studies aim to show that highly sensitive *in situ* IR and SEIRA spectroscopy on microfluidic volumes can be performed. The fifth chapter summarizes the results and presents the drawn conclusions. In the last chapter an outlook is given which shows some further ideas and possible studies with the presented concept of a SEIRA optofluidic platform.

2. Experimental and Theoretical Methods

This chapter gives an overview and introduction to the experimental and analytical techniques used in this thesis. The first two sections of the chapter introduce IR-microscopy and the general concept of ellipsometry as well as the employed instruments. In the third part enhancement substrates, with a focus on metal-island films, are introduced. A general introduction to the state-of-the-art, the technique used for preparation, different types of substrates, the scheme used for the calculation of the enhancement factor and further aspects of SEIRA spectroscopy are described and discussed. The fourth part introduces the methods used for data analysis and optical modeling. A theoretical model used for the description of the metal island films is presented. In the fifth part the materials and the chemical preparation processes are described. The focus here lies on self-assembled monolayers and the preparation process of novel hybrid sensor substrates by transfer of pre-functionalized graphene to an enhancement substrate templates. The last part of the chapter introduces the employed microfluidic chips and the technique used for their fabrication.

2.1. IR microscopy

IR microscopy enables one to perform IR spectroscopy with a high spatial resolution enabling *e.g.* measurements on individual components of microfluidic chips. Numerous publications and books have been published on the fundamentals and instrumentations of FT-IR spectroscopy, for detailed information see *e.g.* Ref. [9, 89-92]. The IR microscope (Hyperion 3000, Bruker Inc.) used for the measurements is coupled to a Fourier transform (FT)-IR spectrometer (Vertex 70, Bruker Optics GmbH). It employs a Cassegrain-objective (NA = 0.4, spot-size 160 μm x 160 μm) as imaging optics and a liquid nitrogen cooled photovoltaic mercury cadmium telluride (MCT) detector. Measurements can in general be performed in reflection or transmission mode, where the former is solely employed in this thesis.

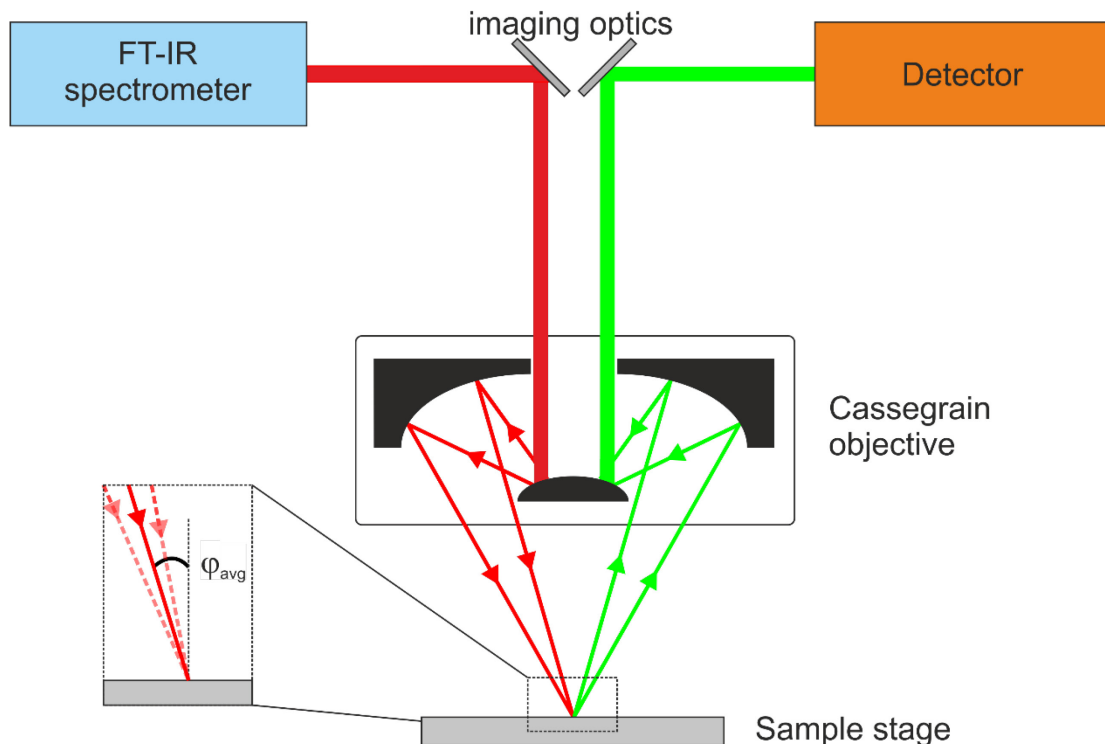


Figure 2-1: Schematic drawing of a FT-IR-microscope using a Cassegrain objective for light focusing

The basic concept of the IR microscope is schematically shown in Figure 2-1. Mirror optics guide the radiation from the FT-IR spectrometer to the Cassegrain objective. The Cassegrain objective utilizes off-axis parabolic mirrors to focus the radiation onto the sample and to collect the radiation reflected from the sample. As a result of the mirror optics and the NA of the objective the range of angles of incidence lies between 10.75° and 23.58°. In simulations of the measurement a median angle of incidence φ_{avg} of 17.12° was assumed.

The IR microscope is equipped with an automated movable x-y-z sample stage which allows for the positioning and mapping of the sample. In order to avoid interference from atmospheric water vapor the microscope has a housed sample compartment which is continuously purged with dry air.

The employed FT-IR spectrometer uses a thermal radiation source of a silicon carbide (SiC) globar to produce the mid IR radiation. The emission profile of the SiC and absorptions from the optical components as well as atmospheric contribution are visible in the single channel spectrum. In order to eliminate these systematic artifacts from the measurement data, measurements are generally performed on the sample and on a reference sample (*e.g.* gold or silicon). The two spectra are divided resulting in a relative or referenced reflectivity spectrum (Figure 2-2).

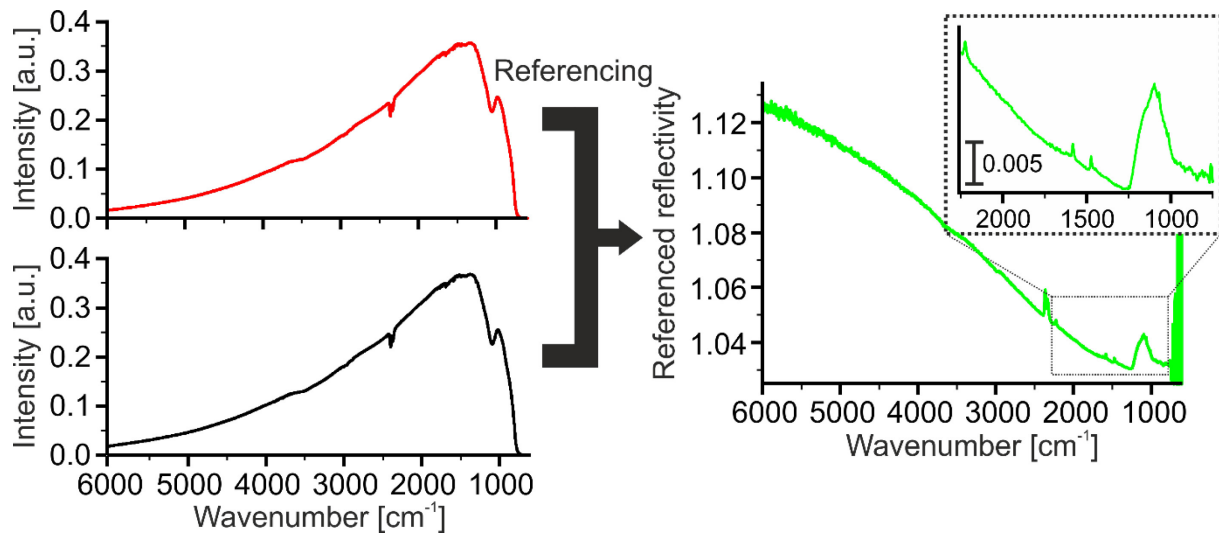


Figure 2-2: Measurement principle of recording relative or referenced reflectivity spectra. (top left) Intensity spectrum recorded on a reference silicon substrate. (bottom left) Intensity spectrum measured on gold island film substrate with an organic SAM of 4-mercaptobenzonitrile. (right) Resulting relative or referenced reflectivity spectrum.

IR spectra are commonly displayed in the units of wavenumber [cm^{-1}] from high wavenumbers to low wavenumbers relating to the energy of the absorbed photon. The unit of wavenumbers is related to the wavelength of the radiation by the relation $\nu[\text{cm}^{-1}] = \frac{10000}{\lambda[\mu\text{m}]} \propto \frac{E[\text{eV}]}{hc}$.

2.2. Ellipsometry

Ellipsometry measures changes in the polarization state of an EM wave when it is reflected from or transmitted through a sample.^{11, 92, 93} It can *e.g.* be used to analyze the film-thicknesses of thin films or in conjunction with optical modeling to gain access to the dielectric properties of the sample enabling further analysis. As an essentially reference free technique it is a powerful tool for characterizing material properties and in combination with optical modeling can be used for quantitative analysis and investigations of interaction processes *e.g.* at the solid—liquid interface.⁹¹

2.2.1. Fundamentals

In order to introduce the principles of ellipsometry and to define the used reference frame a quick introduction on the topic of polarization of electromagnetic waves is beneficial at this point

In ellipsometry it is common to describe the electric field vector \vec{E} of an electromagnetic (EM) wave with respect to the plane of incidence. With this definition the electric field can be expressed as the superposition of two orthogonal components parallel and perpendicular to the plane of incidence denoted with the subscripts p and s respectively^{11, 93}.

$$\vec{E} = \begin{pmatrix} E_{p0} \exp[i(\omega t - kr + \delta_p)] \\ E_{s0} \exp[i(\omega t - kr + \delta_s)] \end{pmatrix} \quad (2-1)$$

Where E_j denotes the amplitude, δ_j the phase of the vector component ($j=p, s$) and ω is the angular frequency of the electric field and r is the propagation direction.

Employing this decomposition of the field into its orthogonal components the ratio of the amplitudes E_{p0}/E_{s0} and the phase difference ($\Delta = \delta_p - \delta_s$) of the EM wave define its state of polarization.

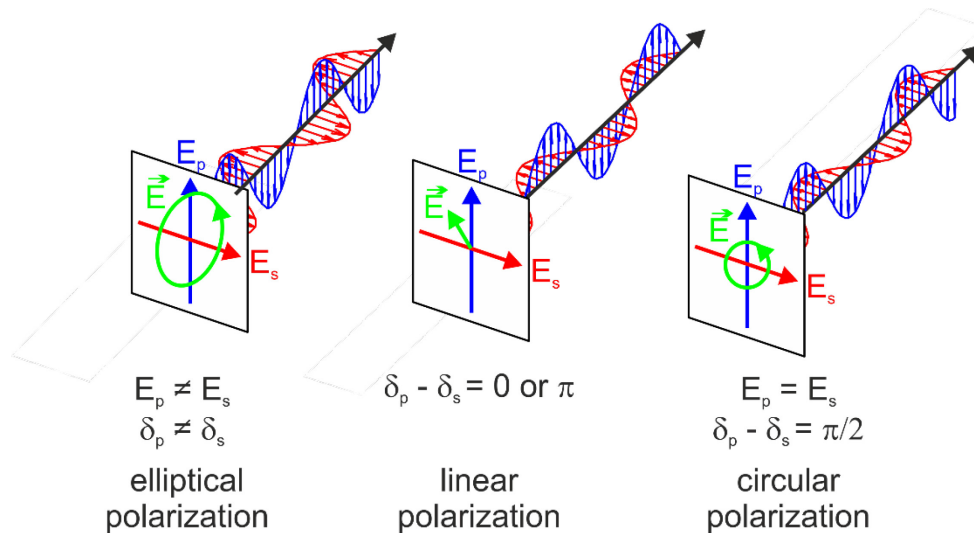


Figure 2-3: Different states of polarizations of an EM wave expressed by its decomposition in E_s and E_p field components, depending on amplitude-ratio E_{p0}/E_{s0} and phase difference ($\Delta = \delta_p - \delta_s$).

As shown in Figure 2-3 the polarization state of the EM wave will in most cases be elliptical. Distinguished states of polarizations are obtained for $\Delta = 0, \pi$ resulting in a linear polarization state and for $\Delta = \pi/2$ and $E_{r0} = E_{s0}$ resulting in a circular polarization state, for all other phase differences and amplitude ratios the radiation will have an elliptical polarization state.

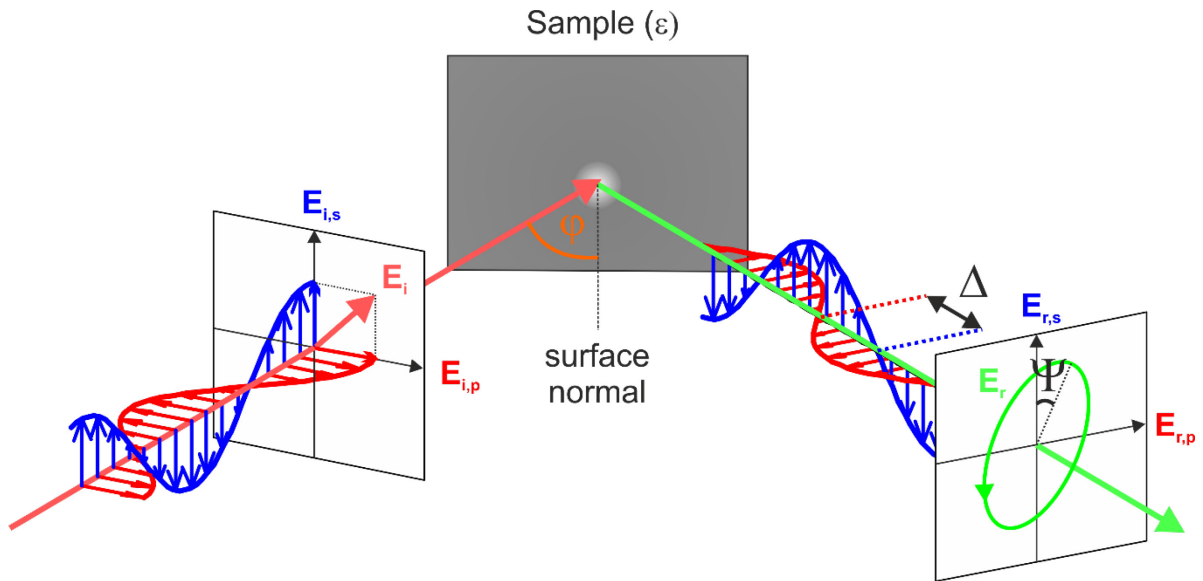


Figure 2-4: Basic principle of ellipsometric measurement. Reflection at an interface changes the polarization state of light in dependence on the dielectric properties ϵ and geometry e.g. film thickness of the sample. Adapted from [34]

The general principle of an ellipsometric measurement is shown in Figure 2-4.

The defined polarization state of an incoming EM wave is altered upon reflection from the surface of a sample in dependence on the thickness, surface structure, layer structure and the individual dielectric properties each layer which form the sample as well as the incidence angle of the radiation.

This change in the polarization state is detected by determining the complex reflectance ratio ρ ^{11, 92, 93}:

$$\rho = \frac{E_{rp}/E_{ip}}{E_{rs}/E_{is}} = \frac{r_p}{r_s} = \tan \Psi \cdot \exp(i\Delta) \quad (2-2)$$

with:

$$\tan \Psi = \frac{|r_p|}{|r_s|} \quad \text{and} \quad \Delta = \delta_p - \delta_s \quad (2-3)$$

r_j ($j = p, s$) are the complex reflection coefficients and δ_j ($j = p, s$) are the phases of the parallel (p) and orthogonal (s) components of the electric field. The ellipsometric parameters $\tan \Psi$ for the change in amplitude and Δ for the change in phase are used to describe the change in polarization state.

There is a manifold of different experimental realizations of ellipsometers.⁹² A common setup, employed in this thesis, is the rotating analyzer setup in a polarizer-sample-compensator-analyzer (PSCA) configuration shown schematically in Figure 2-5.

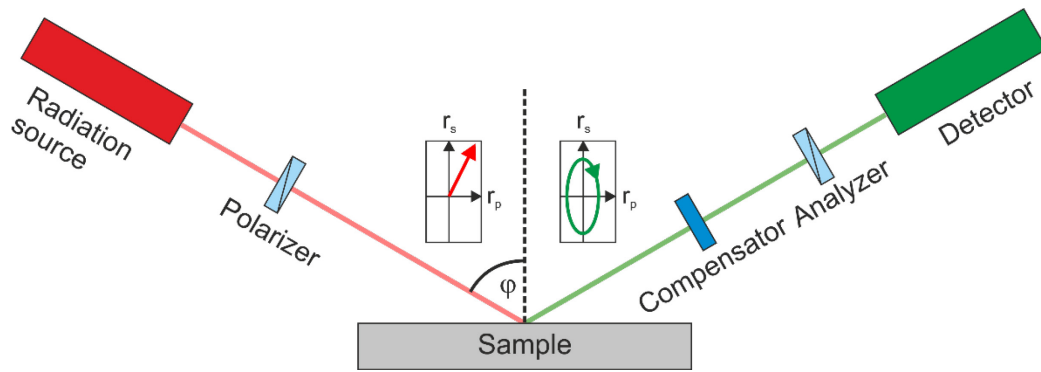


Figure 2-5: Schematic setup of an ellipsometer with a PSCA configuration. The incidence angle of the radiation on the sample is denoted by φ .

The radiation emitted from a radiation source is prepared in a defined linear polarization using a linear polarizer. This radiation is reflected from the sample at a chosen incidence angle φ . The altered state of the polarization is analyzed using a rotatable second linear polarizer called analyzer. A photosensitive detector is used to measure the intensity of the radiation at different relative angles between the polarizer and the analyzer. The recorded intensity at the detector depends on the alignment of the analyzer transmission axis and the altered state of radiation. The compensator which introduces an additional phase shift between r_p and r_s , allows one to obtain a higher sensitivity for Δ -values close to 0° and enables one to define the quadrant of Δ .

2.2.2. UV-Vis ellipsometry

A UV-Vis ellipsometer (Sentech GmbH, Sentech SE 850) was employed for the characterization of the enhancement substrates as well as in reference measurements for the characterization of thin-films of model analytes. The ellipsometer allows the measurement of the ellipsometric parameters $\tan \Psi$ and Δ in the spectral region between 240 nm to 930 nm using the emission of a Xenon lamp for the UV range (240 nm - 400 nm) and a Halogen lamp for the visible range (400 nm - 930 nm) under a variable angle of incidence. The general setup of the ellipsometer is schematically shown in Figure 2-5. If not stated otherwise an angle of incidence of 70° was used for the measurements. The ellipsometer is equipped with an automated sample stage which allows for lateral movement in the x-y-direction and automated mapping of the sample as well as sample rotation, tilting and movement in the z-axis for the alignment. An increased lateral resolution for the characterization of the optical properties on gradient metal island-films is obtained by employing micro-apertures (spot-size $\approx 250 \times 250 \mu\text{m}^2$). Measurements and the analysis/optical modeling of the measurement data have been performed using the commercially available software SpectraRay3 (SENTECH Instruments GmbH).

2.2.3. IR Ellipsometry

IR ellipsometry has been employed to obtain optical constants of model analytes. *Ex situ* measurements have been performed on a custom build IR ellipsometer using a Bruker IFS 55 FT-IR spectrometer. Details on the concept and instrumentation of the used IR ellipsometer can *e.g.* be found in Ref [11, 94]

2.3. Enhancement substrates

Enhancement substrates are a key component for highly sensitive vibrational spectroscopy. In the first part of this section a general introduction will be given to the state of the art of enhancement substrates SEIRA applications and to some further general properties of metal island film substrates. The second part introduces the principle of the fabrication technique employed in this thesis and the different types of substrates that can be realized. In the third part the different line-shapes observed in SEIRA spectroscopy in correspondence to a Fano-like resonance are discussed and in the fourth part the concept used to determine the enhancement factor is presented.

2.3.1. Fundamentals

Introduction

Metamaterials and plasmonic nanostructured surfaces such as metal-island films offer the possibility to considerably enhance sensitivity of vibrational spectroscopy. The field of surface enhanced vibrational spectroscopy can be divided into the complementary techniques of surface enhanced Raman scattering (SERS) and surface enhanced IR absorption (SEIRA). The field of SERS has received large interest due to its very high enhancement factors on the order of $10^6 - 10^{12}$ enabling sensitivities down to single molecule detection.^{95, 96} In comparison enhancement factors obtained in SEIRA spectroscopy with metal island film substrates are orders of magnitude lower reaching factors of $10^1 - 10^3$.^{8, 97, 98} Enhancement factors of up to 10^7 can however be achieved for highly localized enhancement with specifically designed plasmonic nanostructured substrates employing *e.g.* resonant nano-antennas also in combination with perfect absorber structures.^{81, 99-101} The difference in enhancement factors between SERS and SEIRA is partly counter-balanced by the higher absorption cross-section of IR radiation compared to the scattering cross-section in Raman scattering. The IR absorption cross-section is typically in the range of 10^{-20} cm^2 in comparison to the cross sections for Raman scattering on the order of 10^{-28} cm^2 .⁹⁸ In consequence of the complementary nature to Raman spectroscopy and the possibility to use infrared radiation which may be less harmful for biological samples, SEIRA has gained importance in the fields of *e.g.* biology and (bio-) chemistry as well as for chemical and biochemical sensing applications.^{75, 102-105}

Various types of substrates have been presented providing enhanced infrared absorption ranging from electrochemically roughened electrodes,¹⁰⁶ colloidal interfaces and metal island films to precisely designed and highly sophisticated resonant plasmonic nano-antennas fabricated by electron beam or colloidal lithography^{99, 107}. Metal island films as presented in this work may be seen as an intermediate between roughened electrodes and resonant plasmonic nano-antenna substrates. Partial control over island size, geometry, fill factor, density and distribution of the metal islands can be obtained by controlling the deposition parameters. In contrast to specifically engineered resonance of plasmonic nano antennas with spatially and spectrally highly localized enhancement properties, metal island films provide an enhancement over the full area of the substrate and a spectrally broad region of enhancement spanning the full mid-IR region from approx. 4000 cm^{-1} to 800 cm^{-1} .⁷¹ Furthermore due to their thin-film properties they are compatible with other thin film preparation techniques and are accessible for optical modeling by means of *e.g.* effective medium theories.⁹⁸

Metal island films for SEIRA applications can be inexpensively fabricated on various substrates in particular IR transparent substrates such as silicon or CaF_2 using various metals like Au^{67, 71, 72, 108-110}, Ag^{66, 111}, Cu¹¹², Pt^{113, 114}, Pd¹¹⁴, Ni¹¹⁵ or Fe.^{116, 117} Various schemes for the fabrication of metal island films have been demonstrated as suspension of colloidal nanoparticles^{118, 119}, wet-chemical deposition¹¹⁰ or by means of physical deposition techniques as sputtering or thermal evaporation^{37, 69, 71, 72, 97, 104}.

The physical origins of the enhancement observed in SEIRA are still a topic under debate. Major contributions to the enhancement, provided by the metal-island film substrates, result from the enhancement of the optical near-fields in the vicinity of or especially in the gaps between the metal islands. The excitation of collective electron oscillations (localized plasmonic resonances) in the sub-wavelength sized islands as well as the interparticle coupling results in this observable enhancement of the near-field.^{69, 86} Further enhancement is obtained in consequence of film effects as the metal island films show a very high refractive index in combination with a vanishing absorption. In addition chemical enhancement mechanisms are also discussed to contribute to the enhancement. In order to gain a detailed understanding of the enhancement mechanisms, especially to obtain access to the contribution of the near-field enhancement rigorous optical simulations of the island films using Maxwell solvers with *e.g.* finite element methods (FEM) are required (see also section 2.4.4).⁹⁸ Such an analysis is outside the scope of this thesis and the obtained enhancement is regarded as a combination of the different contributions.

A broad and detailed overview of the field of SEIRA can be found in several reviews *e.g.* by Osawa *et al.*⁹⁷ and in the book by Aroca *et al.*⁹⁸

Localized plasmonic resonance

The enhancement of the electromagnetic field by plasmonic resonances in metal nanostructures is an integral component of the enhancement mechanism in surface enhanced vibrational spectroscopy. In subwavelength particles localized plasmonic resonances (LSPR) can be excited, depending on size, shape and material of the particles and on their environment.^{120, 121} In the case of a simple sphere Mie theory¹²² can be applied to calculate the extinction coefficients while for more complex particle geometries numerical methods as *e.g.* the discrete dipole approximation¹²³ have to be utilized. The plasmonic resonance is characterized by a strong increase in the extinction coefficient at defined wavelengths. The resulting peak is defined by its spectral width w and its central position λ_{\max} .

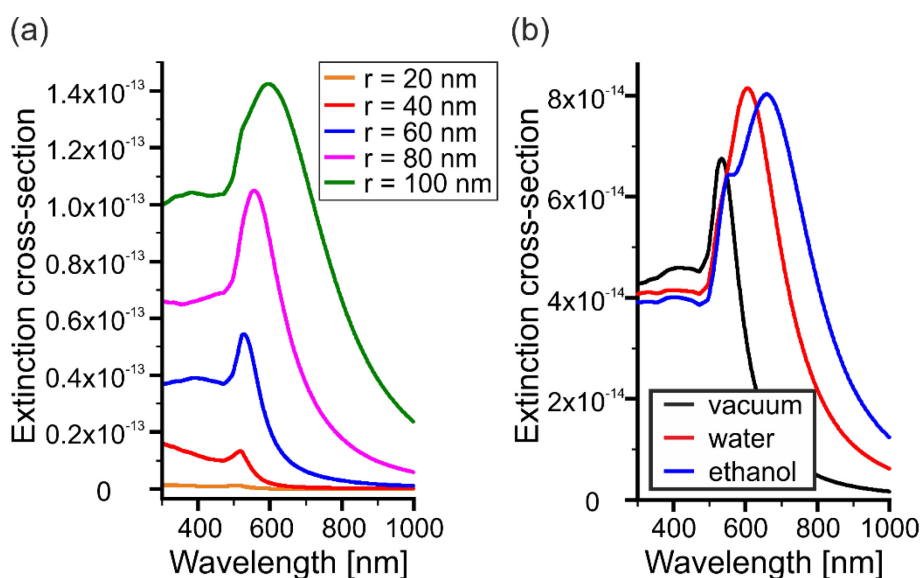


Figure 2-6: Extinction cross-section of Mie scattering for a single spherical gold nano particle. (a) Extinction cross section for different radii of the gold nano particle. (b) Extinction cross section of a 65 nm gold nanoparticle with different surrounding media. (Calculated by MiePlot v4.5 @Philip Laven).

For single gold spheres in vacuum with radii between 10 nm and 90 nm Mie theory predicts a dipolar resonance where the corresponding peak in the spectrum increases in intensity and width. For smaller particles deviations from the result of are observed. In this case Mie theory can no longer provide an appropriate representation of the plasmonic properties as *e.g.* quantum effects in consequence of the

high localization of the electrons have to be taken into account.^{124, 125} With growing sphere radius λ_{\max} is red-shifted (Figure 2-6 (a)). In spheres with a larger radius also higher order resonances as *e.g.* quadrupolar resonances will be excited.

Figure 2-6 (b) displays how the dielectric environment of a single gold sphere with a radius of $r = 65$ nm influences its plasmonic resonance. With increasing refractive index of the surrounding material ($n_{\text{vacuum}} = 1 < n_{\text{water}} \approx 1.33 < n_{\text{ethanol}} \approx 1.5$) the plasmonic resonance is red-shifted. In an ethanol environment ($n_{500 \text{ nm}} \approx 1.5$) contributions of higher order resonances can already be identified for a radius of $r = 65$ nm by the splitting of the resonance peak into two contributions. The effect of the chemical environment on the plasmonic resonance is of high importance for the application of metal island films under *in situ* conditions as the environment of the solvent will directly influence the plasmonic properties of the enhancement substrate and has to be considered.

Since the plasmonic resonance is sensitive to the environment of the nano particle, a homogeneous coating results in a defined shift of the resonance peak depending on the coating thickness (Figure 2-7). This effect forms the basis for LSPR sensing.¹²⁶⁻¹²⁸

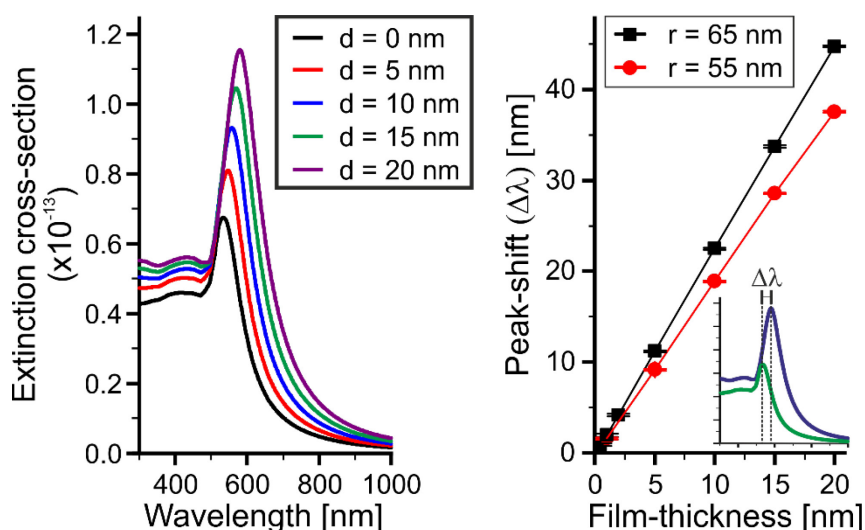


Figure 2-7: Dependence of the extinction cross-section of Mie scattering of a single gold nanoparticle on the thickness of a homogeneous layer with $n_{\text{layer}} = 1.5$ coating the nanoparticle. (a) Extinction coefficient for a single gold sphere ($r=65$ nm) with varying coating thickness d . (b) Shift of maximum position of the plasmonic resonance in dependence on film thickness for gold spheres with $r = 55$ nm and $r = 65$ nm. λ_{\max} was determined by fitting of a Gaussian curve to the spectrum. (Calculated with MiePlot v4.5 @Philip Laven).

The considerations above were made for spherical nano-particles but qualitatively hold true also for metal island films. In the case of metal island films multiple effects which influence the resonance however have to be considered in the analysis. On the one hand deposition of the nanoparticles on a substrate alters their resonance behavior.¹²⁰ On the other hand the resonance is more complex in consequence of the size distribution which follows a log-normal distribution and the variation in the shape of the metal islands.⁹⁸ Furthermore due to the small spatial separation of often less than one nanometer between individual islands interparticle coupling as *e.g.* dipole-dipole or higher order interactions influence the LSPR of the nano-islands forming the metal island film.¹²⁹⁻¹³¹

Island film formation and percolation threshold

The enhancement substrates employed in this thesis rely on a self-assembled formation of metal islands during the deposition before the formation of a thin film of the respective metal is realized. The formation of the metal islands by heterogeneous nucleation depends on the evaporated metal and the substrate chosen for the deposition. The heterogeneous nucleation minimizes the free

interfacial surface energy of the film, minimizing Gibbs energy (ΔG) by the diffusion of the metal atoms on the surface. Three different growth models for the formation of thin films can be derived from Young's equation.^{132, 133}

- Island growth or Volmer-Weber growth
- Layer-plus-island growth or Stranski-Krastanov growth
- Layer-by-layer growth or Frank-van der Merwe growth

The growth of gold on silicon with a native oxide is assumed to follow an island growth according to the Volmer-Weber growth where the atoms of the metal are more strongly bound to each other than to the substrate.¹³⁴

In this growth model separated islands are formed which grow in size and form clusters until a maximum coverage of separated islands is obtained. If more gold is provided for the formation the island film percolates meaning that individual islands coalesce and a conductive layer or network is formed. With a further deposition of gold remaining holes in the film are subsequently filled until a closed thin gold film is obtained. The amount of deposited gold where the film morphology changes from individual islands to a conductive film or network is termed percolation threshold.¹³⁵

2.3.2. Fabrication

The enhancement substrates presented in this thesis are fabricated on silicon and CaF_2 substrates by depositing gold via a thermal evaporation under high vacuum conditions. Before the deposition the silicon substrates were cleaned in the following steps:

- 5 minutes in Ethanol in Ultrasonic bath
- Drying with Air or Nitrogen gas (N_2)
- 10 – 15 min in Piranha solution ($\text{H}_2\text{SO}_4:\text{H}_2\text{O}_2$) (2:1)
- Drying with Air or N_2

After the cleaning the substrates were either directly used or stored in deionized water (Millipore SAS, Direct-Q® 3UV) until usage. CaF_2 substrates were used as received. The deposition setup comprises a small separately pumped loading chamber where the sample can be loaded onto a transfer-arm. Depending on the size of the substrate two different sample handling schemes have been developed. For small samples up to a size of 2 cm x 1 cm the sample can be transferred to a manipulator allowing one to adjust the sample's rotation in the x-z-plane, the tilt relative to and the position in the y-z-plane (Figure 2-8). For larger samples, as employed for the observation window in the optofluidic platform, the sample stays on the transfer arm in a special holder for the whole deposition process. This configuration eliminates the option to rotate the sample in the x-z-plane but allows one for the adjustment of position and tilt to a larger extend than with the manipulator. After evacuation of the loading chamber the sample is transferred to the main chamber where the material is deposited at a pressure of $\approx 10^{-7}$ mBar. Gold is evaporated from a molybdenum-crucible with a boron-nitride (BN) liner using a water-cooled electron-beam evaporator (tectura GmbH). The employed evaporator uses an electron-beam assisted thermal evaporation scheme where the electrons emitted by the filament are heating up the crucible instead of directly interacting with the gold. The BN-liner in this setup is mandatory to avoid alloying of gold and molybdenum. In order to allow for effective evaporation of gold from the BN-liner tungsten-emission tips were inserted into the crucible. This approach is in analogy to the common approach of gold evaporation from a wetted wire, but is termed re-wetting wire technique because of the re-wetting of the wire from the reservoir at the bottom of the crucible. The emission of gold from the crucible can be controlled by adjusting the potential of the crucible, the heating current of the electron emitting filament and the emission current. The emission current

controls the flux of electrons from the filament to the crucible. Typically evaporation rates of 0.4 nm/min to 4.5 nm/min were obtained for gold deposition.

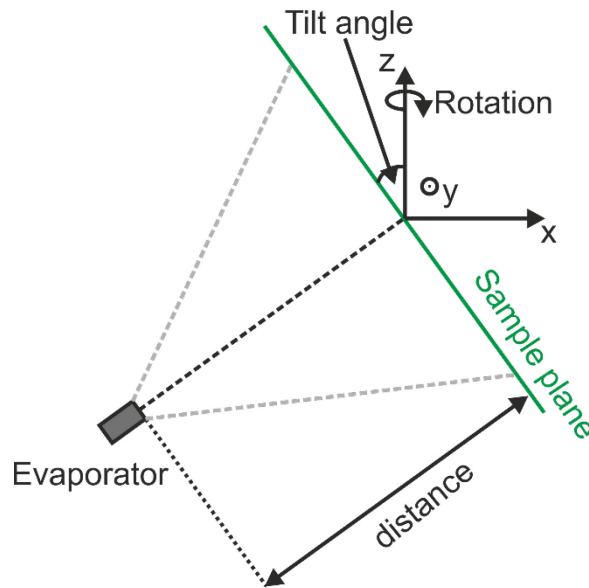


Figure 2-8: Schematics of evaporator setup

Figure 2-8 depicts the general geometry of the evaporation setup. In the given configuration the distance between evaporator and sample plane is fixed. Possibilities to vary the deposition depending on the geometric configuration are given due to the possibility to change the incidence angle of the material flow and by changing the position of the sample in the emission cone.

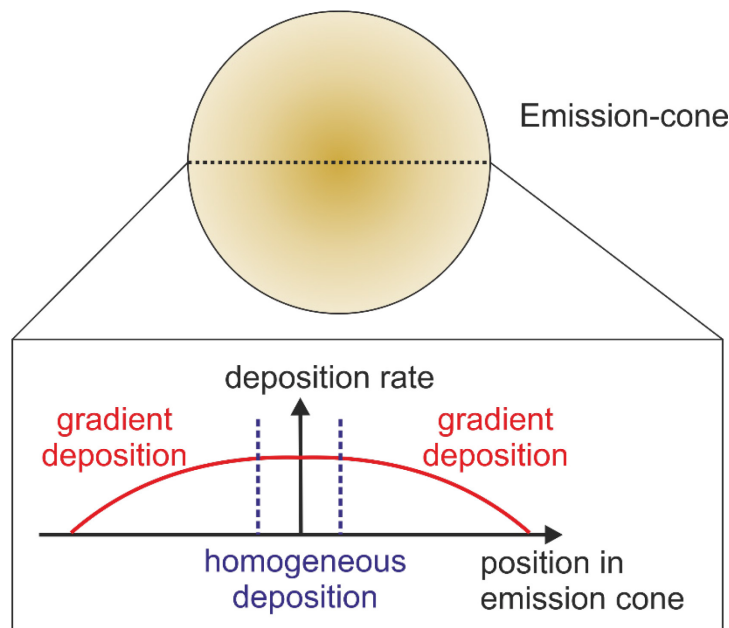


Figure 2-9: Schematic of emission profile of the electron beam evaporator

Figure 2-9 depicts the emission cone and the profile of the deposition rate provided by the evaporator. In the center of the emission cone the deposition rate is constant and a homogeneous coverage with a thickness variation < 0.5 nm can be achieved in this area. For the given setup due to the fixed distance this area is approx. 2 cm x 2 cm. Towards the edges of the emission-cone the deposition rate decreases exponentially. In order to obtain an estimation of the distribution of the deposition rates, the evaporation is calibrated after each maintenance of the evaporator by deposition on a silicon calibration substrates with the same dimensions as the sample holder

(28 mm x 90 mm). The distribution of the effective thickness and correspondingly the deposition rate is determined by a 2D mapping of the calibration sample by UV-Vis ellipsometry and optical modeling in SpectraRay 3 (Sentech Instruments GmbH). The optical model used; was a three-layer model of Si/SiO₂/Au with tabulated values of the bulk materials for the dielectric constants. Figure 2-10 exemplarily shows the effective thickness distribution of a calibration sample.

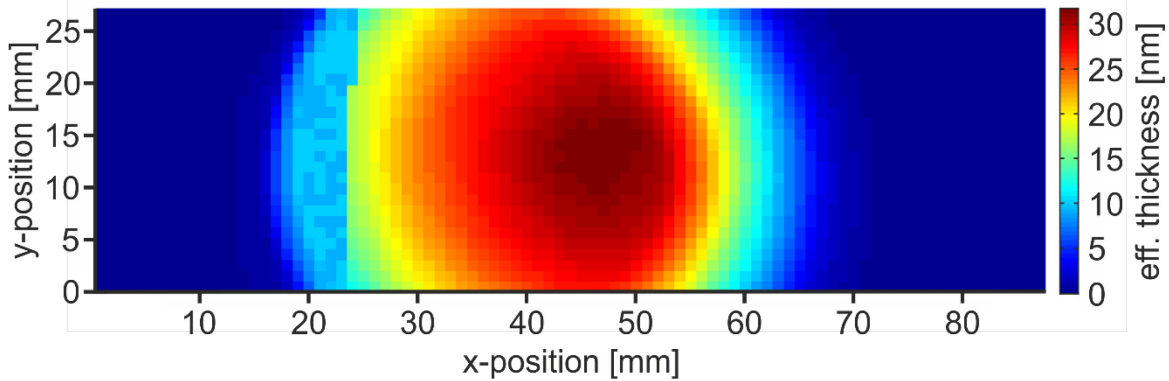


Figure 2-10: Measured distribution of effective film thickness in the area of the substrate holder. The effective film thickness of the gold island film was determined by UV-Vis ellipsometry using bulk optical constants from literature for the materials in a 3-layer model of Si/SiO₂/gold.

The asymmetry of the emission cone visible in Figure 2-10 is most likely due to a misalignment of the crucible in the evaporator which can explain the asymmetry by shadowing effects. The almost straight line on the left side (around x = 24 mm) is an artifact resulting from an inadequacy of the optical model used to determine the effective thickness. In combination with a developed software the data obtained from the calibration sample can be used to determine the optimum positioning of the substrate on the substrate holder.

By proper positioning of the sample the emission profile can be utilized to obtain different types of enhancement substrates as shown in Figure 2-11.

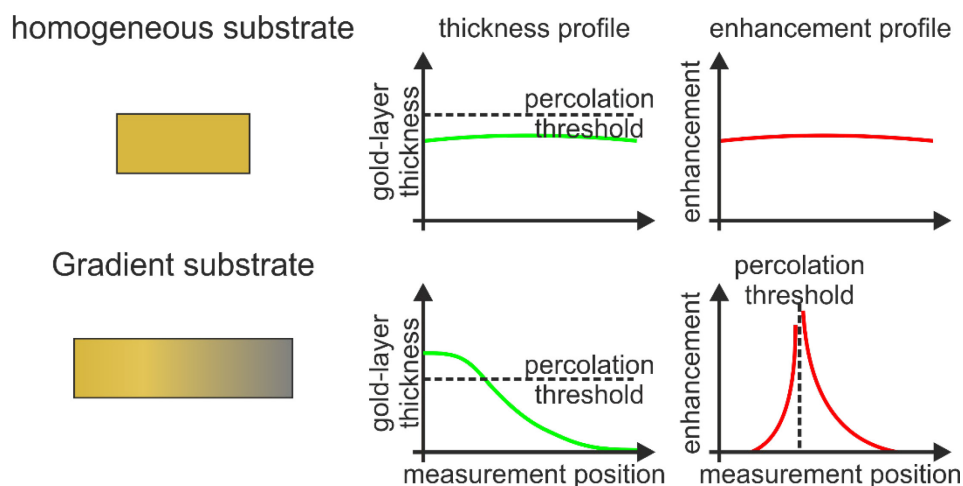


Figure 2-11: Schematic of realizable types of enhancement substrates depending on positioning within the emission cone of the evaporator.

In Figure 2-11 the distribution of the metal is schematically shown in the first column. The second column shows the thickness profile of the metal film in dependence of the position on the sample and the third column shows the obtained enhancement factor in dependence on the position on the sample.

Homogenous substrates can be fabricated by placing the substrate within the area of homogeneous deposition rates and offer a homogenous enhancement over the full area of the substrate (see top-row of Figure 2-11). The gold island film thickness for such substrates is kept below but as close as possible to the percolation threshold to achieve maximum enhancement.

Gradient substrates (lower row of Figure 2-11) are fabricated by using the decreasing deposition rate at the edges of the emission cone. By placing one side of the substrate in the area where homogeneous deposition rates are achieved a variation of the gold-layer thickness from maximum thickness to a blank substrate can be obtained. This type of substrate has tunable enhancement properties on a single substrate and offers a variety of new applications and possibilities for investigations (see section 4.1.1).

The size of the substrates used as observation windows in the optofluidic cell furthermore permits two types of substrates shown in Figure 2-12.

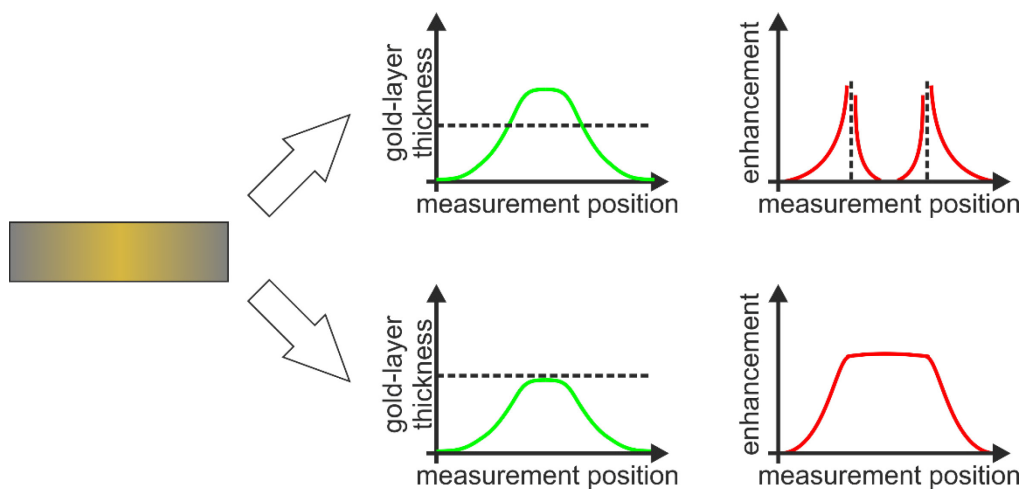


Figure 2-12: Schematic of different types of enhancement substrates realizable on observation windows for the optofluidic platform. Dashed line in the graph of gold-layer thickness indicates percolation threshold.

The substrates can either be realized with two areas providing full tunability of the enhancement separated by an area with a fully percolated gold film (top row of Figure 2-12) or with two areas of partially tunable enhancement and an area of optimized homogeneous enhancement (bottom row of Figure 2-12).

2.3.3. Line shape of vibrational bands in SEIRA spectroscopy

The line shape of vibrational bands in SEIRA spectroscopy may be different to the line shape observed in non-enhanced IR spectroscopy. The most distinct difference between SEIRA and IR spectra is that the line shape of the vibrational peaks in SEIRA shows an asymmetry in dependence on the enhancement and hence the morphology of the gold island film (Figure 2-13). This effect of a “Fano-type” band shape and its origin has been studied by several groups.^{111, 116, 136} The observed band shape can be explained by the coupling between the broad plasmonic resonance and the sharp vibrational band of the adsorbates in analogy to the Fano effect.¹³⁶⁻¹³⁸ Another possible explanation can be found in the dynamic interaction of the vibrational modes of the adsorbate and the excitation of electron-hole pairs. As Priebe *et al.* however pointed out the effect of electron-hole pair excitation should be limited to the first layer of the adsorbate and cannot explain the Fano type band shape observed for multilayer systems. They could also show that the asymmetric line shape can be reproduced by optical modeling using a simplified effective medium theory for the description of the metal island film.

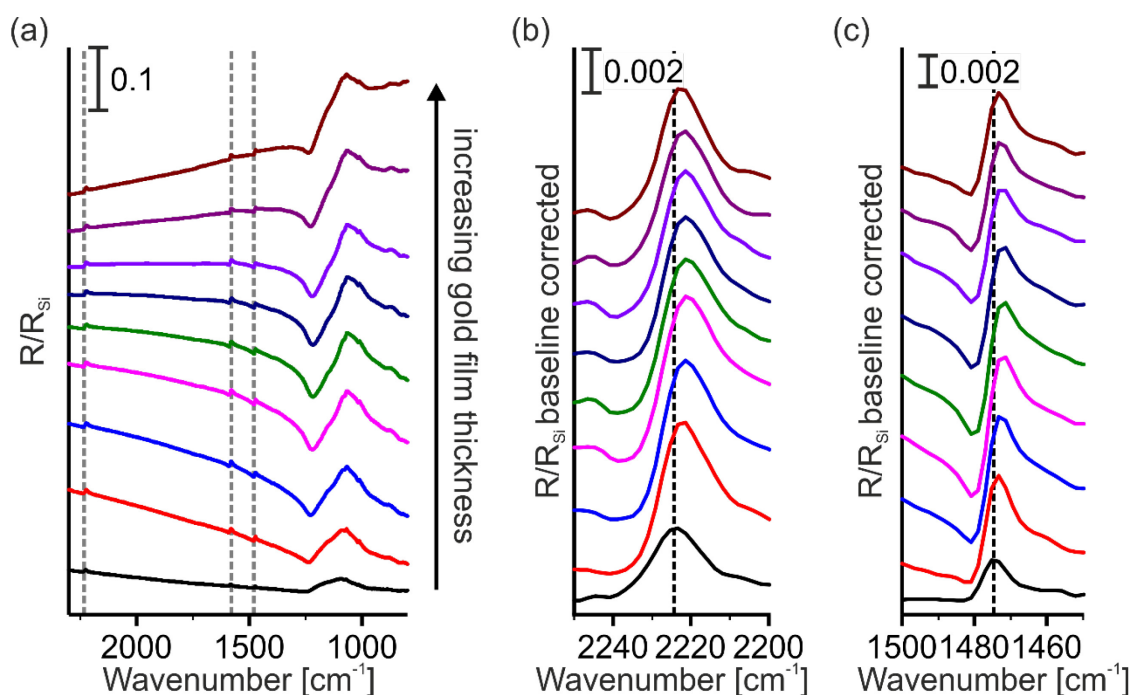


Figure 2-13 Changes in the line shape of vibrational bands in SEIRA spectroscopy in dependence of the morphology of the gold island film on the example of a 4-mercaptobenzonitrile SAM on a gradient gold island film substrate. (a) IR microscopic reflection spectra obtained by a line scan along the gradient substrate. A measurement on a silicon substrate was used as a reference. (b) Baseline corrected zoom into the region of the vibrational band of the stretching vibration of the $C\equiv N$ -group of 4-MBN. The spectra were baseline corrected using a linear baseline and shifted for a better comparison. (c) Baseline corrected zoom into the region of the vibrational band of the combined stretching and deformation vibration of the phenylene ring of 4-MBN. The spectra were baseline corrected using a linear baseline and shifted for a better comparison.

Figure 2-13 exemplarily show the discussed effect on the example of two vibrational modes of the $C\equiv N$ and the phenylene group of 4-MBN obtained from a SAM on a gradient gold island film substrate. With increasing overlap of the plasmonic resonance and a resulting increase in the enhancement the shape of the observed vibrational band becomes asymmetric (Figure 2-13 (b) and (c)). In consequence of the asymmetry the wavenumber of the maximum of the vibrational band is shifted to lower wavenumbers. This may complicate the direct assignment of the vibrational bands and the identification of a molecule and in particular complicate the analysis of the secondary structure of proteins. Also the determination of the amplitude of or the area under vibrational band is complicated by the asymmetry. However for low enhancements no or only a low asymmetry is observed and the spectral position of the vibration can be determined at the cost of the intensity of the signal.

In consequence it has to be noted that a trade-off can be made between asymmetry and enhancement. If the spectral position of the vibrational band is important *e.g.* for comparison with databases, SEIRA analysis should be performed at low enhancement in order to minimize the asymmetry and the spectral shift of the maximum of the vibrational band. In the case where maximum sensitivity is required the asymmetry of the vibrational bands may be less important and higher enhancement factors can be used to increase the sensitivity. It has to be noted that the statements above are made for the *ex situ* application of metal island film, under *in situ* conditions the relations may be different but have not yet been evaluated.

2.3.4. Enhancement factor

The definition of the enhancement factor (EF) for SEIRA is a topic of lively debate. In this thesis the idea of Aroca *et al.*¹³⁹ was used. The idea is the comparison between the spectrum of the organic film

on a flat gold substrate and the spectrum of the same organic film on an enhancement substrate recorded under identical conditions. With the employed IR microscope with a Cassegrain-objective the detection of the IR signal is challenging as the signal is too weak to be distinguished from the noise. Alternative objectives as a grazing incidence (GIR) or ATR objective may be used for the measurement of monolayers but imply other challenges for the evaluation of the obtained spectra and may not easily be compared to the spectra obtained with a Cassegrain-objective. In consequence the spectra for the comparison are obtained by optical simulation. In this work IR ellipsometry has been employed to characterize the optical properties of the organic film on bulk gold samples (SiO_2/Au , $d_{\text{Au}} = 200 \text{ nm}$, S_{sens}) by optical modeling of the obtained $\tan\Psi$ spectra in SpectraRay 3 (Sentech Instruments GmbH).

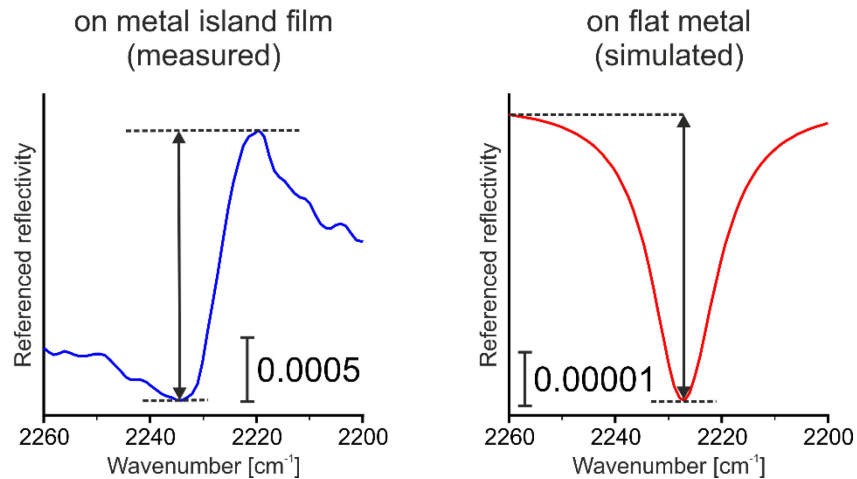


Figure 2-14: Peak-amplitudes of exemplary vibrational band measured in IR microscope (Cassegrain objective, angle of incidence 17.125°) on metal island film (left) and simulated on bulk gold for an angle of incidence of 17.13° for the $\nu(\text{C}\equiv\text{N})$ vibrational mode of 4-Mercaptobenzonitrile.

Figure 2-14 shows exemplarily the vibrational band $\nu(\text{C}\equiv\text{N})$ of 4-MBN measured on a gold island film and simulated on a flat gold substrate. Due to the Fano-type shape¹³⁶ of the vibrational band on the enhancement substrate a comparison of the area under the curve would be strongly biased by the choice of the base line and the definition of the width of the vibrational band. In consequence the EF is here defined as the ratio of the amplitudes A_{enhanced} and A_{normal} of the vibrational bands (indicated by the arrows in Figure 2-14) obtained from the measurement on an enhancement substrate and simulated or measured on a thick gold film respectively.

$$\text{EF} = \frac{A_{\text{enhanced}}}{A_{\text{normal}}} \quad (2-4)$$

Typical enhancement factors obtained for the presented gold island films substrates with this calculation method lie in the range of 20 - 60.

In comparison to a flat gold surface the structure of the island film leads to an enlargement of the surface area which also has to be considered in the calculation of the enhancement factor.

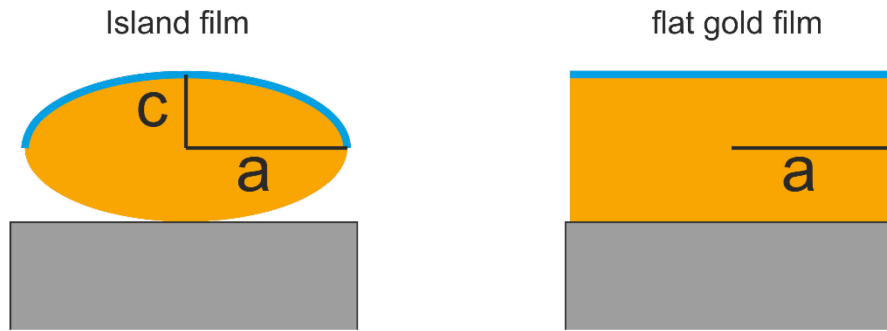


Figure 2-15: Schematic drawing of enlarged surface area of a metal island in comparison to flat gold surface.

The surface area of an individual gold island can be approximated by describing the island as an oblate spheroid with semi-half axis a and c (Figure 2-15).^{37, 140, 141} An approximation of the increase in surface area can then be made by comparing the surface area of the spheroid with the surface area of a cylinder with the same radius. In consequence of the small separation $< 1\text{nm}$ between the islands only the top half of the ellipsoid and the top surface of the cylinder are considered as effective area where the molecule can bind to the surface. The surface area of an oblate spheroid is given by:

$$S_{oblate} = 2\pi a^2 + \pi \frac{c^2}{e} \ln\left(\frac{1+e}{1-e}\right) \quad (2-5)$$

With $e^2 = 1 - c^2/a^2$ and the surface area of the cylinder is a circle whose area is given by:

$$S_{circle} = \pi a^2 \quad (2-6)$$

For typical island dimensions of $a = 10\text{ nm} - 20\text{ nm}$ and $a = 2\text{ nm} - 5\text{ nm}$ determined by AFM measurement the increase in surface area lies between 3 and 14 % and may be considered for the calculation of the enhancement factor. In principle the shown approach is still a highly simplified approximation as the island dimensions in a real island film follow a log-normal distribution and different island shapes would have to be considered.^{140, 142} In practice the consideration of the increased surface area requires the knowledge of the discreet island geometry and the distribution of these geometries over the area in each measurement. As the island geometry may vary on each sample and might be unknown for the sample or the particular area of the sample under investigation an average increase in surface area of 8% has been assumed for the experiments performed in this thesis.

2.4. Data analysis & Optical modeling

In the interpretation of measurement data from IR ellipsometry and spectroscopy experiments valuable information can be obtained by direct analysis of the vibrational bands in the obtained spectra. The use of optical modeling however allows one to perform detailed analysis giving access to physical properties of the sample as *e.g.* film thickness and allows one to perform a quantitative analysis. Optical models are also required to perform a detailed analysis of molecular interactions and other processes as this information can only in very few cases be directly obtained from examining the vibrational fingerprint. In the following the employed method for the analysis of the obtained data will be introduced and a description of the optical models used in this thesis will be given.

2.4.1. General considerations

The complex dielectric function $\varepsilon(\nu)$ of a material is used to describe the interactions of a material with electromagnetic radiation. In a homogeneous material the material equations of Maxwell's equation relate the dielectric displacement current $\vec{D}(\nu)$ to the electric field $\vec{E}(\nu)$ by¹⁴³:

$$\begin{aligned}\vec{D}(\nu) &= \varepsilon_0 \vec{E}(\nu) + \vec{P}(\nu) \\ &= \varepsilon_0 (1 + \chi_e(\nu)) \vec{E} \\ &= \varepsilon_0 \varepsilon(\nu) \vec{E}\end{aligned}\tag{2-7}$$

where ε_0 denotes the vacuum permittivity and $\chi_e(\nu)$ the susceptibility of the material. The complex dielectric function relates as an answer function of the material the dielectric polarization density \vec{P} to an electric field \vec{E} . In general $\varepsilon(\nu)$ is a tensor which for homogeneous materials with appropriate symmetries may reduce to a vector (uniaxial or biaxial materials) or a scalar constant in the case of homogeneous isotropic materials.

The complex dielectric function is related to the complex refractive index $N = n + ik$ comprising the refractive index n and the absorption coefficient k of the material:

$$\varepsilon = N^2 = (n + ik)^2\tag{2-8}$$

2.4.2. Direct inversion of ellipsometric measurements

In the case where the optical activity of the sample as a whole is of importance or under the assumption that the sample consists of a single layer with no surface roughness a pseudo-dielectric function $\langle \varepsilon \rangle$ can be directly calculated from the ellipsometric measurement parameters $\tan \Psi$ and Δ with the help of the Fresnel equations (Eq. (2-10)).⁹²

$$\begin{aligned}\langle \varepsilon \rangle &= \langle \varepsilon_1 \rangle - i \langle \varepsilon_2 \rangle \\ &= \sin(\varphi)^2 \cdot \left[1 + \tan(\varphi)^2 \left(\frac{1 - \tan \Psi \exp(i\Delta)}{1 + \tan \Psi \exp(i\Delta)} \right)^2 \right]\end{aligned}\tag{2-9}$$

Where φ denotes the angle of incidence.

This direct calculation has been employed in the characterization of the enhancement substrates where the optical activity of the substrate as a whole gives sufficient information for analysis.

2.4.3. Optical simulation

In general, a real sample will not consist of a single layer and will in almost all cases exhibit a certain surface roughness. In this case an optical model is required in order to correctly simulate the measured

spectra and extract information about individual layers of the sample. The optical model is commonly represented by a layer-model as shown for the example of a reflection measurement in Figure 2-16.

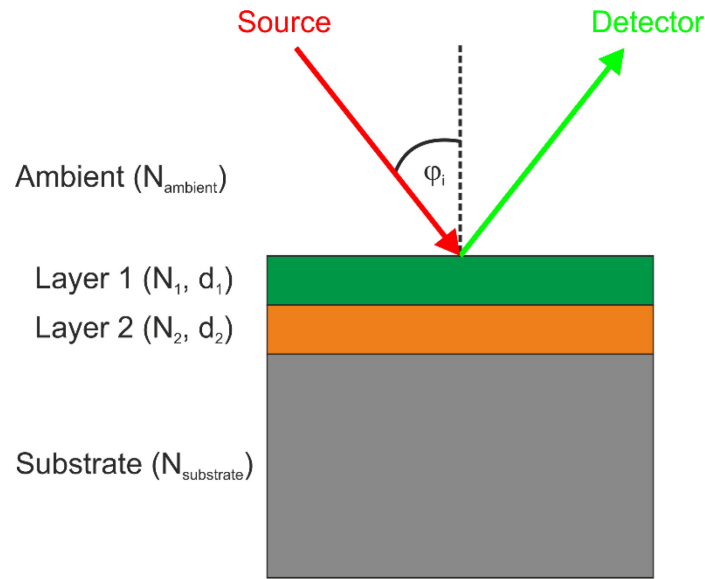


Figure 2-16: Schematic layer-model representation of a sample with two layers on a substrate for the optical modeling of measurements in reflection geometry.

The layer-model schematically depicts the physical conditions of the measurement. An EM wave from a source impinges on the sample under an incidence angle φ_i and the reflected part of the wave is measured by a detector. The sample is represented by a stack of different layers characterized by their complex reflection indices N_j and thicknesses d_i on top of a substrate with a thickness much larger than the thickness of the layers ($d_{\text{substrate}} \gg d_i$) that is therefore assumed to be semi-infinite. By simulating the propagation of the incident radiation through the stack of layers the signal at the detector can be modeled. The chosen modelling approach depends on the complexity of the sample.

In the simplest case of an interface between isotropic and homogeneous layers the wave will be partly reflected and transmitted according to the Fresnel equations (Eq.: 2-10). At the interface between the j -th and $(j+1)$ -th layer with complex reflection indices N_j and N_{j+1} and the wave propagating under the angle φ_j in layer j they are given by:

$$r_{s,j,j+1} = \frac{N_j \cos \varphi_j - N_{j+1} \cos \varphi_{j+1}}{N_j \cos \varphi_j + N_{j+1} \cos \varphi_{j+1}} \quad (2-10)$$

$$r_{p,j,j+1} = \frac{N_{j+1} \cos \varphi_j - N_j \cos \varphi_{j+1}}{N_{j+1} \cos \varphi_j + N_j \cos \varphi_{j+1}}$$

$$t_{s,j,j+1} = \frac{2N_j \cos \varphi_j}{N_j \cos \varphi_j + N_{j+1} \cos \varphi_{j+1}}$$

$$t_{p,j,j+1} = \frac{2N_j \cos \varphi_j}{N_{j+1} \cos \varphi_j + N_j \cos \varphi_{j+1}}$$

where the propagation angle of the transmitted part of the wave in layer $j+1$ φ_{j+1} is given by Snell's law.

$$N_j \sin \varphi_j = N_{j+1} \sin \varphi_{j+1} \quad (2-11)$$

The analysis of multilayer structures also requires the consideration of multi-beam interferences, as schematically shown in Figure 2-17.

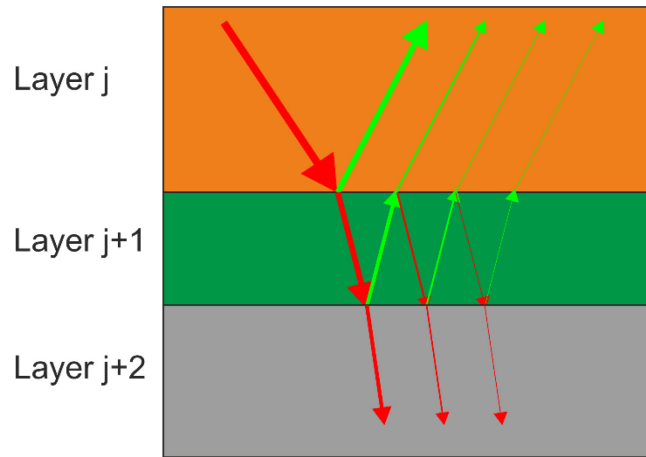


Figure 2-17: Schematic of multi-beam interference in layered structure.

The interference condition is dictated by the path length difference between the interfering waves given by:

$$\delta = 4\pi N_{j+1} d_{j+1} \nu \cos \varphi_{j+1} \quad (2-12)$$

The Airy formula can be used to calculate the reflection coefficient taking into account the multi-beam interference.⁹²

$$r_{q,j} = \frac{r_{q,j,j+1} + r_{q,j+1,j+2} \exp(i\delta)}{1 + r_{q,j,j+1} r_{q,j+1,j+2} \exp(i\delta)} \quad (2-13)$$

The subscript q here denotes the p- and s- components of the electric field respectively and the subscripted numbers indicate at which interface the reflection coefficient is calculated. In the form of iterative algorithms as *e.g.* Wolters algorithm, the Airy formula can be applied for systems with multiple layers.³⁵

In order to perform optical simulation of reflectance spectra of metal island film substrates a suitable optical model, enabling one to account for the uniaxial properties of the island film was used in this thesis. The optical model follows the works of Röseler *et al.*⁷² employing Airy's equation and using the model proposed by Azzam and Bashara⁹³ to determine the reflection coefficients for the uniaxial material.

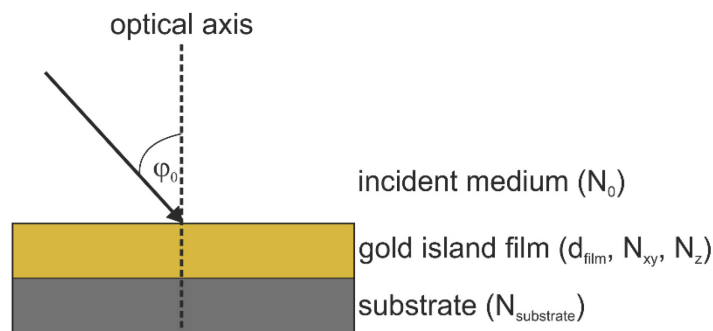


Figure 2-18: Schematic of the optical model employed in the calculation of reflectance spectra. The gold island film is therein described by a uniaxial film.

A schematic view of the employed optical model in a layer representation and the used physical parameters of the optical model are shown in Figure 2-18. The angle φ_0 denotes the angle of incidence, the incident medium and the substrate are assumed as semi-infinite layers and the gold island film is assumed to have a thickness of d_{film} .

The dielectric functions of the incident medium and the substrate are taken from literature. For CaF₂ the data from Li¹⁴⁴ and for silicon the data from Chandler-Horowitz *et al.*¹⁴⁵ were used. The incident medium was air with a constant refractive index of N=1. In order to provide the dielectric functions with the spectral resolution necessary for the simulation the literature data has been fitted and evaluated using spline interpolation.

The reflectance of a uniaxial layer with the optical axis perpendicular to the plane of the layer is defined as⁷²:

$$R_t = r_t r_t^* \quad (2-14)$$

Where the superscript * denotes the complex conjugate of the complex quantity and the subscript $t=s, p$ indicates the polarization direction with respect to the plane of incidence. The reflection coefficients are determined using the Airy-formula (equation (2-13)). The reflection coefficients at the individual interfaces are determined following Azzam and Bashara⁹³ and are given by:

$$\begin{aligned} r_{01p} &= \frac{N_{1xy}N_{1z} \cos \varphi_0 - N_0(N_{1z}^2 - N_0^2 \sin^2 \varphi_0)^{1/2}}{N_{1xy}N_{1z} \cos \varphi_0 + N_0(N_{1z}^2 - N_0^2 \sin^2 \varphi_0)^{1/2}} \quad (2-15) \\ r_{01s} &= \frac{N_0 \cos \varphi_0 - (N_{1xy}^2 - N_0^2 \sin^2 \varphi_0)^{1/2}}{N_0 \cos \varphi_0 + (N_{1xy}^2 - N_0^2 \sin^2 \varphi_0)^{1/2}} \\ r_{12p} &= \frac{-N_{1xy}N_{1z} \cos \varphi_2 + N_2(N_{1z}^2 - N_2^2 \sin^2 \varphi_2)^{1/2}}{N_{1xy}N_{1z} \cos \varphi_2 + N_2(N_{1z}^2 - N_2^2 \sin^2 \varphi_2)^{1/2}} \\ r_{12s} &= \frac{-N_2 \cos \varphi_2 + (N_{1xy}^2 - N_2^2 \sin^2 \varphi_2)^{1/2}}{N_2 \cos \varphi_2 + (N_{1xy}^2 - N_2^2 \sin^2 \varphi_2)^{1/2}} \end{aligned}$$

The phase thickness δ_p and δ_s are given by⁷²:

$$\begin{aligned} \delta_p &= 4\pi\tilde{\nu}d_{film} \left(\frac{N_{1xy}}{N_{1z}} \right) (N_{1z}^2 - (N_0 \sin \varphi_0)^2)^{1/2} \quad (2-16) \\ \delta_s &= 4\pi\tilde{\nu}d_{film} (N_{1xy}^2 - (N_0 \sin \varphi_0)^2)^{1/2} \end{aligned}$$

The angle φ_2 is calculated using Snell's law (Eq. (2-11)).

The optical models presented here have only a limited applicability for more complex media and samples containing a multitude of different layers. In order to correctly describe such samples 4x4 matrix formalisms have been developed to determine the reflection and transmission coefficients.^{92, 146}

2.4.4. Theoretical optical model for metal-island films

In order to perform optical modeling of the employed enhancement substrates a computationally accessible description of the metal island films in terms of their optical and electronic properties is required. In this context many different models have been developed and proposed. In their reviews Aroca *et al.*⁹⁸ and Oates *et al.*¹⁴⁷ give an overview over the different models, Pucci *et al.*^{86, 116, 117, 136} have discussed the application and limitations of different models for the simulation of SEIRA substrates and the interested reader is referred to these publications for more details.

In principal a detailed analysis of the optical properties of the morphology of the metal island films can be obtained using high resolution SEM images and AFM measurements as structural input for Maxwell-solver based calculations, determining the optical nearfields *e.g.* with finite element (FEM)

calculations. This method is most suitable for regular structures as arrays of plasmonic nano-antennas. Calculations of the optical nearfield of metal-island films can however be performed as shown in Figure 2-19 (a) and (b). From nearfield data far-field spectra can be calculated (Figure 2-19 (c)). The calculations of the near field data and far field spectra shown in Figure 2-19 have been performed by Timur Shaykhutdinov.

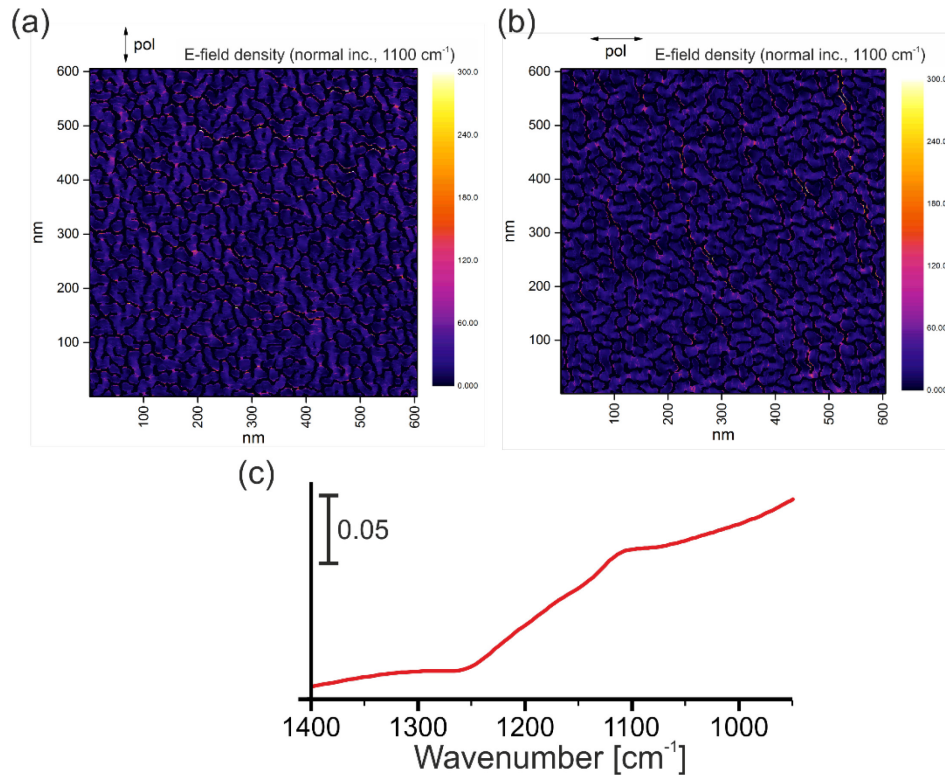


Figure 2-19: Optical properties of metal-island film determined by FEM calculation from SEM image converted with a spatial resolution of 1 nm. (a) Near-field E-field density map for s-polarized light. (b) Nearfield E-field density map for p-polarized light. (c) Far-field spectrum calculated for simplified structures in the region of the SiO₂-vibrational band. FEM simulations were performed by Timur Shaykhutdinov.

Even though the information content of this method is most precise, calculations are highly time consuming for sufficiently discretized calculations required to describe the highly non-periodic structure of the metal-island film substrates. In consequence this method is only of limited use for the analysis of metal-island films and is not yet compatible with fitting algorithms.

Effective medium theories or approximations (EMA) form an alternative approach which requires less computational power for the description of the optical properties of metal island films. EMAs are commonly applied to qualitatively and quantitatively access the enhancement properties of metal-island films and are compatible with fitting algorithms.^{37, 139} However, these type of approximations cannot take into account local field resonances which may play an important role in the understanding of the enhancement.

In general EMAs describe the macroscopic properties of a composite material in terms of effective properties where the individual constituent of the mixture may be of arbitrary shape but are so small in size that the medium can be homogenized for the probing wavelength. Because of the small size of the inclusions the composite film is assumed to be a continuous, parallel-sided layer. In this way Fresnel's equations can be applied in the calculation of transmittance and reflectance of the layer.¹⁴⁸ Most commonly applied are the models developed by Maxwell-Garnett¹⁴⁹ and Bruggeman¹⁵⁰. These models have been initially developed for spherical inclusions but have been extended to various

inclusion shapes. For a broad overview and comparison of different EMA models and their applications the interested reader is referred *e.g.* to the review by Bergman and Stroud.¹³⁵

In this thesis a Bruggeman EMA has been used to determine the effective dielectric function of the metal island films. In comparison to the Maxwell-Garnett EMA, the Bruggeman EMA provides a better approximation for the case of densely packed island films where dipole interactions cannot be neglected.⁹⁷ The employed model is based on the works of Andersson *et al.*^{140, 142, 151} and Eagen¹⁵² extending the Bruggeman EMA¹⁵⁰ to spheroidal inclusions coated with an adsorbate layer. Osawa *et al.*⁶⁷ proposed and demonstrated its applicability for the simulation of SEIRA spectra.

In this model the effective dielectric function $\bar{\epsilon}$ of the metal island film is represented as¹⁵¹:

$$\bar{\epsilon} = \epsilon_h \frac{3(1-f) + f\alpha'}{3(1-f) - 2f\alpha'} \quad (2-17)$$

where ϵ_h is the dielectric function of the host medium surrounding the metal islands, f is the fill-factor and α' is the electrical polarizability of the individual metal islands.

The electrical polarizability depends on the dielectric function of the metal (ϵ_m) the size and shape of the metal islands via the depolarization factors L , the properties of the adsorbate layer (thickness and dielectric function ϵ_d) as well as the dielectric function of the host medium (ϵ_h). The value of the electrical polarizability α' for the coated spheroid can be expressed by^{69, 152}

$$\alpha'_{\perp, \parallel} = \left[\frac{x}{y} \right]_{\perp, \parallel} \quad (2-18)$$

$$x = (\epsilon_d - \epsilon_h)[\epsilon_m L_1 + \epsilon_d(1 - L_1)] + Q(\epsilon_m - \epsilon_d)[\epsilon_d(1 - L_2) + \epsilon_h L_2]$$

$$y = [\epsilon_d L_2 + \epsilon_h(1 - L_2)][\epsilon_m L_1 + \epsilon_d(1 - L_1)] + Q(\epsilon_m - \epsilon_d)(\epsilon_d - \epsilon_h)L_2(1 - L_2)$$

The subscripts \perp and \parallel of α' refer to the polarization direction of the electric field of the applied radiation field relative to the plane of incidence. The individual treatment of the different polarizations allows for the treatment of non-normal incidence of the radiation on the surface and interpretation of ellipsometric data. The subscripts 1 and 2 in x and y indicate the depolarization factors of the uncoated and coated ellipsoid respectively and Q denotes the volume ratio of the uncoated to the coated spheroids.

In order to incorporate the size and shape of the metal islands the depolarization factors L_j ($j = 1, 2$) have to be determined. The individual islands forming the metal island film can be described as oblate spheroids with the axis of rotation perpendicular to the substrate (Figure 2-20).^{10, 97} The oblate spheroids are characterized by the length of their major axis a and minor axis b . The spheroids are assumed to be coated by a homogeneous adsorbate layer of thickness $d_{\text{Adsorbate}}$.

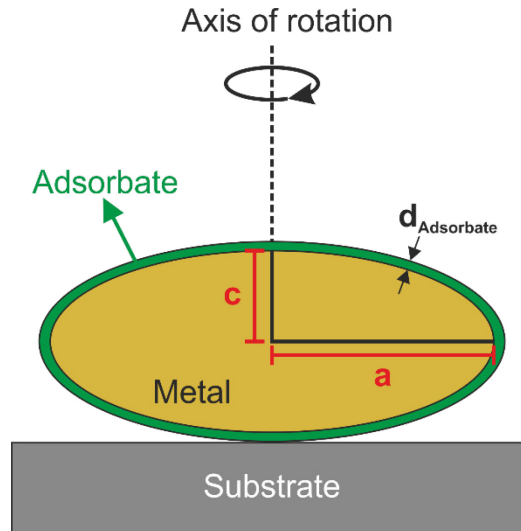


Figure 2-20: Schematic representation of an oblate spheroid used in the model to describe the individual adsorbate coated metal island.

Following the works of Röseler *et al.*⁷² and Hinrichs *et al.*³⁷ the adsorbate layer is considered as an effective medium using a Bruggeman EMA for spheroids of a mixture of the adsorbate and the metal. With this procedure the insulator-semiconductor-metal transition which occurs when the metal islands are more closely packed on the surface with increasing fill-factor can be accounted for.

With the description of the metal islands as oblate spheroids the depolarization factors L_j can be determined following the fundamentals relations derived by Stoner.¹⁵³ The depolarization factors are geometrical factors which give a measure of the curvature perpendicular to a specific axis of the spheroid and have a value $0 < L_j < 1$ where $\sum_j L_j = 1$. Due to the symmetry of oblate spheroids only two depolarization factors have to be determined as $L_x = L_y \neq L_z$. The depolarization factors for an oblate spheroid in terms of its eccentricity $e = \sqrt{1 - c^2/a^2}$ are given by⁹⁸:

$$L_1 = \frac{g(e)}{2e^2} \left[\frac{\pi}{2} - \tan^{-1}(g(e)) \right] - \frac{g^2(e)}{2} \quad (2-19)$$

$$\text{with } g(e) = \sqrt{\frac{1 - e^2}{e^2}}$$

$$L_2 = \frac{1}{2}(1 - L_1)$$

Another parameter in the calculation of α' is the volume ratio Q of the uncoated to the coated particle given by:

$$Q = \frac{V_1}{V_2} = \frac{a_1^2 c_1}{a_2^2 c_2} \quad (2-20)$$

Where a_1 is the length of the major and c_1 the length of the minor axis of the uncoated spheroid and $a_2 = a_1 + d_{abs}$ and $c_2 = c_1 + d_{abs}$ are the respective diameters of the coated particle.

The dielectric function required for the calculation of α' of the metal are taken from literature. For gold the dielectric function determined by Rakic *et al.*¹⁵⁴ have been used. The host is set to be air with $n = const. = 1$ and $k = const. = 0$. The dielectric function of the adsorbate layer can be described by an

oscillator model which represents the molecular oscillations as averaged properties by a Lorentzian oscillator^{11, 155}:

$$\varepsilon(\tilde{\nu}) = \varepsilon_{\infty} + \sum_{k=1}^m \frac{F_k}{\tilde{\nu}_{0,k}^2 + \tilde{\nu}^2 + i\Gamma_k \tilde{\nu}} \quad (2-21)$$

Where the index k indicates the k -th oscillator in the model; $\nu_{0,k}$ is the center frequency of the oscillator; F_k is the parameter of the oscillator strength and is proportional to the dimensionless oscillator strength S_k ($F_k = S_k \cdot \nu_{0,k}^2$) and Γ_k is related to the damping constant γ of the averaged properties of the molecular vibration. F_k and Γ_k are adapted values to directly use wavenumbers rather than frequencies in the calculation. The dimensionless oscillator strength is defined by¹⁵⁵:

$$S_k = \frac{N e^{*2}}{\varepsilon_0 \nu_{0,k}^2 m^*} \quad (2-22)$$

With phenomenological effective ionic charge e^* , reduced mass m^* , and number density N of the oscillators.

The individual parameters of the oscillators can either be taken from literature or have to be determined in additional measurements, which give access to the dielectric function of the adsorbate as *e.g.* IR ellipsometry in conjunction with optical modeling.

With the use of the optical layer model introduced in section 2.4.3 one can use the determined dielectric function to calculate the *ex situ* reflectivity measurements obtained with the IR microscope.

The described optical model can also be used to calculate a pseudo-dielectric function of the metal island film in the UV-Vis region of the spectrum. This allows one to qualitatively reproduce the measurements of the pseudo-dielectric function with UV-Vis ellipsometry and enables to estimate the shift in the plasmonic resonance in correspondence to coating-thickness on the metal-island film as shown in Figure 2-21.

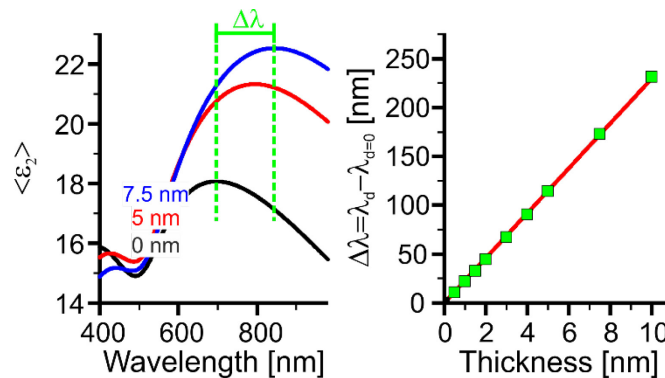


Figure 2-21: Imaginary part of the pseudo-dielectric function of exemplary gold island film on silicon substrate with fixed fill-factor f , length of major and minor axis of gold islands and variation of the adsorbate layer thickness.

For a fixed fill-factor f and length of major and minor axis of the gold islands a linear trend in the shift $\Delta\lambda$ of the plasmonic resonance can be observed in dependence of the adsorbate layer thickness. This information can be used as a measure for the thickness of thin films deposited on the metal-island films. Initial parameters of the metal island film for the simulation can be obtained by fitting of the model parameters f , a and c to a corresponding IR-reflectivity spectrum of the metal-island film.

2.5. Surface preparation & modification

In the following the procedures used for the preparation of model organic layers on the enhancement substrates are presented. Ultra-thin model organic layers are obtained by means of the formation of SAMs on the surface of the enhancement substrates. As an alternative functionalization route the method for the transfer of pre-functionalized graphene to an enhancement substrate is described.

2.5.1. Self-assembled monolayers (SAM)

Self-assembled monolayers (SAM) are ultra-thin molecular layers which only contain one layer of an organic molecule. The formation of such layers is a self-organized process where the molecules of the SAM are adsorbed on the surface of a substrate from a liquid phase or gas phase and form a crystalline (or semi-crystalline) structure on the surface.^{156, 157} SAMs have been widely used to modify the surface properties of various substrates as they present a convenient and flexible way to alter the interfacial properties of the substrate.¹⁵⁷⁻¹⁵⁹ They are also frequently used as a initial building block in biosensing applications providing specific binding sites for the surface immobilization of molecules as *e.g.* proteins or antibodies.¹⁶⁰⁻¹⁶²

In consequence of the ordered adsorption process with almost no desorption, SAM formation from thiolate molecules forms an ideal model systems for investigations with the optofluidic platform to demonstrate its ability to study processes at the solid-liquid interface. They can also be used to demonstrate the high sensitivity obtained by enhancement substrates because they provide small amounts of organic material on the surface. For example the theoretically calculated maximum coverage of a gold surface with a SAM of alkane thiols corresponds to a surface density of 4.5×10^{14} molecules/cm² or 0.74 nmol/cm².¹⁶³ The actual surface density strongly depends on the type of the organic molecule which forms the SAM and the surface on which the SAM is formed.

General considerations

Molecules which are used to form a SAM on a substrate generally comprise two specific functional groups. A head-group with a high affinity to bind to the surface of the substrate and a tail-group which determines the properties of the SAM surface *e.g.* providing a binding side for a protein or antibody or presenting a desired functional group for the further modification of the surface. The two groups are connected by a linker which is of high importance for the organization and alignment of the molecules in the SAM.

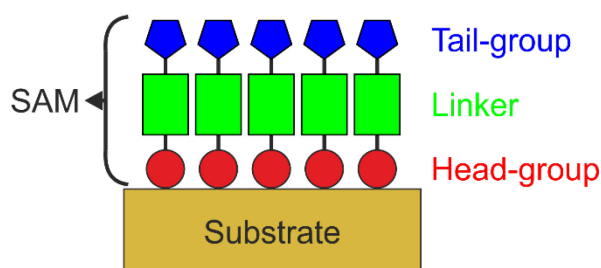


Figure 2-22: Schematic drawing of a substrate surface functionalized with a SAM

SAMs formed from molecules with a thiol functional head groups show a high affinity for binding to the surface of noble and coinage metals and have been extensively studied.^{38, 39, 158, 164}

The kinetics of the formation process of a SAM from a solution of molecules can qualitatively be described by Langmuir-type adsorption models.¹⁵⁷ Even though originally derived to describe the adsorption kinetics from a gaseous phase on a solid, most of the assumption of the Langmuir-model may to a certain extend be assumed for the formation of SAMs. The model assumes that¹⁶⁵:

- The surface has a defined number of specific binding sites and all binding sites have equal properties.
- Molecules can only bind to the specific binding sites on the surface.
- Each binding site absorbs only one molecule and the final state is a monolayer on the solid surface.
- No interaction between the adsorbed molecules occurs.

Following this definition the surface of the sample can adsorb a maximum number of molecules N_{max} equal to the number of binding sites available on the surface

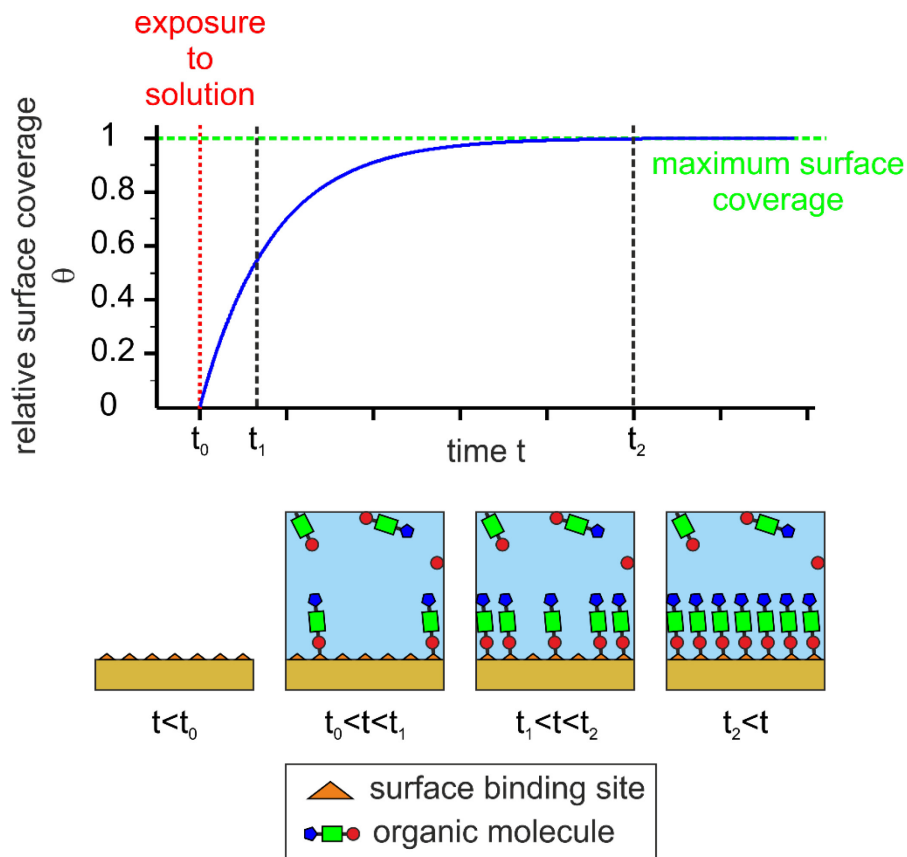


Figure 2-23: SAM formation following a first order Langmuir adsorption model.

As illustrated in Figure 2-23, the change in the surface coverage relative to N_{max} ($\theta = N/N_{max}$) with time is proportional to the number of free binding sites available on the surface ($1-\theta$) and the adsorption/desorption rates. With the affinity of the organic molecule to bind to the surface expressed by the adsorption constant k_{ads} , the desorption rate k_{des} and the concentration c of the bulk solution the time dependent change in surface coverage ($d\theta/dt$) can be described by an inhomogeneous first order differential equation.¹⁶⁶

$$\frac{d\theta}{dt} = k_{ads} \cdot c(1 - \theta) - k_{des}\theta \quad (2-23)$$

The solution to the inhomogeneous first order differential equation (2-23) yields the formula for the time-dependent fractional surface coverage $\theta(t)$:

$$\theta(t) = \left(\frac{1}{1 + \frac{k_{des}}{k_{ads}c}} \right) [1 - \exp(-(k_{ads}c + k_{des})t)] \quad (2-24)$$

It has to be noted that for the formation of a SAM the number of available binding sites on the surface depends on the surface properties. The number of molecules which adsorb on the surface depends strongly on the type and size of the molecule which is used to form the SAM.

In the case where the desorption is negligible as *e.g.* assumed here for the formation of a SAM by binding of a thiol-group to a noble metal surface¹⁶⁶ formula (2-24) further simplifies to:

$$\theta(t) = [1 - \exp(-k_{ads}ct)] \quad (2-25)$$

It has however to be noted that in principle the assumption of the Langmuir model may be violated in the process of SAM formation. Binding sites may be blocked by steric hindrance by previously bound molecules which results in the effect that not all binding sites are equal. If the molecules forming the SAM possess suitable binding sites molecules may also adsorb onto each other and may form multilayers. Furthermore in a SAM the interactions between the molecules may play an important role for the arrangement of the molecules within the SAM *e.g.* π - π interactions between phenylene groups of aromatic compounds which further influence the obtainable packing density on the surface. Numerous models exist which allow to account for different effects occurring during the formation of the SAM and in general for the adsorption/desorption of molecules on a surface which may be used for a more detailed and in depth analysis of the adsorption/desorption processes.^{156, 167-171}

SAM preparation

All SAMs in this thesis were prepared by adsorption of molecules from the liquid phase. A solution of the molecules with the desired concentration (usually in the range of 1-10 mM) was prepared by dissolving the molecules in an appropriate solvent. As solvents ethanol, Dimethyl sulfoxide (DMSO) and deionized water (Millipore SAS, Direct-Q® 3UV) have been used.

For the *ex situ* characterization experiments the prepared enhancement substrates were immersed in the solution at room-temperature for a minimum of 10 h to allow for SAM formation. Subsequently, the substrates were rinsed with the pure solvent to remove excess material and dried using air or nitrogen.

For the *in situ* experiments with the optofluidic platform the experimental procedures are described in the respective sections in the results part of the thesis.

2.5.2. Transfer of pre-functionalized graphene

As an alternative surface modification strategy the transfer of functionalized graphene has been investigated.

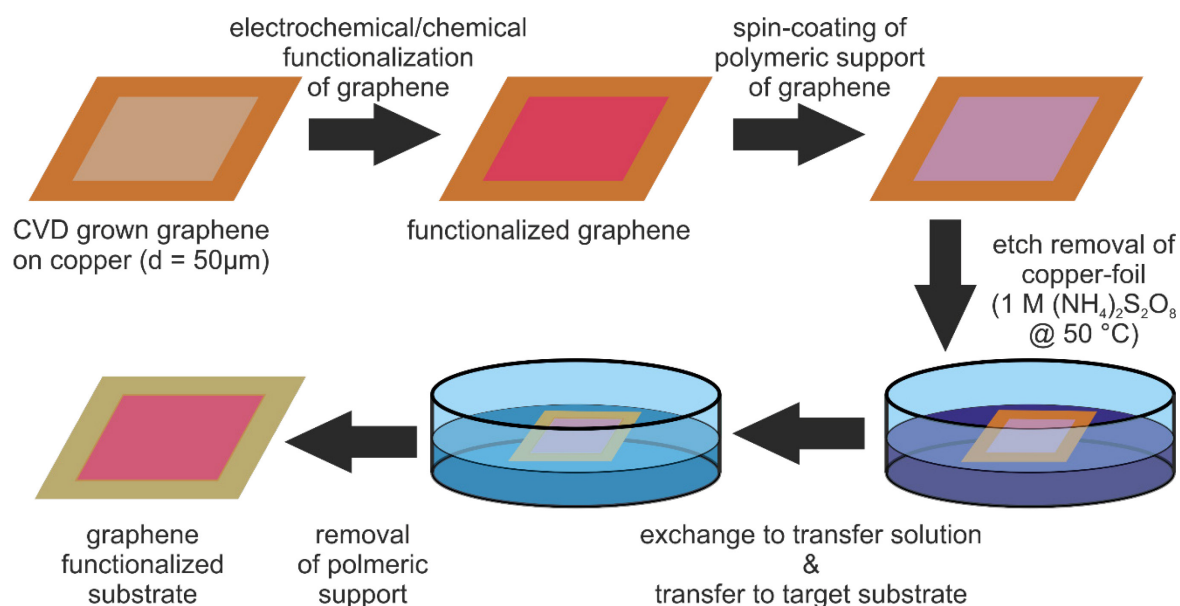


Figure 2-24: Schematic of preparation and transfer of functionalized graphene to the enhancement substrate.

The process is schematically depicted in Figure 2-24. Large area graphene (10 mm x 10 mm) is grown by chemical vapor deposition (CVD) on a copper-foil (d = 50 μm). Covalent modification of the graphene is obtained using electrochemical grafting from a respective diazonium salt and further chemical preparation steps can be performed. For the transfer a support of a polymeric material on nitrocellulose-base is spin-coated onto the graphene and the copper is etched away using a solution of 1 M ammonium persulfate at 50°C. After the complete removal of the copper-foil the graphene/support complex is rinsed with deionized water. Then the graphene/support complex is placed on the substrate. In the last step the support material is removed using ethyl acetate and the functionalized substrate is obtained.

The preparation and transfer of the functionalized graphene were not part of this thesis and have been performed in cooperation with the Helmholtz-Zentrum Berlin (HZB). Details on the electrochemical functionalization of the graphene and the transfer can be found elsewhere.¹⁷²⁻¹⁷⁴

2.6. Microfluidics

Microfluidic chips in this work are solely used as a platform to handle small liquid volumes. The theory and development of microfluidics and microfluidic components is a large research topic which shall not be discussed here. For more information the interested reader may be referred to one of the many books and publications on this topic.¹⁷⁵⁻¹⁸¹

The microfluidic chips mainly used in the optofluidic platform are depicted in Figure 2-25.

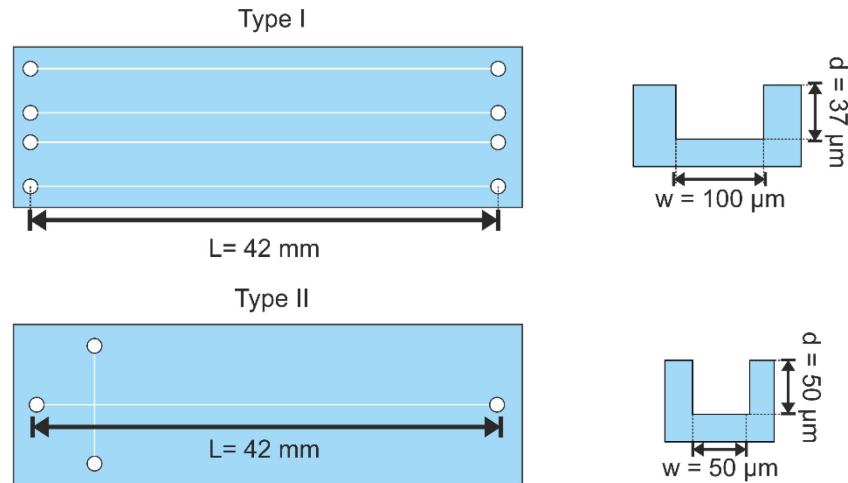


Figure 2-25: Schematic top and cross section view of the employed microfluidic chips and channels. Type I: Microfluidic chip with four straight channels (dimensions 42 mm x 0.1 mm x 0.037 mm (L x w x d)). Type II: Microfluidic chip with T-junction.

The microfluidic chips used in this work were fabricated from the elastomer polydimethylsiloxane (PDMS), if not stated otherwise, using soft-lithography in a master replica scheme for their fabrication.^{182, 183}

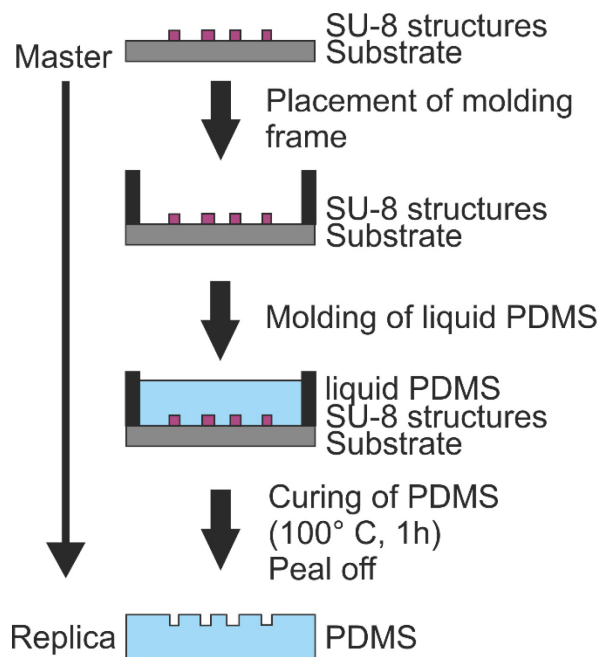


Figure 2-26: General scheme of master-replica fabrication method for microfluidic chips.

Figure 2-26 shows the general scheme of master-replica fabrication for microfluidic chip fabrication with PDMS. The masters for the microfluidic chips utilized in this thesis were fabricated with photolithographic methods to obtain a negative image of the microfluidic channels in the

photopolymer SU-8. The design of the microfluidic channels was provided by Dr. Dirk Janasek and the employed master and was produced at the ISAS Dortmund. A molding frame with the dimensions of the chip (78 mm x 22 mm) was placed on the master and subsequently the liquid mixture of PDMS and curer (10:1) was filled into the frame. The mixture of PDMS and curer was out-gassed in a desiccator for at least 1 h prior to its use. The PDMS was cured for 30 min at 100° C to solidify. Afterwards the microfluidic chip were removed from the master. The connection holes for the fluid inlet and outlet were punched into the microfluidic chip using a hole-puncher with an outer-diameter of 1 mm.

Sample delivery to the microfluidic chip was achieved using a syringe pumps (World Precision Instruments AL1000-220) with disposable syringes (Becton-Dickinson) of 10 mL, 5 mL and 1 mL volume and disposable hypodermic needles (Terumo AGANI™ Needle, 0.5x25 mm). The connection between the microfluidic chip and the syringe was realized using Teflon tubes (Diagonal, OD 1 mm, ID 0.5 mm).

Theoretical calculation of the flow conditions and flow velocity in the microfluidic channels were performed using the Flow Simulation package (Flow Simulation 2014 SP4.0 Build:2765) of SolidWorks® 2014.

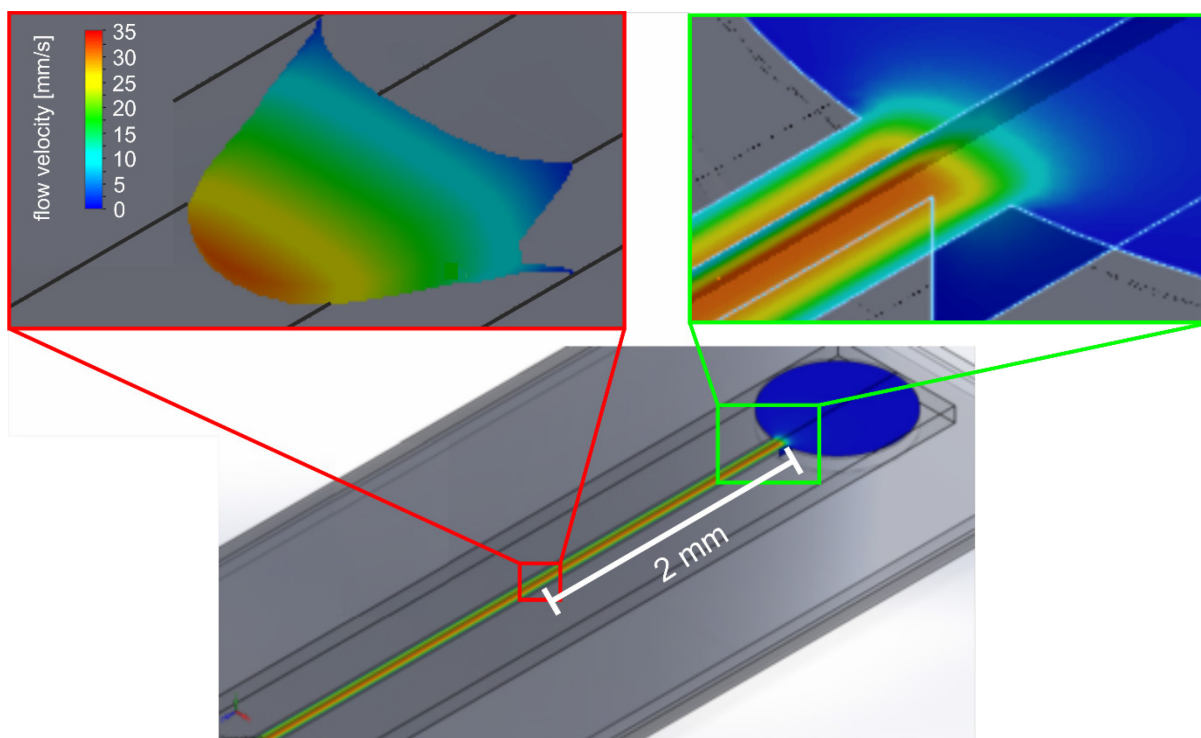


Figure 2-27: Simulation of flow-velocity distribution in the vicinity of the inlet of the microfluidic chip of type I with a volume flow rate of 0.2 ml/h at the inlet. (Left inset) Flow velocity profile in 2 mm distance from the inlet. (Right inset) Zoom in the transition zone between the inlet and the microfluidic channel.

Results of the theoretical analysis of the flow velocity distribution within the microfluidic channel as well as in the transition zone from the inlet to the microfluidic channel are shown in Figure 2-27. The depicted flow velocity distribution follows a 2D Hagen-Poiseuille flow profile as expected for a laminar flow in the microfluidic channel.¹⁸⁴ This fully developed flow profile can already be found in close proximity to the inlet. Therefore, a laminar flow of the analyte can be assumed over the whole length of the measurement channel. At a volume flow rate of 0.2 ml/h at the inlet a maximum flow velocity of 35 mm/s is expected at the center of the channel. At the edges of the channel, which are important for the interaction with the interface and therefore for the detection, a flow velocity of 10 mm/s was predicted. This will ensure a sufficient exchange of the sample to provide a constant concentration of the analyte in the measurement volume in the course of the experiment.

3. Realization of an optofluidic platform for IR microscopy

The combination of enhancement substrates and microfluidics in IR microscopy will enable one to perform highly sensitive *in situ* SEIRA spectroscopy at the solid—liquid interface with sub- μL sample volumes. Such a combined system may help to exploit the high sensitivity of *in situ* IR spectroscopy for the analysis and study of biologically relevant samples and systems. Different concepts for the integration of IR spectroscopy with microfluidics have been presented relying either on a transmission^{54-58, 60, 185, 186} or an ATR geometry^{61, 63, 187}, a recent overview of the developments can be found in the review by Perro *et al.*⁵³ The integration of SEIRA spectroscopy with metal island film substrates with microfluidics in a specular reflection has however not been reported yet.

The concept developed in this thesis has been submitted as a patent proposal.¹⁸⁸ It relies on measurement of a specular reflection under non-ATR conditions at the solid—liquid interface between the enhancement substrate and the microfluidic channel. Such a geometry circumvents the strong absorption in the IR of materials as *e.g.* of the polymer or glass commonly used in the fabrication of microfluidic chips, enabling the application of such microfluidic chips in the experiment. It furthermore evades the potentially strong absorption of the liquid environment within the microfluidic channel if aqueous solutions are to be investigated. The adsorption of the solvent imposes design limitations for the design of a cell for transmission measurements, limiting the channel depth to approx. less than 10 μm . The proposed concept does not require any additional optics as would be required *e.g.* to realize ATR conditions at the solid—liquid interface and can be used with simple planar IR transparent substrates *e.g.* in a conventional IR microscopes. High sensitivity for *in situ* experiments is obtained by integration of enhancement substrates of metal island film functionalized substrates in order to perform SEIRA spectroscopy. Such substrates mediate a broad-band enhancement over the whole IR spectral range and are compatible to thin film preparation techniques.

The described concept demanded the development of a suitable optofluidic platform which is compatible with standard IR microscopes and allows for the combination of the microfluidic chip and the enhancement substrate. The following chapter presents the optofluidic platform developed to realize the detection concept described above. The effective measurement area and volume of such a cell has been determined and exemplary *in situ* IR and SEIRA measurement with the presented optofluidic platform are shown.

3.1. Layout of the optofluidic platform

The results presented in this section have been published in ACS Sensors: Kratz, C., Furchner, A., Oates, T. W., Janasek, D., & Hinrichs, K. (2018). Nanoliter Sensing for Infrared Bioanalytics. ACS sensors, 3(2), 299-303. DOI: 10.1021/acssensors.7b00902

Figure 3-1 schematically shows developed optofluidic platform system.

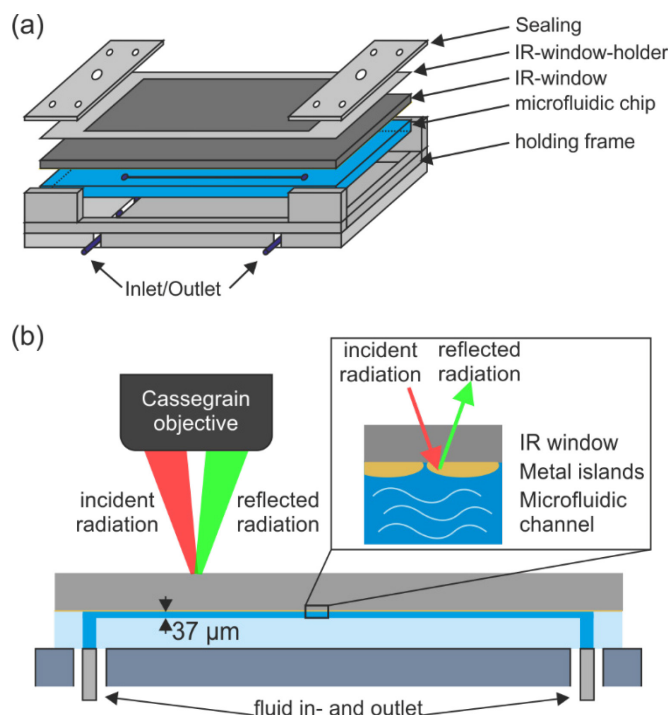


Figure 3-1: Schematic drawing of optofluidic platform. (a) Assembly drawing of optofluidic platform. (b) Cross-sectional view of optofluidic platform. Inset: Zoom on detection layer

As depicted in Figure 3-1 (a) the platform comprises a holding frame to combine the microfluidic chip with an IR window of choice. The channels of the microfluidic chips are open on the top side and sealed leak tight by the IR window by applying pressure. Sample delivery to the microfluidic channels is realized via connections on the backside of the microfluidic chip. The cross-sectional view shown in Figure 3-1 (b) illustrates the general detection setup. The IR radiation is focused using a Cassegrain objective (NA = 0.4, spot-diameter $\approx 160 \mu\text{m}$) of an IR-microscope (Bruker Hyperion 3000) onto the interface between the microfluidic chip and the IR-window. An aperture is used to limit the illuminated area to approx. $160 \mu\text{m} \times 160 \mu\text{m}$. Measurements are performed in a single-reflection at the solid—liquid interface under non—ATR conditions. As a result of the refraction at the interface between air and IR window the median incident angle at the solid—liquid interface is 4.7° for a silicon window ($n_{\text{Si}} = 3.42$).

3.2. Effective measurement area in *in situ* measurements

In consequence of the refraction of the incident radiation at the front-side of the IR window and the focal depth the measurement spot-diameter changes compared to a measurement on the top-surface of the IR window. This effect has been evaluated for the standard IR window, a 0.8 mm thick double side polished silicon wafer (Vario Kristallbearbeitung GmbH), used in the experiments. In the evaluation a spot-size of $160\ \mu\text{m} \times 160\ \mu\text{m}$ has been assumed.

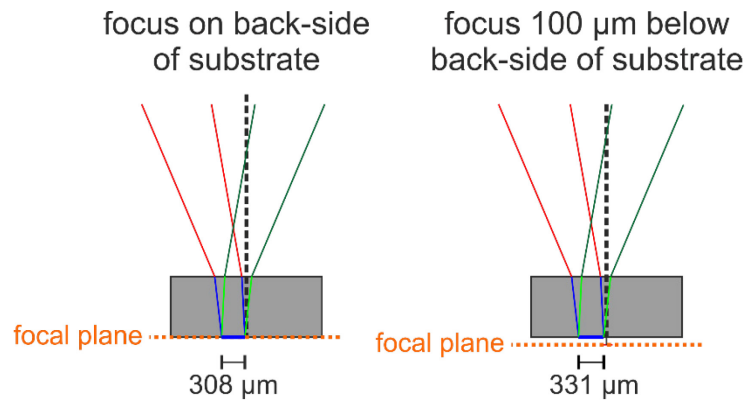


Figure 3-2: Dependence of measurement spot-size on focus depth. Assumed spot diameter $160\ \mu\text{m}$ in air, thickness of substrate $0.8\ \text{mm}$, refractive index of IR window $n_{\text{Silicon}} = 3.42$.

Taking the refraction at the first interface into account the diameter of the measurement spot varies depending on the focus-depth by $0.23\ \mu\text{m}$ per $1\ \mu\text{m}$ change in the depth of the focal plane.

Under these considerations the size of the measurement area probed during the experiments has been estimated.

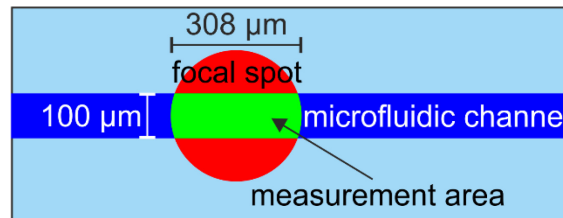


Figure 3-3: Measurement area on microfluidic channel during *in situ* measurements with the optofluidic platform marked in green and indication of defining dimensions used for the calculation.

The green area in Figure 3-3 corresponds to the area where the measurement spot of the microscope overlaps with the microfluidic channel. This area is the effective measurement area assumed in the experiments.

In the experiments the height of the sample stage is adjusted so that a sharp focus on the top-side of the substrate is obtained. Then the sample stage is raised further towards the objective a distance equivalent to the thickness of the substrate. Assuming a thickness of the substrate of $(800 \pm 20)\ \mu\text{m}$ the measurement area corresponds to $(3.0 \pm 0.5) \times 10^{-2}\ \text{mm}^2$. For the microfluidic chip of type I (comp. section 2.6) with a channel depth of approx. $(37 \pm 2)\ \mu\text{m}$ this corresponds to an effective sampling volume of $(1.1 \pm 0.2)\ \text{nL}$.

3.3. Measurements with the optofluidic platform

In order to show the applicability of the optofluidic platform for *in situ* IR and SEIRA measurements, test measurements have been performed. In the beginning IR spectra of common solvents have been collected with a double side polished silicon window ($d = 0.8$ mm) without a metal island film.

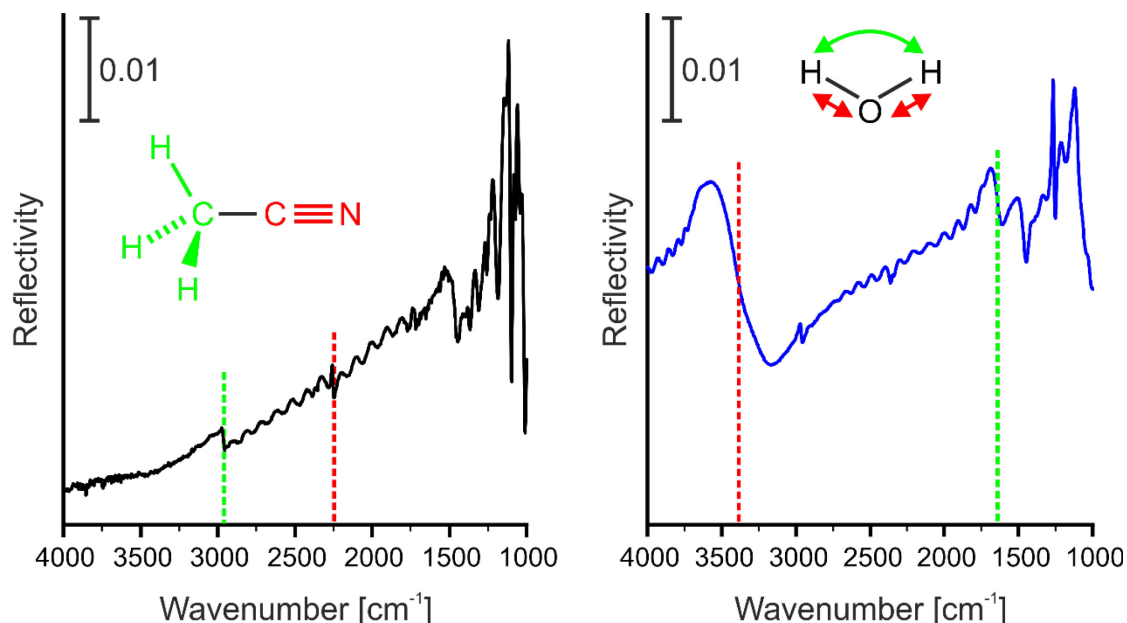


Figure 3-4: Exemplary IR microscopic reflectivity spectra of a microfluidic channel filled with acetonitrile (left) and water (right).

Figure 3-4 shows exemplary spectra of acetonitrile and water recorded with the optofluidic platform on a PDMS microfluidic chip (type I). Distinct vibrational bands of the solvents can be identified in the spectra as indicated. In addition to the vibrational signature the measured spectra show oscillations in the spectral regions where no molecular absorption is observed. The observed oscillations in the spectrum are the result of multiple reflection interference within the microfluidic channel and can potentially be used as a complementary access to information on changes at the solid-liquid interface.¹⁸⁹⁻¹⁹¹

The capability for *in situ* SEIRA measurements has been evaluated using a gold island film functionalized silicon substrate (double side polished, $d = 0.8$ mm) with a SAM of 4-mercaptobenzonitrile (4-MBN).

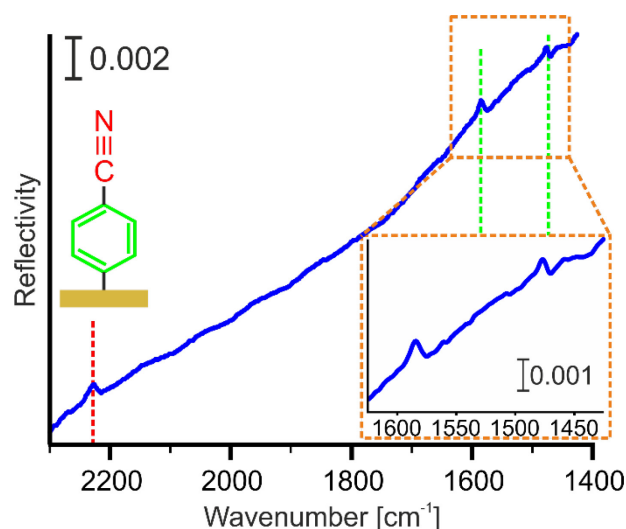


Figure 3-5: *In situ* SEIRA microscopic reflectivity spectrum of a 4-MBN monolayer on a gold island film in ethanol recorded with the optofluidic flow cell and indication of vibrational bands associated with the SAM.

Figure 3-5 shows an *in situ* SEIRA microscopy spectrum of the 4-MBN SAM in ethanol. The typical vibrational bands of 4-MBN, the stretching vibration of the nitrile group $\nu(\text{C}\equiv\text{N})$ around 2227 cm^{-1} and ring vibrations around $\nu(\text{ring})$ 1585 cm^{-1} and $\nu+\delta(\text{ring})$ 1477 cm^{-1} ¹⁹² can be identified, illustrating that the concept can provide monolayer sensitivity under *in situ* conditions.

The shown exemplary measurements demonstrate that the optofluidic platform can be used for *in situ* spectroscopy with and without enhancement substrates. Characteristic vibrational signatures of common solvents can be identified in the IR spectra recorded in the small effective sampling volume of the microfluidic channel. Under the utilization of enhancement substrates the vibrational signal of a SAM with thicknesses of less than 1 nm was detectable under *in situ* conditions. In consequence the developed optofluidic platform is suitable for the designated application.

4. Results & Discussion

In the following chapter results of the performed studies are presented and discussed.

The first section focuses on investigations concerning the employed enhancement substrates of gold island films. Substrates with a gradient in gold film thickness, termed gradient substrates, are presented and used to study the correlation between island film morphology, effective film thickness, plasmonic and enhancement properties under *ex situ* conditions. A quantitative approach for *a priori* assessment of the enhancement of gold island films on silicon substrates is presented and the possibility for on-substrate tuning of the enhancement to the needs of the experiment is demonstrated. Furthermore the formation of SAMs of thiolate molecules on contaminated surface has been studied as well as the effect of the SAM formation on the plasmonic properties of the substrates. In the last part the applicability of the model for the optical simulation of metal island films with different island film geometries proposed in section 2.4.4 has been evaluated.

In the second section the developed optofluidic platform has been employed to perform *in situ* SEIRA spectroscopy studies of monolayers at the solid—liquid interface, investigating the formation kinetics and reaction to environmental stimuli. Adsorption kinetics of monolayer self-assembly of model molecules 4-MBN and GSH as well as the recognition of streptavidin on a biotinylated enhancement substrate have been investigated. The experiments enabled to determine adsorption rate constants and to demonstrate sub-monolayer sensitivity of the presented detection concept. A Limit of detection (LOD) under simplifying assumptions on the order of few ng/cm^2 could be obtained for the model compounds. The dissociation and protonation of the carboxylic groups in an approx. 1.2 nm thick monolayer of GSH under alkaline and respectively acidic conditions in its environment have been studied, demonstrating the ability to monitor minute changes and potentially their dynamics on the monolayer level.

In the third part a novel route for the surface functionalization of enhancement substrates by transfer of pre-functionalized graphene has been investigated. The effect of graphene transfer on the enhancement performance of the enhancement substrates have been investigated using gradient gold island films. The functionality of these novel hybrid sensor substrates for *ex situ* and *in situ* applications has been studied.

4.1. Enhancement substrates

The enhancement substrates are the key component for SEIRA spectroscopy. The following section shows the results of the performed investigation of enhancement substrates of gold island film substrates.

The introduction of enhancement substrates with a gradient in the effective thickness of gold film allowed to study different island film morphologies on a single substrate. These substrates have been used to study the correlation between the island film morphology, plasmonic properties and the enhancement of the different island film morphologies minimizing the effects of substrate properties, pre-treatment, deposition and preparation of the organic layer. It is shown that such substrates can be used to provide an on-substrate tunability of the enhancement by varying the measurement position.

The gradient gold island film substrates have been used in the investigation of the suitability to use the enhancement of the vibrational signature of the native oxide of the silicon substrates as a material independent *a priori* indicator of the enhancement.

The deposition of SAMs on enhancement substrates contaminated with “advantageous” hydrocarbons has furthermore been investigated. The shift of the plasmonic resonance of the enhancement substrates measured in the UV-Vis spectral region has been studied for three model SAMs.

In the end of the section the results of the implementation of an optical model for the modeling of different island film morphologies found along the gradient substrates is presented.

4.1.1. Correlation between island film morphology and enhancement properties of metal island film substrates

The results in this sub-section have partially been published in Kratz, C., T. W. H. Oates, and K. Hinrichs. "Optimization and quantification of surface enhanced infrared absorption using gradient gold island films." *Thin Solid Films* 617 (2016): 33-37. (<https://doi.org/10.1016/j.tsf.2016.02.019>).

The enhancement of a metal island film substrate strongly depends on the morphology of metal islands forming the film. The morphology herein depends on the deposition parameters of the evaporation, substrate properties and the treatment of the substrate prior to the deposition. Metal island films can be fabricated with a gradient thickness of the gold film by adjustment of the deposition position fabrication protocols (see section 2.3.2). This type of enhancement substrates provides the possibility to realize different island film morphologies on a single substrate. Investigations on such substrates may reduce or eliminate the effects of the substrate and the pretreatment of the substrate in studies of the effect of the different island film morphologies. Gradient island film substrates can be used for SEIRA spectroscopy with an on-chip tunable enhancement. Furthermore they can be used for efficient optimization in the fabrication of homogeneous SEIRA substrate with optimized enhancement properties.

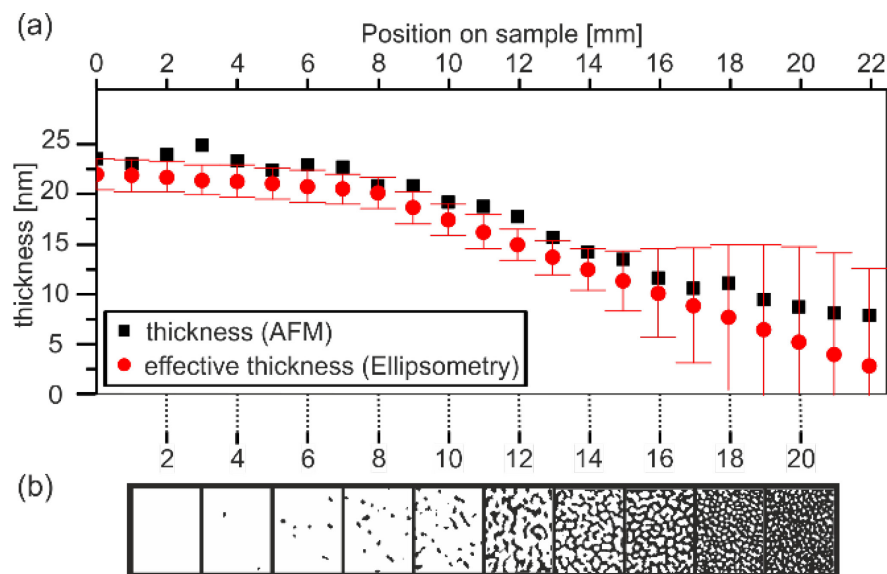


Figure 4-1: Gold island film with gradient thickness of gold. (a) Thickness map along the gradient substrate measured with (■) AFM and (●) fitted effective thickness from UV-Vis ellipsometry. (b) Exemplary SEM pictures recorded along the gradient (2mm step size). The shown SEM images were recorded by Dr. Dimitra Gkogkou at the ZELMI – Zentraleinrichtung Elektronenmikroskopie at the Technische Universität Berlin. Reprinted with permission from Ref. [88].

Figure 4-1 (a) shows exemplarily the gradient in film thickness of the gold layer on a gradient substrate. The film thickness was determined by AFM measurements and by determining an effective thickness from UV-Vis ellipsometry measurements. The effective thickness was determined by fitting a simple three layer optical model (Si/SiO₂/gold) to the measurement data where bulk optical constants have been used in the model. The comparison between the measured thickness and the fitted effective thickness shows good agreement within the error of the fit. For island films with a low coverage of gold, the assumption of the optical model breaks down leading to a strong increase in the uncertainty of the fit and hence the error increases. The comparison between the two complementary techniques shows that UV-Vis ellipsometry in conjunction with optical modeling can be used to efficiently gain access to the film thickness.

Depending on the amount of gold available during deposition different island film morphologies are formed as shown in the exemplary SEM pictures in Figure 4-1 (b). For low amounts, a Volmer-Weber like growth mechanism (see chapter 2.3.1) was observed.¹³⁴ Small isolated gold islands were formed, growing in size and number as more gold was available during deposition. Close to the percolation threshold, AFM measurements suggested a change in the growth mechanism to a Stranski-Krastanov like growth¹⁴¹. At the percolation threshold (Figure 4-1 (a) Pos. 12) the gold islands started to unite, forming a conductive network and remaining holes in the film are subsequently filled with increasing amount of gold available.

Each of these structural domains shows distinctive optical properties. In order to assess these properties the gradient substrate was characterized with UV-Vis ellipsometry in a line scan with micro-apertures (spot-diameter $\approx 250 \mu\text{m}$) and an incidence angle of 70° . From the complex reflectance ratio ρ the pseudo-dielectric function was determined using equation (2-9).

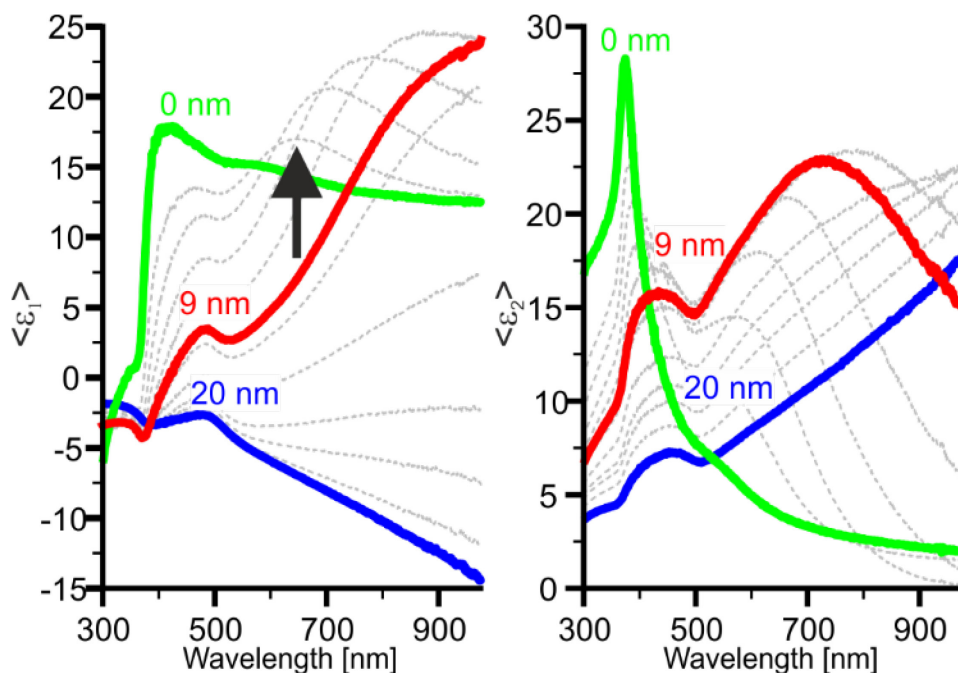


Figure 4-2: Thickness dependent evolution of the real $\langle \epsilon_1 \rangle$ and imaginary $\langle \epsilon_2 \rangle$ component of the pseudo-dielectric function from bare substrate to gold-film. Indicated thickness values of the solid lines are effective thicknesses determined by UV-Vis ellipsometry. Light grey lines show the development in steps of 2 nm increase in effective film thickness. Reprinted with permission from Ref. [88].

The thickness-dependent evolution of the real ($\langle \epsilon_1 \rangle$) and the imaginary ($\langle \epsilon_2 \rangle$) part of the pseudo-dielectric function is shown in Figure 4-2. Interband transitions of the silicon substrate are visible as bands below 400 nm.¹⁹³ The formation of the gold film leads to a reduction in the intensities of these peaks due to increased screening and field interactions between silicon and the gold islands.¹⁹⁴

Induced by the formation of gold islands on the substrate, a plasmonic resonance band can be excited (arrow in Figure 4-2). The plasmon resonance frequency shifts to longer wavelengths and the peak intensity increases with growing film thickness.^{147, 195} The red-shift of the resonance frequency is connected with the growing size of the islands and shows a good agreement with investigations of Feldmann *et al.*¹⁹⁵ for spherical gold clusters. The observed deviations in the red-shift of the plasmonic resonance compared the investigation of Feldmann *et al.* could be a result of the non-spherical shape of the gold islands and the interaction between the silicon substrate and the gold islands.¹⁹⁴ For island films with a high fill factor *i.e.* close to the percolation threshold interparticle coupling may explain further deviations.^{130, 131} The intensity of the plasmonic resonance band is correlated with the number

of islands and reaches a maximum for 9 nm thickness corresponding to a structure very close to the percolation threshold (Figure 4-1 (b) Position 14 mm). Above 12 nm effective film thickness, no plasmonic resonance band is observed since the gold film becomes conductive and no localized plasmonic resonance may be excited (Figure 4-1 (b) Position 12 mm). The assumption of considerable contributions to the effective dielectric function of areas with a closed gold film is supported by the reducing value of the real part of the pseudo-dielectric function for film thicknesses above 10 nm. For film thicknesses above 14 nm it turns negative. This results from a Drude like absorption due to the contribution of free charge carriers. However, the pseudo-dielectric function deviates from the dielectric function found for a closed gold film because of substrate contributions and the fact that in dependence on the morphology an effective medium must be considered. The plasmonic resonance band observed in the intermediate region may originate from strongly enhanced electron scattering in the ultrathin film between the islands.¹¹⁶

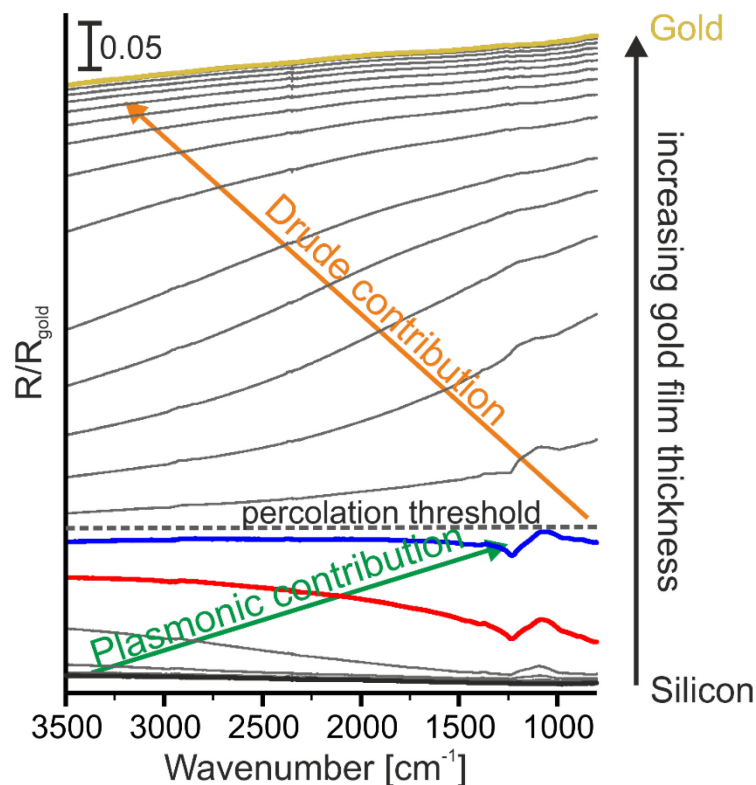


Figure 4-3: IR microscopic reflectance spectra recorded along a gradient substrate. Colored spectra correspond to effective dielectric function in Figure 4-2.

Figure 4-3 shows the effect of the different island film morphologies along the gradient on the measured reflectivity in the IR. The occurrence of a plasmonic resonance, which is shifted from the visible region into the NIR region directly influences the reflectivity of the substrate in the IR. The tail of the plasmonic resonance leads to changes in the reflectivity in the IR. With growing size and density of the island a growing contribution of the island film in the IR is visible which is reflected by the growing reflectivity arising on the high wavenumber side of the spectrum (indicated by the green arrow in Figure 4-3). This is in agreement with the trend observed in the pseudo-dielectric function determined in the UV-Vis spectral region for island films with a thickness below approx. 9 nm as the plasmonic resonance shows a red-shift and seems to extend further into the IR region. Above the percolation threshold a Drude-like contribution from free charge carriers comes into play which increases the reflectivity on the low-wavenumber side of the spectrum (indicated by the orange arrow). As the island character is lost with an increasing amount of gold the Drude-like contributions

of free charge carriers start to dominate the reflectivity spectrum, until for a closed gold film a metal like reflection is observed.

In order to evaluate the enhancement performance for SEIRA in dependence on the film thickness a self-assembled monolayer of 4-Mercaptobenzonitrile (4-MBN)¹⁹² was deposited on the gradient substrate (see section 2.5.1). 4-MBN was used as a model system because the stretching vibration ν ($C\equiv N$) of the nitrile group shows no overlap with vibrational bands of neither water nor CO_2 .

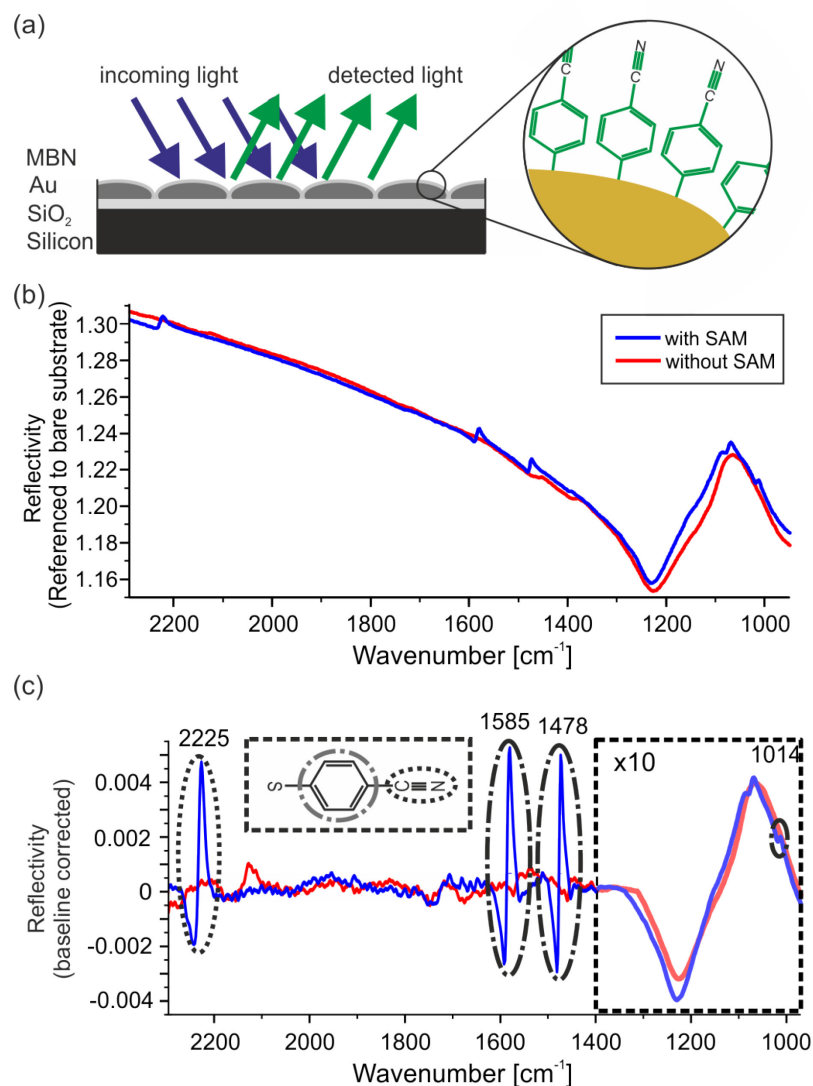


Figure 4-4: Evaluation of SEIRA activity of gradient island film substrate. (a) Schematic setup of IR measurements with a SAM of 4-MBN on a gold island film. (b) IR-microscope reflection spectra of unmodified and modified gradient substrate at position of maximum SEIRA activity. (c) Baseline corrected IR-microscope reflection spectra of MBN film on gradient substrate with maximum SEIRA enhancement with identification of central frequencies of vibrational bands of 4-MBN. Baseline correction was performed using a “rubber-band” method.¹⁹⁶ For better comparison the spectrum in the spectral range of the native oxide band (dashed box) was scaled down by a factor of 10. Reprinted with permission from Ref. [88].

Figure 4-4 (a) shows a schematic of the investigated structure, a SAM of 4-MBN on top of the gold island film on the native oxide of the silicon. The zoom on the right side indicates the bonding of 4-MBN via the interaction of the sulfur with the gold of the island.¹⁹² The spectra (Figure 4-4 (b)) were recorded at the position on the substrate where maximum enhancement of the vibrational bands of the MBN was observed. In consequence of the coupling between the vibrational band of the molecule

and the plasmonic resonance the observed vibrational bands show a Fano-like resonance typical for SEIRA spectroscopy.^{111, 117, 136}

The characteristic vibrational bands of the 4-MBN were identified in the baseline corrected spectra shown in Figure 4-3 (c). The band of the nitrile stretching vibration $\nu(\text{C}\equiv\text{N})$ was identified at 2225 cm^{-1} .¹⁹² The bands of the phenylene group were assigned using a best fit to the vibrational bands of unsubstituted benzene.¹⁹⁷ The vibrational band of the ring stretching $\nu(\text{ring})$ was found at 1585 cm^{-1} , combined ring stretching and deformation $\nu+\delta(\text{ring})$ at 1478 cm^{-1} and ring breathing at 1014 cm^{-1} . A spectral signature of the substrate's native oxide was observed between 1000 cm^{-1} and 1300 cm^{-1} .

The combination of UV-Vis ellipsometry and IR measurements on a single gradient substrate allowed for an investigation of the correlation between SEIRA activity and film thickness of the gold island film (Figure 4-5). SEIRA activity was herein quantified by the amplitude of the vibrational band of the nitrile stretching vibration. The amplitude is determined as the minimum to maximum peak-height of the Fano-shaped peaks. Average noise intensity was determined by the evaluation of the noise in the vicinity of the band. The noise-level in the plot is defined according to the 3σ criterion.

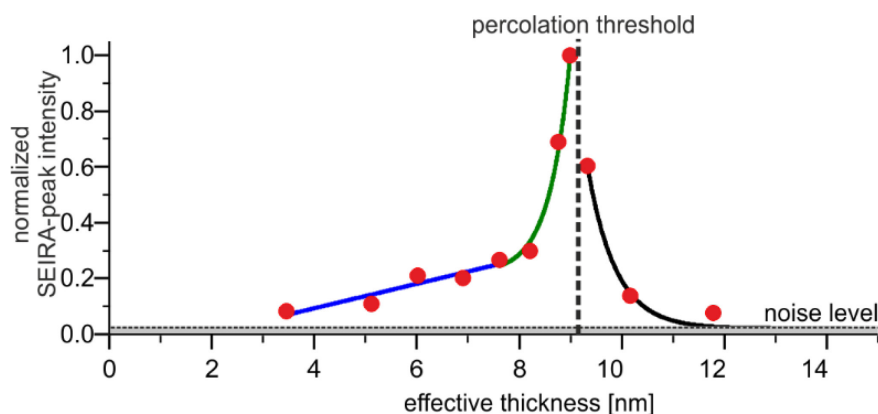


Figure 4-5: SEIRA activity quantified by measured band amplitude of the nitrile vibrational band $\nu(\text{C}\equiv\text{N})$ of a SAM of 4-MBN in dependency of film thickness. Adapted from Ref. [88]

For an effective gold film thickness above 2.5 nm SEIRA enhancement is observed which increases with growing thickness showing an almost linear trend (blue curve). For a thickness above 7.5 nm SEIRA activity increases non-linearly towards the percolation threshold at about 9 nm film thickness and sharply decreases with a non-linear trend for larger thicknesses. In agreement with *e.g.* Osawa *et al.*⁹⁷ the strongest SEIRA activity is observed very close to but before the percolation threshold is reached. After the percolation threshold was crossed a diminishing SEIRA activity was observed in agreement with Fahsold *et al.*¹¹⁶

In Figure 4-5 the trend of observed SEIRA activity for values from 7.5 nm thickness to the last point before the percolation as well as for the points after the percolation threshold could be described by exponential functions (green and black curve). Above 12 nm film thickness no SEIRA activity was observed.

A comparison between the pseudo dielectric function (Figure 4-2) and measured SEIRA activity (Figure 4-5) supports the assumption of a direct linkage between SEIRA activity and the observed behavior of the plasmonic resonance of the gold island film. The occurrence of maximum SEIRA activity coincides with a maximum in the intensity and red-shift of the plasmonic resonance for an effective film thickness of about 9 nm.¹⁹⁸ Theoretical analysis of connection between the plasmonic resonances of SEIRA active substrates and the observed enhancement support this correlation.¹⁹⁹ However it has to

be noted that other effects as *e.g.* chemical enhancement (compare section 2.3.1) may also contribute to the SEIRA effect.⁹⁷

The study shows that gradient island films can be used to study the effect of different island film morphologies on optical and enhancement properties on a single substrate eliminating possible effects of varying substrates and pre-processing. Gradient island films enable to tune the enhancement on-substrate and may allow achieving optimized enhancement conditions by simple adjustment of the measurement position. This may especially be of advantage when a sample is only available in small quantities as a single preparation of a substrate may suffice for optimized SEIRA characterization. Furthermore the island films may be used to determine the optimum effective film thickness of the fabrication process for the formation of metal-island film morphologies optimized for SEIRA enhancement. As shown UV-Vis ellipsometry and a simple optical model may be used for fast optimization and validation.

4.1.2. *A priori* quantification of SEIRA enhancement

The results in this sub-section have partially been published in Kratz, C., T. W. H. Oates, and K. Hinrichs. "Optimization and quantification of surface enhanced infrared absorption using gradient gold island films." *Thin Solid Films* 617 (2016): 33-37. (<https://doi.org/10.1016/j.tsf.2016.02.019>).

In the application of metal island films for SEIRA spectroscopy a material independent *a priori* determination of the enhancement provided by an enhancement substrate as well as the optimization of the enhancement remain a key challenges.¹⁰⁴ The enhancement provided by a substrate can often only be analyzed after the molecule of interest has been deposited and may depend on the molecule of interest. As a result it often takes elaborate efforts to optimize the enhancement properties of the substrates, requiring the repeated deposition of the material of interest on multiple substrates. The use of gradient substrates may (*vide supra*) provide a possible alternative for this optimization but would still require the deposition of the material of interest. It would therefore be of advantage to have a marker which gives an *a priori* indication of the enhancement. On the one hand this would provide a way to determine the enhancement independently of the molecule of interest. On the other hand an optimized measurement position on gradient substrates could be chosen prior to the deposition of the material of interest.

As shown before the vibrational signature of the native oxide on a silicon wafer is enhanced by the metal island film. This vibrational band may be a suitable candidate for an *a priori* indicator of the enhancement as the native oxide is an inherent component of silicon substrates. In consequence the correlation between the enhancement of this vibrational signature and the enhancement of the vibrational bands of organic molecules on the enhancement substrate has been investigated. The aim of this study was to show that the native oxide signature can be used to determine the optimum measurement position on a gradient substrate. In a second step its applicability as a compound independent *a priori* indication of the provided enhancement was studied.

In the experiment it was observed that the vibrational signature assigned to vibrations of the native oxide is enhanced along with the vibrational bands of the molecule of interest. The observed signature of the native oxide is a strong spectral feature between 1300 cm^{-1} and 1000 cm^{-1} . It may be associated with the Rest-strahlen band of the native oxide and may contain further components resulting from effects of the strong oscillator⁵⁰ and varying other contributions.²⁰⁰ The enhancement of this bands can be expected as an over-layer configuration¹⁰⁶ is realized for the native oxide layer. Analysis of the IR spectra recorded along the gradient substrate showed that the enhancement of the silicon oxide vibration seems to be correlated with the enhancement of the vibrational bands of the deposited molecule (Figure 4-6).

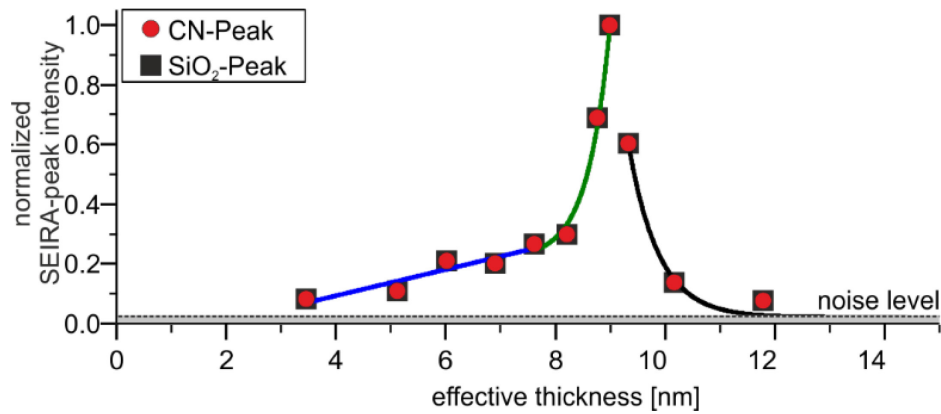


Figure 4-6: Normalized peak-intensity of vibrational modes of $\nu(\text{C}\equiv\text{N})$ of 4-MBN (red dots) and vibrational band of the native oxide (black squares). Reprinted with permission from Ref. [88]

As shown in (Figure 4-7) the vibrational signature of the native oxide can be analyzed prior to the deposition of the material of interest. The deposition of the organic layer on top of the metal island film may have an effect on the amplitude of the native oxide signature. The evaluation of the signature amplitude after the deposition may however be complicated if it overlaps with a molecular vibration as it is the case for a SAM of 4-MBN.

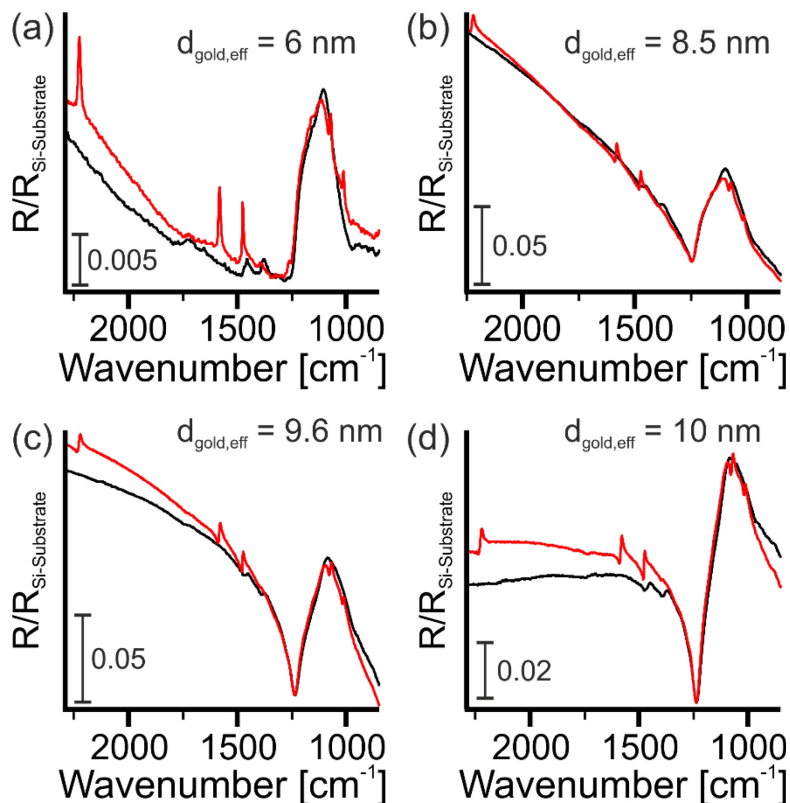


Figure 4-7: Position dependent enhancement on a gradient gold island film at four different positions along the gradient. (black) Spectra recorded priori to SAM deposition and (red) spectra recorded after SAM deposition

The deviations in the shape and amplitude of the vibrational signature of the native oxide with and without a 4-MBN SAM are due to the presence of two vibrational bands of the 4-MBN overlapping with the vibrational band of the native oxide.

In order to investigate whether the vibrational signature of the native oxide can be used as an *a priori* indicator of the enhancement for gold island film substrates eight gradient substrates have been

prepared. SAM monolayer of 4-MBN and 4-mercaptobenzoic acid (4-MBA) have been prepared on the substrates by immersion of the samples for 24 hours. IR spectra of all samples were recorded by mapping IR-microscopy before and after the formation of the SAMs with a step-size of 1 mm. The gradient substrates were scanned from the thick gold side to the silicon side showing on average a gradient from 23 nm effective gold film thickness to blank silicon as determined by UV-Vis ellipsometry. The structure of the molecules along with corresponding SEIRA spectra are shown in Figure 4-8. The vibrational bands used for the analysis are marked in the spectra.

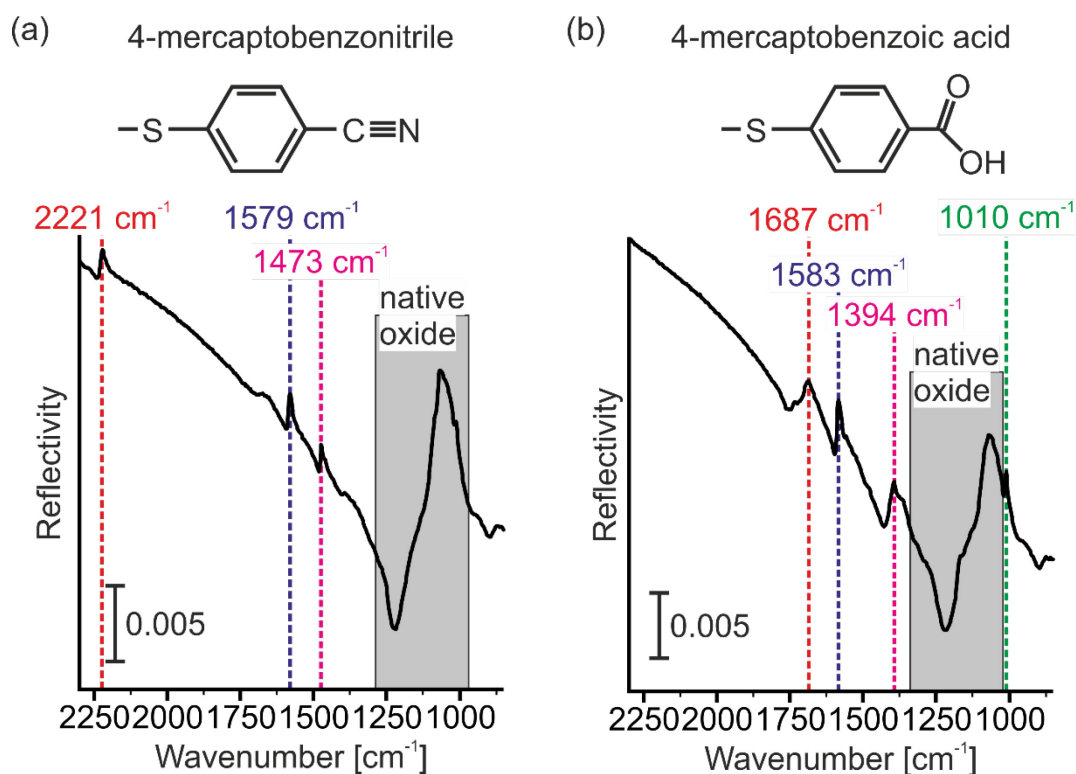


Figure 4-8: Molecular structure of and IR microscopic SEIRA spectra of (a) 4-MBN and (b) 4-MBA with indication of the vibrational bands used for the analysis.

The amplitudes of the indicated vibrational bands were determined at each measurement position for the indicated vibrational bands, taking the difference between the maximum and the minimum reflectivity value. The values of the vibrational band amplitudes of the organic layer was then compared to the amplitude of the vibrational band of the native oxide determined from the measurement before SAM formation. In order to allow for a direct comparison of the position where maximum enhancement of the vibrational bands was observed, the amplitudes of each band were normalized. The results of this evaluation are shown exemplarily in Figure 4-9 for three of the 4-MBN and in Figure 4-10 for three of the 4-MBA coated gradient substrates. The same results were found on the samples not shown here.

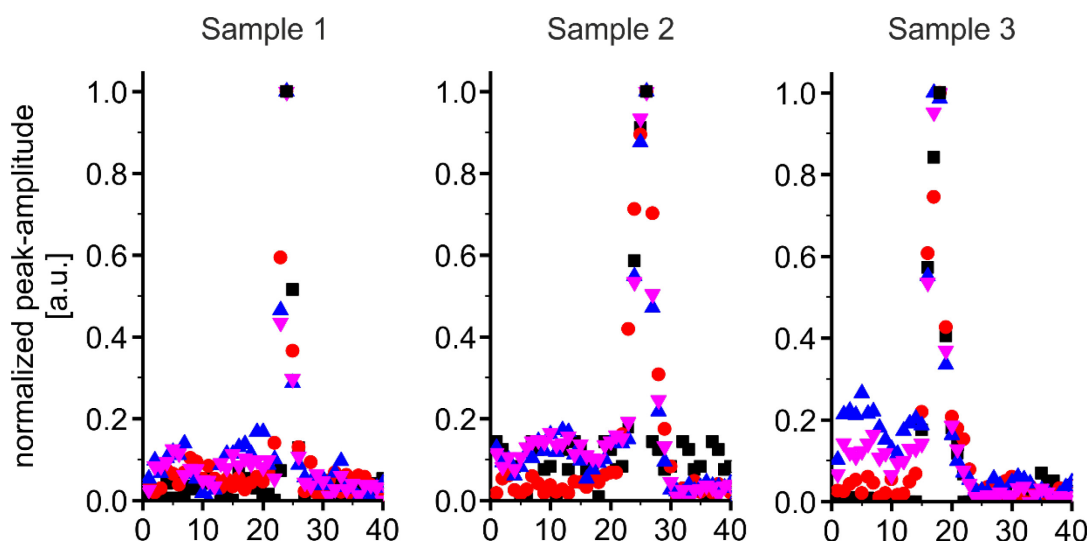


Figure 4-9: Normalized peak amplitude of molecular vibrations of 4-MBN after and of the native oxide vibration before SAM formation in dependence of the measurement position on three different gradient substrates. The colors of the symbols correspond to the indication of the vibrational bands in Figure 4-8.

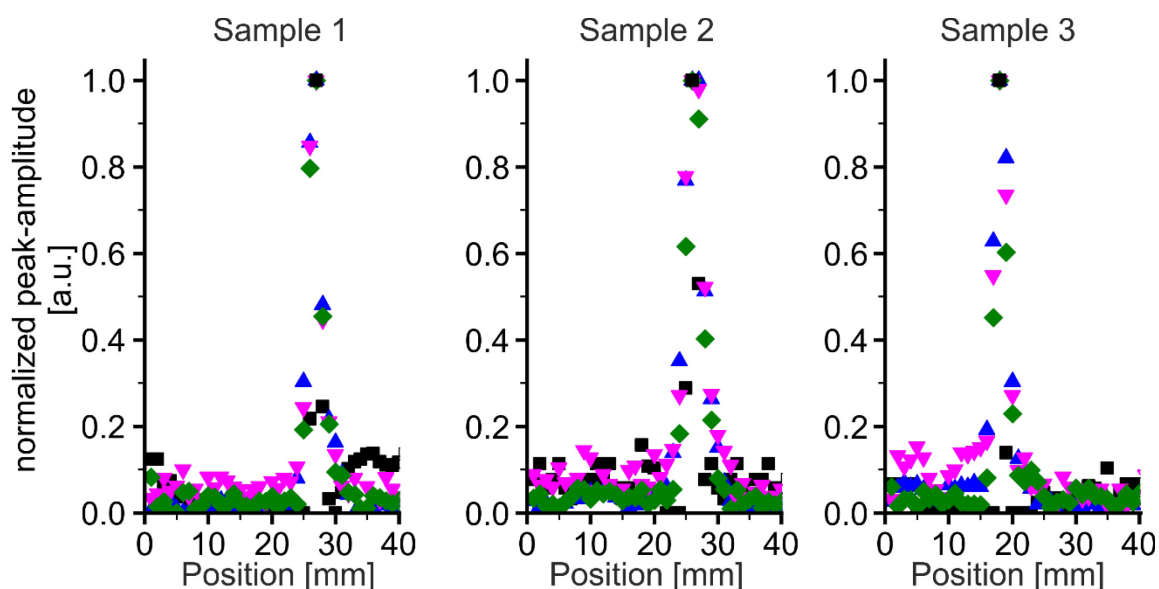


Figure 4-10: Normalized peak amplitude of molecular vibrations of 4-MBA after and of the native oxide vibration before SAM formation in dependence of the measurement position on three different gradient substrates. The colors of the symbols correspond to the indication of the vibrational bands in Figure 4-8

On all investigated samples the position where maximum enhancement of the native oxide signature was observed before the formation of the SAM coincides with the position where maximum enhancement of the vibrational bands of the molecules of the SAM was determined. The analysis of the vibrational signature of the native oxide therefore is an appropriate method to determine an optimized measurement position on a gradient substrate and may serve as a qualitative *a priori* indicator of the enhancement.

The enhancement of the native oxide signature seems to be correlated with the enhancement of the vibrational bands of the organic molecule. This is exemplarily shown in Figure 4-11 for the position where maximum enhancement was observed on the investigated gradient island film samples for the ring vibration of 4-MBN around 1579 cm^{-1} and 4-MBA around 1583 cm^{-1} .

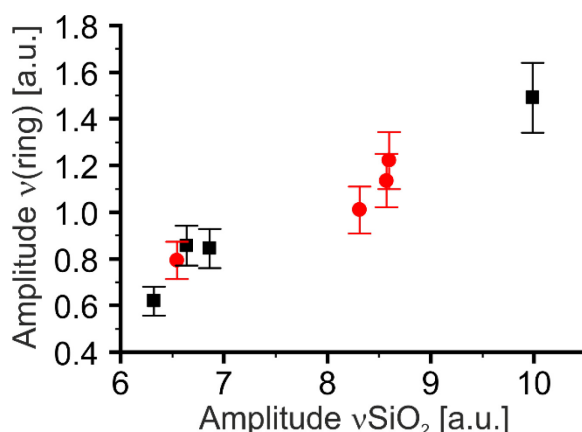


Figure 4-11: Correlation between the amplitude of the vibrational band of the native oxide before the deposition of the SAM and the ring vibration of (■) 4-MBN around 1579 cm^{-1} and (●) 4-MBA around 1583 cm^{-1} of the SAMs.

The correlation between the enhancement of the vibrational bands and the enhancement of the native oxide signature has been investigated in more detail exemplarily for the 4-MBN gradient substrates. The enhancement factors were calculated using the method presented in section 2.3.4.

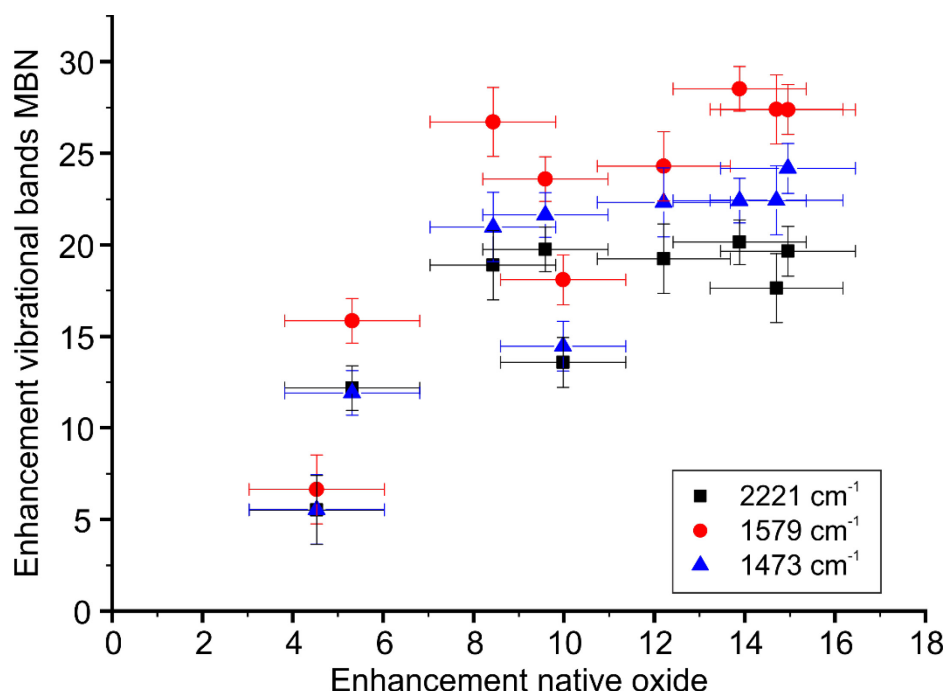


Figure 4-12: Correlation between the enhancement of the vibrational bands of 4-MBN and the enhancement of the vibrational signature of the native oxide

The analysis shows that the enhancement of the vibrational signature of the native oxide shows a type of correlation to the enhancement of the vibrational bands of the 4-MBN. However the scattering of the obtained data points is much too large to evaluate the correlation further.

In order to use the enhancement of the vibrational signature of the native oxide as a quantitative measure of the enhancement the variation in the components of the vibrational signature as well as the differences in the native oxide layer from substrate to substrate have to be taken into account. Also a larger set of samples could help to use statistical methods for the determination of the correlation.

The analysis showed that the enhancement of the vibrational signature of the native oxide may be used as a qualitative *a priori* indicator of the enhancement. It may be used to determine the optimum measurement position on a gradient substrate and give an indication of the enhancement the substrate may provide. The analysis of the correlation between the enhancement of the vibrational signature of the native oxide and the enhancement of the vibrational bands of the molecules of interests on different gradient island film substrates illustrated that it may also serve as a quantitative indicator of the enhancement if further studies were to be performed.

4.1.3. Self-assembled monolayer formation on contaminated surfaces

A problem often encountered in the vacuum preparation of metal island films is the contamination of the surface by organic molecules which may be a consequence of the pre-cleaning, preparation or from exposing the sample to air.¹¹⁰ The contaminations present on the gold island film substrates typically contain hydrocarbons with $-CH_2$ and $-CH_3$ functional groups with absorption bands in the region between 3000 cm^{-1} and 2800 cm^{-1} for the stretching vibration of these groups and below 1500 cm^{-1} for the deformation vibrations. Additionally other contaminations containing carbonyl (C=O) or other functional groups may be identified in the spectra recorded of the enhancement substrates after deposition of the gold island film and exposure to air (see *e.g.* Figure 4-13). These absorption bands may potentially influence the evaluation and interpretation of the measurements in the spectral regions where an overlap of vibrational bands from the contaminations and the molecules of interest occurs. The formation of a SAM of thiolate molecules on the gold surface however does not seem to be affected by the contaminations on the surface. It rather seems as if the contaminations are removed from the surface by the formation of the SAM.

This effect has been investigated in the following. Gold island film substrates have been fabricated and characterized with IR microscopy before and after the deposition of SAMs of 4-MBN and GSH. The SAMs were prepared by immersion of the samples overnight ($t_{\text{immersion}} > 12\text{ h}$) in a 1 mM solution of 4-MBN in ethanol and in a 5 mM solution of GSH in DI-water respectively.

In the first experiment 4-MBN was chosen as it forms relatively dense SAMs (surface density $\Gamma_{4\text{-MBN}} \approx 5.3 \times 10^{-10}\text{ mol/cm}^2$)¹⁰⁹ and does not contain any functional groups of $-CH_2$ nor $-CH_3$.

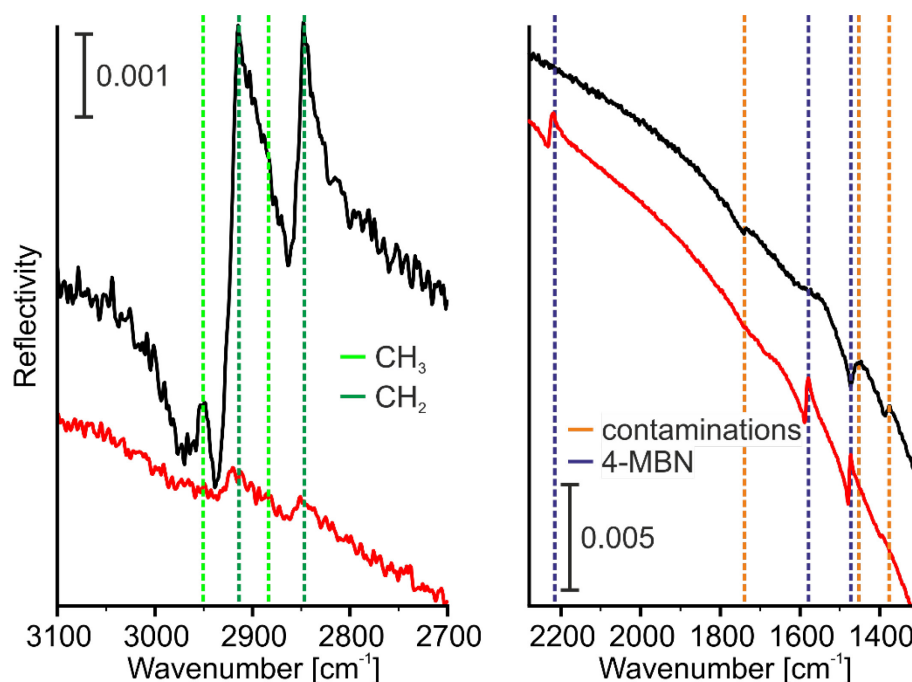


Figure 4-13: Formation of 4-MBN SAM on contaminated gold island film substrate. SEIRA spectra of the enhancement substrate before (—) and after (—) deposition of 4-MBN SAM from solution.

In the IR reflectivity spectra measured before the deposition of the SAM (Figure 4-13 black line) vibrational bands of the contaminations with hydrocarbons ($\nu_{\text{as}}(\text{CH}_2) = 2915 \text{ cm}^{-1}$, $\nu_{\text{s}}(\text{CH}_2) = 2847 \text{ cm}^{-1}$, $\nu_{\text{as}}(\text{CH}_3) = 2950 \text{ cm}^{-1}$, $\nu_{\text{s}}(\text{CH}_3) = 2885 \text{ cm}^{-1}$, $\delta(\text{CH}_2 \text{ \& \; CH}_3) = 1454 \text{ cm}^{-1}$, $\delta(\text{CH}_3) = 1375 \text{ cm}^{-1}$) and also carbonyl ($\nu(\text{C}=\text{O}) = 1734 \text{ cm}^{-1}$) could be identified. After the deposition of the 4-MBN SAM (red curve) the vibrational bands of the contaminations are considerably reduced to a value just above the noise level and characteristic vibrational bands of 4-MBN can be identified.

In order to evaluate the removal of the contaminations the area under the curve of the stretching vibrations of the hydrocarbons was determined (comp. Table 4-1). The vibrations of $\nu_{\text{as}}(\text{CH}_2)$ and $\nu_{\text{s}}(\text{CH}_3)$ were not separable in the spectrum but are analyzed as one band centered around 2918 cm^{-1} .

	Before	After	Ratio
$\nu_{\text{as}}(\text{CH}_3)$	10.93×10^{-3}	0.44×10^{-3} (below noise level)	0.04
$\nu_{\text{s}}(\text{CH}_3) + \nu_{\text{as}}(\text{CH}_2)$	152.64×10^{-3}	11.16×10^{-3}	0.07
$\nu_{\text{s}}(\text{CH}_2)$	44.19×10^{-3}	5.21×10^{-3}	0.12

Table 4-1: Integrated area of vibrational bands of the contamination before and after deposition of the 4-MBN SAM.

Under the assumption, that the integrated area of the vibrational band scales linearly with the number of molecules on the surface the analysis shows, that the contaminations were reduced to less than 10 % for the CH_3 and to 12 % for the CH_2 contaminations compared to the initial values by the deposition of a 4-MBN SAM.

In the second exemplary SAM of GSH the GSH contains four $-\text{CH}_2-$ groups and is expected to form less dense monolayers than 4-MBN (surface density $\Gamma_{\text{GSH}} \approx 1.3 \times 10^{-10} \text{ mol/cm}^2$)²⁰¹.

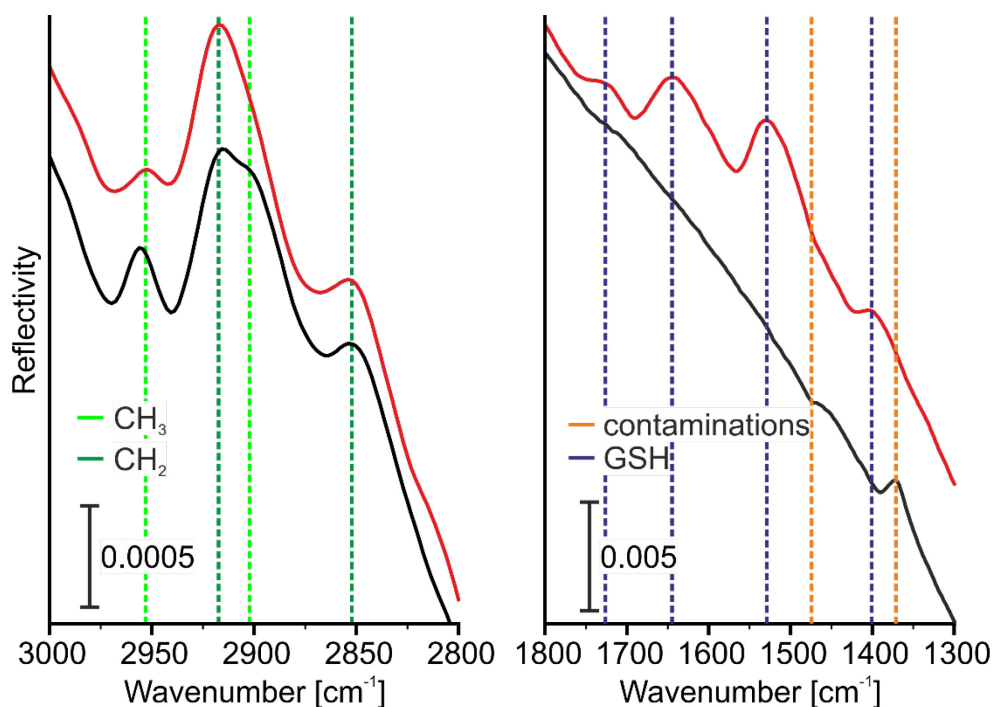


Figure 4-14: Formation of GSH SAM on a contaminated gold island film substrate. SEIRA spectra of the enhancement substrate before (—) and after (—) deposition of 4-MBN SAM from solution. Spectra were smoothed using a cubic spline interpolation.

In the IR reflectivity spectrum measured before the adsorption of GSH (Figure 4-14 black curve) similar contaminations as for the 4-MBN sample were identified. After the formation of a GSH SAM (Figure 4-14 red curve) the characteristic vibrational bands of GSH can be identified and a change in the amplitudes of the vibrational band in the stretching region of the hydrocarbons was observed.

The bands were analyzed with the same procedure as before and the results are summarized in Table 4-2.

	Before	After	Ratio
$\nu_{as}(\text{CH}_3)$	4.15×10^{-3}	1.03×10^{-3}	0.25
$\nu_s(\text{CH}_3) + \nu_{as}(\text{CH}_2)$	35.22×10^{-3}	32.51×10^{-3}	0.92
$\nu_s(\text{CH}_2)$	5.46×10^{-3}	7.04×10^{-3}	1.29

Table 4-2: Integrated area of vibrational bands of the contamination before and after deposition of the GSH monolayer on gold island film substrate

Under the same assumptions as above the analysis of the integrated areas of the vibrational bands showed that the amount of CH_3 is reduced to 25 % of its initial value while the amount of CH_2 is increased by the formation of a GSH monolayer. The increase in the amount of CH_2 is expected as the GSH itself contains CH_2 groups. This analysis has however be evaluated with great care as the different configurations of the $-\text{CH}_2$ groups and the coupled oscillations may lead to contributions which overlap with the vibrations attributed here to the $-\text{CH}_3$ groups of the contamination.

In comparison the removal of the contaminations was less efficient by the deposition of GSH compared to 4-MBN. Several explanation can be assumed for this observation. An important factor may be the different surface density of the two monolayers $\Gamma_{\text{GSH}} / \Gamma_{4\text{-MBN}} \approx 0.25$ which leads to a less densely packed SAM which in turn leaves more space for the contaminations on the surface. In addition the

morphologies of the island films may have been different, leading to different effective surface areas which furthermore influences the evaluation. The composition of the contaminations on the two investigated samples is different. The ratio of $\nu_s(\text{CH}_2) / \nu_{as}(\text{CH}_3)$ before the deposition of the SAM of the two samples was MBN-sample 1.31 and GSH sample 4.04 respectively which may lead to different desorption rates for the contaminations. These different ratios also show that the contaminations are not reproducible and should always be considered when vibrational bands which overlap with the bands of the contaminations are analyzed.

In summary the formation of a SAM on the surface of a gold island film from thiolate molecules is not hindered by the presence of contaminations of hydrocarbons. The deposition of a SAM rather leads to a reduction of the contaminations present on the surface of the gold island film. The amount of contaminations which is desorbed seems to scale with the packing density of the SAM as the more densely packed SAM of 4-MBN removes 6.25 fold more of the contaminations from the surface than the GSH monolayer. The results presented may be of high importance for the analysis of molecules with vibrational bands overlapping with the vibrational bands of the contaminations as *e.g.* lipids.

4.1.4. Plasmonic resonance shift by monolayer adsorption

The deposition of an organic monolayer onto gold island film changes the dielectric environment of the gold islands. In response to this change in the dielectric environment the resonance of the gold island film substrate is expected to be shifted (comp. section 2.4.4). This effect which forms the basis of LSPR sensing has recently been investigated by Rai et al.²⁰², for gold island film samples. The application of gradient island films however enables for a more in depth analysis as various gold island film structures are present on such a substrate which have experienced identical pretreatment and functionalization conditions. The shift of the resonance may be of interest for applications and should be considered in the IR as a baseline shift may result. For application of the enhancement substrates for combinatorial SERS and SEIRA the position of the resonance maximum may be of great importance to meet the resonance condition in SERS. Furthermore it may be of interest to employ LSPR sensing as a further source of information which can be obtained from the same substrate.

The shift in the plasmonic resonance in response to the formation of a SAM has been investigated for three model SAMs of 4-Mercaptobenzoic acid (4-MBA) (MW: 154.16 g/mol), 4-MBN (MW: 135.18 g/mol) and glutathione (GSH) (MW: 307.32 g/mol) prepared on gradient gold island film substrates. The substrates have been characterized by mapping UV-Vis ellipsometry and IR microscopy before and after functionalization. The pseudo-dielectric function was determined from ellipsometric UV-Vis measurements under an incidence angle of 70° using the formula presented in section 2.4.2.

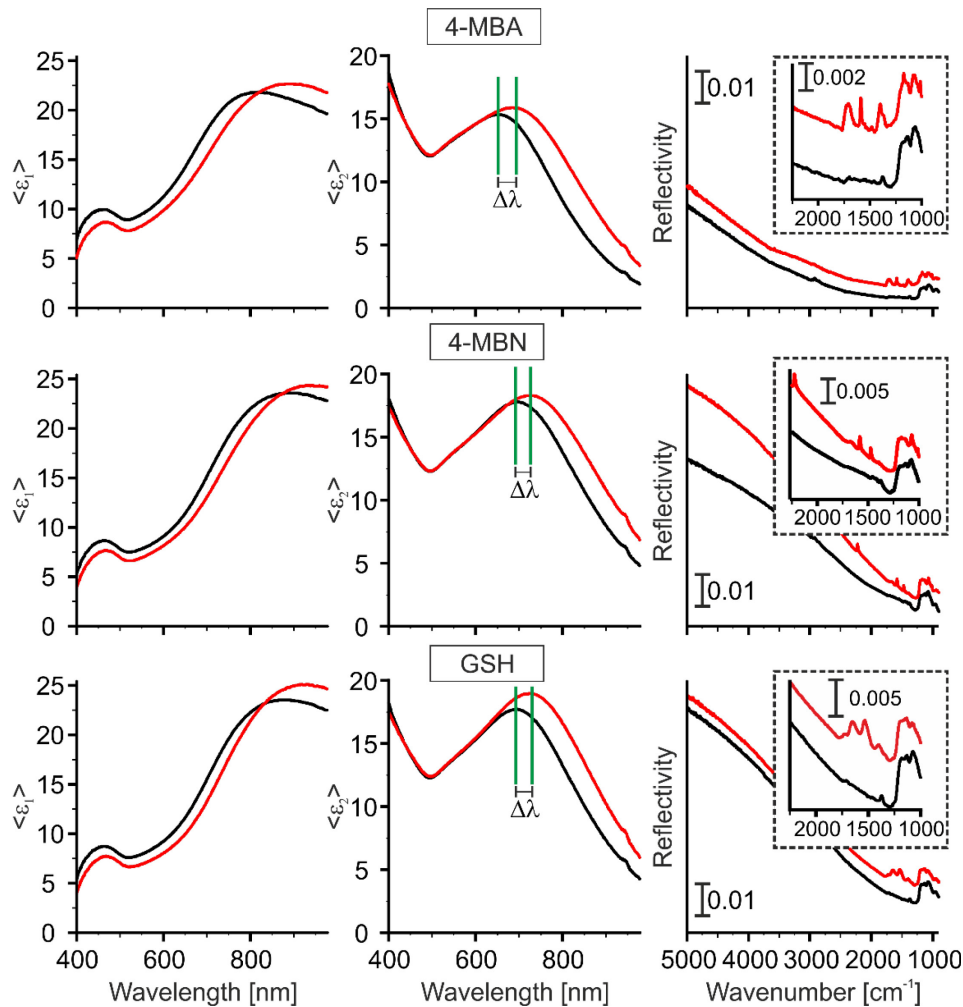


Figure 4-15: Shift of the resonance of gold island films upon absorption of different SAMs. (—) Measurement before SAM deposition (—) measurement after SAM deposition. (left column) real part $\langle \epsilon_1 \rangle$ of pseudo-dielectric function; (middle column) imaginary part $\langle \epsilon_2 \rangle$ of pseudo-dielectric function; (right column) corresponding IR reflectivity spectra.

The formation on the SAMs, in all three cases, leads to a considerable red-shift $\Delta\lambda$ in the resonance observed in the imaginary part of the dielectric function (Figure 4-15 middle column). The observed red-shift in the UV-Vis spectrum in turn leads to an upwards shift and in a change in the curvature of the reflectivity in the corresponding IR spectrum (Figure 4-15 right column).

In order to analyze the dependence of the shift in the resonance $\Delta\lambda$ on the initial central wavelength λ_0 , the data of the imaginary part of the pseudo-dielectric function obtained by a line scan along the gradient was analyzed. The initial central wavelength herein was used as a measure for the initial island film morphology. λ_0 before and λ_1 after functionalization were determined by fitting of a Gaussian function to the observed resonance. As observed in section 4.1.1 the central wavelength increased with increasing film thickness of the gold layer along the gradient island film. The limited spectral range of the employed ellipsometer (350–980 nm) and the effect of the broadening of the plasmonic resonance only permitted for the investigation of the resonances with a $\lambda_0 < 800$ nm.

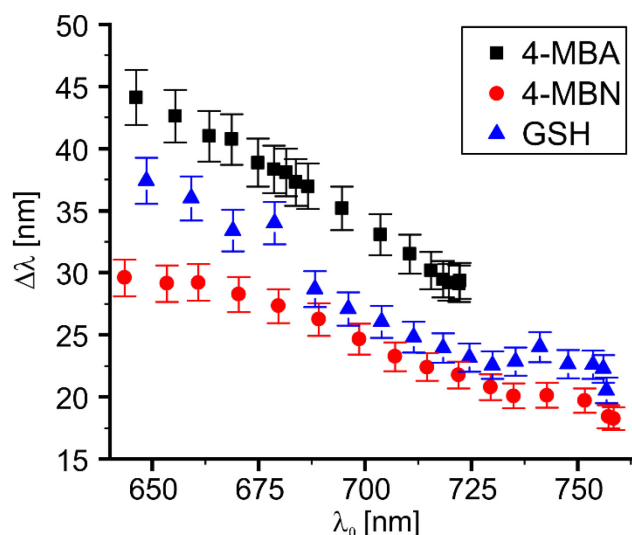


Figure 4-16: $\Delta\lambda$ in dependence of the initially observed resonance wavelength λ_0 for the three investigated SAMs. Dashed lines correspond to linear fit of the data

The analysis showed that the shift $\Delta\lambda$ is largest for resonances at low wavelength where the island films are composed of small individual particles and decreases with increasing wavelength of the initial resonance as the islands grow in size. A linear trend can be observed for this dependency in the region between 640 nm to 720 nm for the 4-MBA and 640 nm to 730 nm for the 4-MBN and the GSH SAM. Above 730 nm the shift in the resonance reaches a constant level for the 4-MBN and the GSH SAM.

The experiment showed that the shift in the resonance wavelength is dependent on the island film morphology. The shift appears to scale with $(n \cdot d)$ under the simplifying assumption that the refractive index scales with the density of the molecules in the SAM and the molecular weight. This observation opens up a further source of information as in addition to the information from the infrared spectra also LSPR sensing may be feasible on the gold island film substrates. The behavior of the curve as well as the dependence of the wavelength shift on the initial central wavelength λ_0 and hence the morphology of the island film may hold further information but will require further analysis which was outside the scope of this thesis.

4.1.5. Optical modeling of *ex situ* SEIRA reflectivity spectra

The optical modeling of SEIRA reflectivity spectra is of high interest in order to enable for quantitative analysis of the measurements and more detailed studies of the underlying processes as *e.g.* molecular interactions. Along the gradient metal island film substrates different island film morphologies with different fill-factors and dimensions of the individual islands can be found. The possibility to simulate these different island film morphologies with the presented EMA model (see section 2.4.4) has been investigated.

In order to perform the simulations the EMA model for the metal island film and the optical model for a uniaxial film have been implemented in Matlab. The implementation in principle allows for a fitting of all the parameters of the optical model. In the actual simulation however it is highly advised to fix as many parameters as possible using other corresponding techniques for the independent determination. As figure of merit the mean square error (MSE) was used for the fitting procedure. The actual values of the MSE have to be viewed with great care as the wavenumber range of the fit greatly influences these values. In consequence they are only comparable if the wavenumber range is chosen the same for the compared fits.

Simulation of SEIRA reflectivity spectra

In the simulation various parameter can potentially be determined. In order to gain a starting point for the simulation the dielectric function of the organic layer is best determined *a priori e.g.* using IR and UV-Vis ellipsometry. For this purpose a SAM of 4-MBN was prepared on a flat gold surface (glass/gold ($d=200$ nm)). A thickness of $d_{\text{MBN}} = 0.9$ nm was determined by UV-Vis ellipsometry assuming $n_{\infty} = 1.41$ for the SAM, this is a typical value obtained for a similar molecule of nitrobenzene.³⁷ IR ellipsometry was performed by Ilona Engler and used to obtain a $\tan \Psi$ spectrum of the SAM under an angle of incidence of 65° . The $\tan \Psi$ spectrum was modeled in SpectraRay3 (Sentech Instruments GmbH) using the parameters derived above in a layer model of gold/4-MBN SAM. For gold the optical constants of Rakic *et al.*¹⁵⁴ have been used in this model. The 4-MBN SAM was represented by a harmonic oscillator model and oscillator parameters were deduced by MSE fit to the measured spectrum. The oscillator parameters are summarized in Table 4-3 and the results of the simulation are shown in Figure 4-17 (a).

	ν_o [cm^{-1}]	F [cm^{-2}]	Γ [cm^{-1}]
$\nu(\text{C}\equiv\text{N})$	2228 ± 1	614 ± 1	11 ± 1
$\nu(\text{ring})$	1583 ± 1	445 ± 1	10 ± 1
$\nu+\delta(\text{ring})$	1476 ± 1	640 ± 1	7 ± 1

Table 4-3: Oscillator parameters of harmonic oscillator model representing the averaged properties of a 4-MBN SAM on gold. The parameters were determined by optical modeling of IR ellipsometry data using SpectraRay3 (Sentech Instruments GmbH)

The obtained oscillator parameters served as input values for the adsorbate layer on the gold islands in the simulation of an IR reflectivity spectrum of a 4-MBN film on a gold island film with optimized enhancement. In the fit equatorial diameter a and polar diameter c of the gold islands along with the fill factor f (see section 2.4.4) were determined by a MSE fit.

The MSE was defined as:

$$MSE = \frac{\sum_{i=1}^N (R_{meas}(\nu_i) - R_{simu}(\nu_i))^2}{N} \quad (4-1)$$

where N is the number of measurement points considered in the fit.

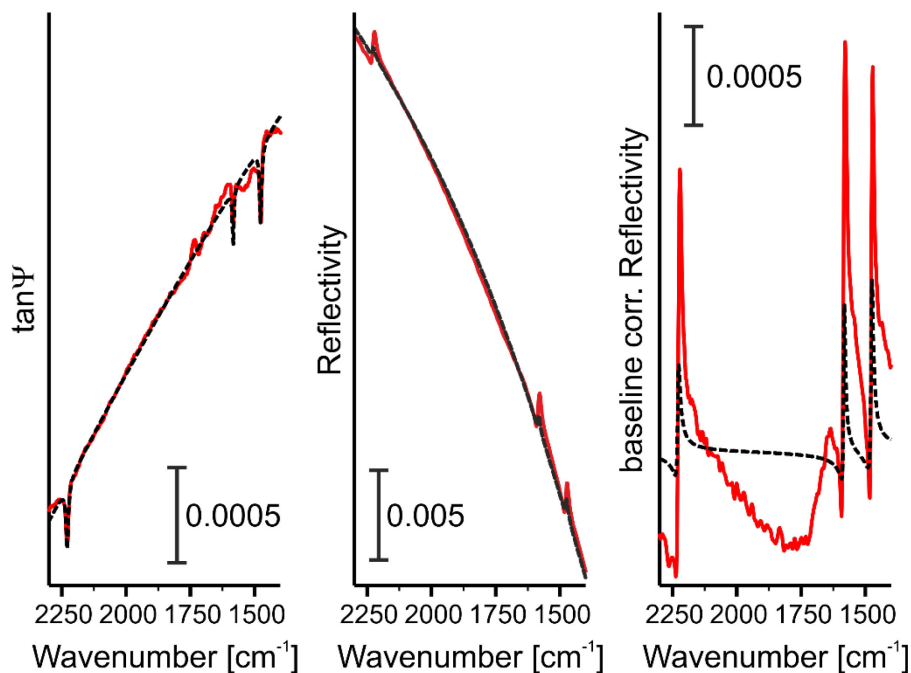


Figure 4-17: Simulation of SEIRA spectra using EMA model. (a) Fit of ellipsometric measurement of 4-MBN SAM on gold ($d_{\text{gold}} = 200 \text{ nm}$). The ellipsometric measurement was performed at 65° incidence angle. (b) Measured and simulated IR reflectivity spectra of 4-MBN SAM on gold island film substrate. (c) Measured and simulated IR reflectivity spectra of 4-MBN SAM baseline corrected using simulation of gold island film substrate without oscillators as baseline.

Figure 4-17 (b) shows the result of the simulation for $a = 17.65 \text{ nm}$, $b = 8.61 \text{ nm}$ and $f = 0.215$ resulting in an $\text{MSE} < 5 \cdot 10^{-7}$. The simulated spectrum shows a good agreement with the measured spectrum concerning the curvature of the spectrum. In Figure 4-17 (c) a simulation of the gold island film without the harmonic oscillators was used to perform a baseline correction. This presents a possibility to perform a baseline correction based on a physical model and allows for a better identification of the vibrational bands in the spectrum.

It has to be noted that the amplitude of the vibrations in the simulated spectrum are weaker by a factor of approx. 3 than the ones observed in the measured spectra. This deviation may result from the fact that the effective medium model cannot account for local field enhancement which may explain the additional enhancement.

Simulation of gold island films with different morphologies

As mentioned before the presented gradient gold island films realize different island film morphologies. In the following the ability of the optical model to account for these different morphologies has been investigated comparing measured and simulated spectra.

For the measurements a gradient gold island film has been deposited on a silicon substrate with a native oxide layer and was modified by a monolayer of GSH. The gradient was characterized with mapping IR microscopy with a step size of 1 mm.

The simulation was performed assuming a thickness of the GSH layer of 1.2 nm^{201} and $n_\infty = 1.5$ which has been confirmed by UV-Vis ellipsometry. The region between $3000 \text{ cm}^{-1} - 2800 \text{ cm}^{-1}$ has been modeled with the following oscillators (Table 4-4). The parameters were obtained from a best fit to measurement data of measurement #2.

	$\tilde{\nu}_0 [\text{cm}^{-1}]$	$F[\text{cm}^{-2}]$	$\Gamma [\text{cm}^{-1}]$
1	2854±1	6600±100	28±1
2	2897±1	3200±100	32±1
3	2924±1	11200±100	28±1
4	2957±1	3300±100	28±1

Table 4-4: Parameters of oscillators in the region between $3000 \text{ cm}^{-1} - 2800 \text{ cm}^{-1}$. Values were determined by a best fit to the measurement data of measurement #2 (see Figure 4-18).

It has to be noted that the vibrational bands of the GSH monolayer may be overlapping with contributions from contaminations of the surface by “advantageous hydrocarbons” (comp. section 4.1.3). The simulated spectra were obtained by adjusting the free parameters of the EMA model (length of minor and major axis and fill factor) for a best fit of the measured spectra.

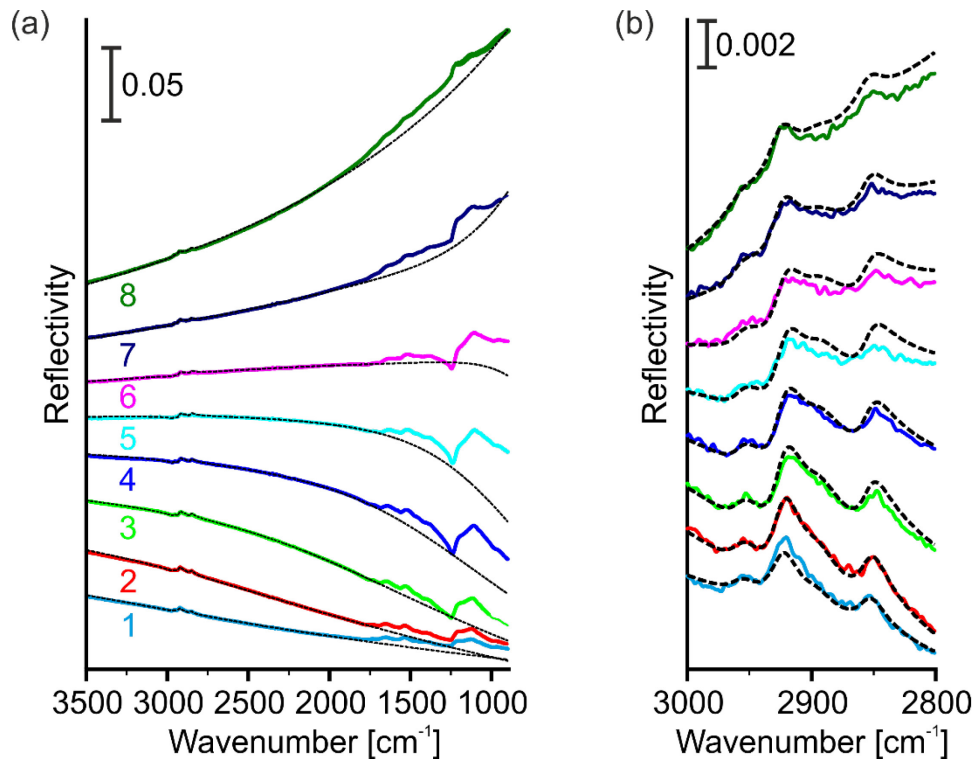


Figure 4-18: Simulation of IR reflectivity spectra of different island film morphologies. (a) Measured (full lines) and simulated (dashed lines) IR reflectivity spectra measured at different positions on a GSH modified gradient gold island film substrate. (b) Zoom into region of CH_x stretching vibrations.

Figure 4-18 shows the measured and corresponding simulated spectra at different positions along the gradient gold island film. The values of the EMA used for the simulation of the different spectra are summarized in Table 4-5 the error of the fit values is given by the step-size used in the fitting process.

Measurement #	Major axis [nm]	Minor axis [nm]	Fill factor	MSE (x10 ⁻⁷) (3500—1900 cm ⁻¹)	MSE (x10 ⁻⁷) (3000—2800 cm ⁻¹)
1	13.9±0.1	9.8±0.1	0.171±0.001	0.84	0.43
2	15.8±0.1	9.8±0.1	0.199±0.001	2.23	0.17
4	16.1±0.1	9.8±0.1	0.225±0.001	0.77	0.83
5	16.9±0.1	9.8±0.1	0.243±0.001	2.37	0.51
6	17.0±0.1	9.8±0.1	0.266±0.001	2.48	2.53
7	18.9±0.1	9.8±0.1	0.283±0.001	1.02	2.19
8	34.5±0.1	10.9±0.1	0.295±0.001	2.05	0.96

Table 4-5: Resulting EMA parameters of the optical simulation of different morphologies of gold islands films on a single gradient substrate.

Results & Discussion

The study of the simulations showed that different island film geometries along the gradient gold island film substrate can be modeled with a good agreement. Also above the percolation threshold (measurements #7 and #8) the simulation provides a good fit to the measurement data. The study also shows that enhancement and band-shapes of the vibrational bands observed in the spectral region between 3000 cm^{-1} and 2800 cm^{-1} can be reasonably reproduced when the oscillator parameters are determined by an initial fitting to a SEIRA spectrum. This is in contrast to the simulation using the optical constants of a SAM determined by IR ellipsometry on a thick gold film shown previously which could not reproduce the enhancement. It may be an indication that the optical constants derived by IR ellipsometry may not directly be applicable for the simulation of SEIRA spectra. The reasons for this deviation have to be investigated in future studies.

In summary the implemented optical model can in principle be used to simulate the experimental *ex situ* SEIRA microscopy spectra. It can be used to provide a method for baseline removal to remove the effect of the gold island film on the spectrum and to allow for a more detailed study of the vibrational bands of the molecule of interest. The model can however not reproduce the observed enhancement when optical constants determined by modeling of IR ellipsometry spectra are used as input values for the oscillator model. The band-shape and enhancement can however be reproduced for different island film geometries if the parameters of the oscillator model representing the organic layer are determined by an initial fit to a SEIRA spectrum. This observation should in the future be further investigated to allow for an improved optical modeling of SEIRA spectra.

4.2. *In situ* IR microscopy in microfluidic volumes

The development of an optofluidic platform for *in situ* IR and SEIRA spectroscopy on microfluidic volumes enables to perform different *in situ* studies which are presented in the following.

4.2.1. Online *in situ* reaction monitoring

A potential application of the optofluidic platform could be online on-chip monitoring of chemical reactions in solution. With the aim of demonstrating the feasibility of *in situ* monitoring of chemical reactions with the optofluidic platform, the reaction of ethyl acetate hydrolysis was studied. The reaction has been studied in a mixture of ethyl acetate and an aqueous solution of sodium hydroxide (0.1 mM). For the experiment a blank silicon substrate as IR-window and a microfluidic chip of type II (comp. section 2.6) have been utilized.

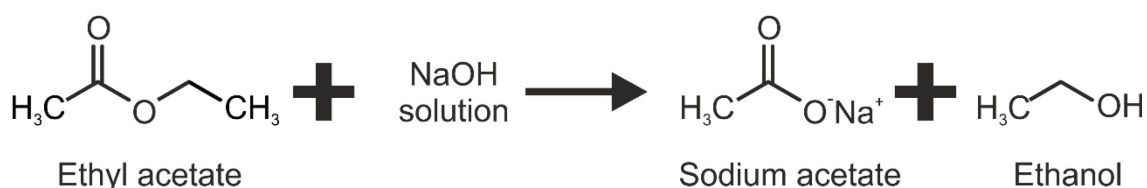


Figure 4-19: Schematic of the ethyl acetate hydrolysis reaction

In the presence of hydroxide ions, ethyl acetate is hydrolyzed forming sodium acetate and ethanol (Figure 4-19).²⁰³ This reaction has been chosen as an example because ethyl acetate provides distinct vibrational bands ($\nu(\text{C}=\text{O})$ around 1750 cm^{-1} and a vibrational band mainly resulting from $\delta(\text{H}_3\text{C}-\text{C}=\text{O})$ vibrations around 1380 cm^{-1}). These bands only show a weak overlap with the vibrational bands of water and the educts of the reaction.²⁰⁴

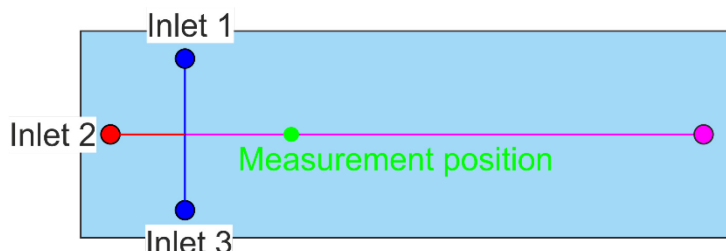


Figure 4-20: Schematic of employed microfluidic chip. Inlet 1 (0.1 ml/h) and 3 (0.1 ml/h) were used for the delivery of sodium hydroxide solution and ethyl acetate was supplied via Inlet 2 (0.2 ml/h). The measurement position was chosen approx. 1 cm after the T-junction to ensure for sufficient mixing.

The T-junction of the microfluidic chip of type II has been used to obtain a mixture of ethyl acetate and sodium hydroxide solution. Measurements were performed approx. 1 cm after the junction to ensure for an appropriate mixing of the reactants. The reaction was monitored by stopping the flow and recording consecutive spectra for 25 min at the indicated measurement position (32 scans, 2 cm^{-1} resolution, $t_{\text{meas}} = 9\text{ s}$).

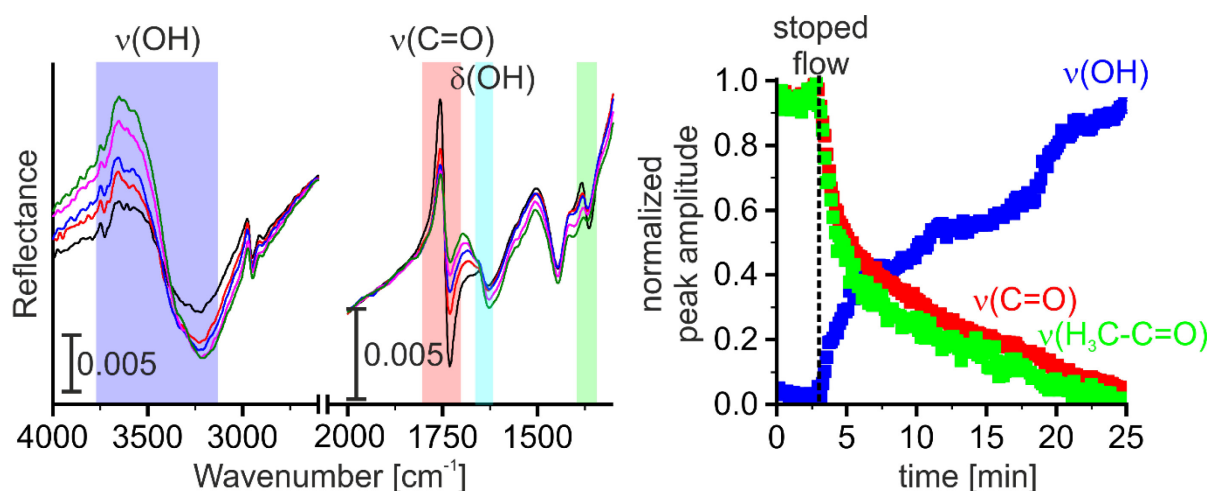


Figure 4-21: *In situ* monitoring of ethyl acetate hydrolysis. (a) Exemplary IR reflectivity spectra recorded during the experiment at the start (black line), the end (green line) and at 3 time points in between (red, blue and pink lines). The vibrational bands monitored for the analysis are indicated. (b) Time dependent development of the peak amplitude of the v(OH) (blue), v(C=O) (red) and v(H₃C-C=O) (green) vibrational bands.

The vibrational bands of the ethyl acetate as well as the bands of the OH stretching and deformation vibrations can be clearly identified in the spectra at the beginning of the experiment (Figure 4-21 (a)). After the flow is stopped the intensity of the vibrational bands associated with the ethyl acetate decreases and the intensity of the OH vibrations which may be associated with the formation of ethanol increases. For the two vibrational bands of the ethyl acetate the decrease follows an exponential trend (Figure 4-21 (right)). The increase in the intensity of the OH stretching vibration associated with an increase in ethanol concentration follows a reverse trend. After 20 min however a deviation from the exponential trend can be observed in the amplitude of the OH vibration where no equivalent is found in the amplitudes of the ethyl acetate vibrational bands. The origin of this change has not been investigated further at this point. However, a possible explanation might be changes in the hydrogen bonding with increasing ethanol content in the solution which influences the vibrational signature of the OH vibration. This effect has been known to complicate the evaluation of the OH vibrational modes of alcohols in aqueous environments.²⁰⁴

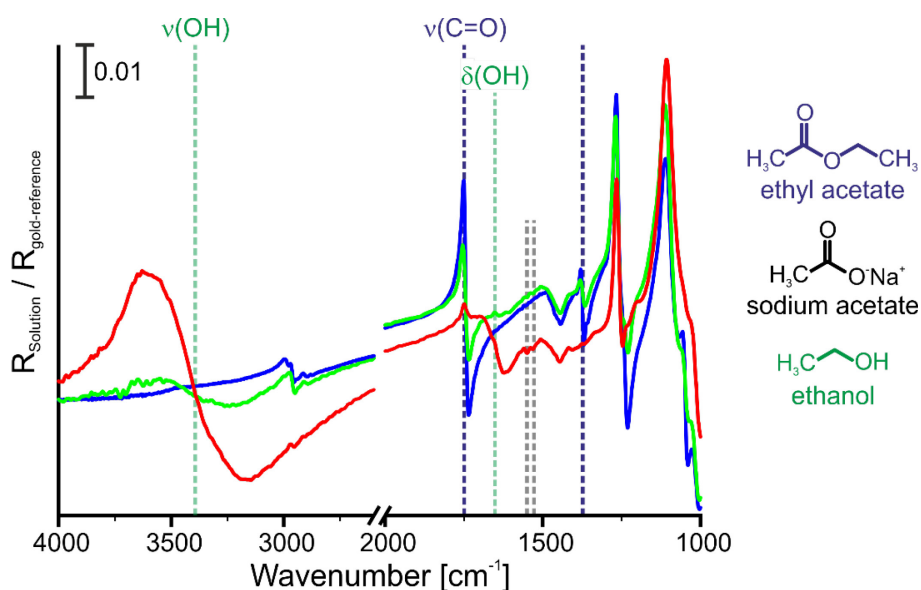


Figure 4-22: *In situ* IR spectra recorded on the microfluidic chip of pure ethyl (blue), the mixture after the flow was stopped (green) and at the end of the measurement (red). Respective vibrational bands of ethyl acetate and the educts of the reaction are indicated color-coded in the spectra.

Results & Discussion

Figure 4-22 shows IR spectra obtained on the microfluidic chip at the same position for pure ethyl acetate (blue), the mixture at the beginning (red) and at the end of the measurement (green). For the analysis a linear relationship between the area of the $\nu(\text{C}=\text{O})$ vibrational band and the number of ethyl acetate molecules present in the solution is assumed. Under this assumption the initial concentration of ethyl acetate after stopping the flow is approx. 38 vol. % and decreases to approx. 5 vol % at the end of the experiment. Under consideration of the noise level in the measurement a theoretical limit of 0.6 vol. % can be estimated for ethyl acetate under the given conditions in the experiment.

The performed experiment shows that, in principle, chemical reaction can be monitored and their kinetics can be investigated in a label-free analysis under *in situ* conditions with the presented optofluidic platform. This ability could be of interest to *e.g.* monitor on-chip synthesis in *e.g.* micro-reactors or to investigate mixing processes. In addition this could be also of interest to study reactions involving multiple reactions in multiple compartments on a microfluidic chip and could be performed cost-effectively on polymeric microfluidic chips. In addition such experiments could be performed utilizing enhancement substrates to increase sensitivity.

4.2.2. *In situ* monitoring of monolayer assembly with SEIRA spectroscopy

The *in situ* monitoring of monolayer self-assembly at the solid-liquid interface and investigations of formation kinetics are of high interest in many applications. SAMs are commonly used for the modification of the interface *e.g.* to modify interfacial properties as hydrophobicity or to obtain functional surfaces for sensing applications.¹⁵⁷ Sub-monolayer sensitivity with measurement times at least on the order of minutes is required in order to determine the kinetics of the formation, in consequence the process of SAM formation presents a possibility to demonstrate the high sensitivity of the presented method. The formation of two model SAMs formed from the previously studied molecule 4-MBN as well as from GSH have been investigated along with the technologically relevant recognition of streptavidin by a biotinylated surface.

Formation of 4-mercaptobenzonitrile SAM

The formation of a self-assembled monolayer of the small aromatic molecule 4-MBN was investigated under *in situ* condition. The experiment was performed with a microfluidic chip of type I (see Figure 2-25). In the experiment a gradient gold island film on silicon (74 mm x 20 mm x 0.8 mm, MateK GmbH) was used as enhancement substrate. Optimized enhancement performance of the substrate was ensured, evaluating the enhancement of the silicon oxide *ex situ* prior to the experiment (comp. section 4.1.1). Measurements were performed at the position of maximum enhancement determined in the *ex situ* experiment. An initial spectrum was recorded, where the channel was filled with pure ethanol. In order to enable sensitive monitoring of the changes at the solid—liquid interface the ratio of the measured spectrum and the initial spectrum were evaluated. In the experiment a 1 mM solution of 4-MBN in ethanol was pumped through the microfluidic channel at a continuous volume flow rate of 0.2 ml/h. IR-reflectivity spectra with a resolution of 1 cm⁻¹ were recorded consecutively for more than 6 h adding up 32 Scans per measurement ($t_{\text{meas}}=9$ s). Averaging over 20 measurements resulted in a time resolution of 3 min in the evaluation of the experiment and a sufficient signal-to-noise ratio. It has to be noted that the chosen resolution of 1 cm⁻¹ is very high. This resolution was chosen to demonstrate that also high resolution measurements are feasible. A lower resolution of 4 cm⁻¹ or 8 cm⁻¹ is often sufficient in the experiment and results in a better signal-to-noise ratio and may provide an increased temporal resolution.

Concerning the formation of the SAM the peak amplitudes of the stretching vibration ν (ring) and the combined stretching and deformation vibration of the ring $\nu+\delta$ (ring) were evaluated by fitting of a Gaussian function to the vibrational bands. The noise-level was defined by the 3σ criterion analyzing the noise in the vicinity of the bands.

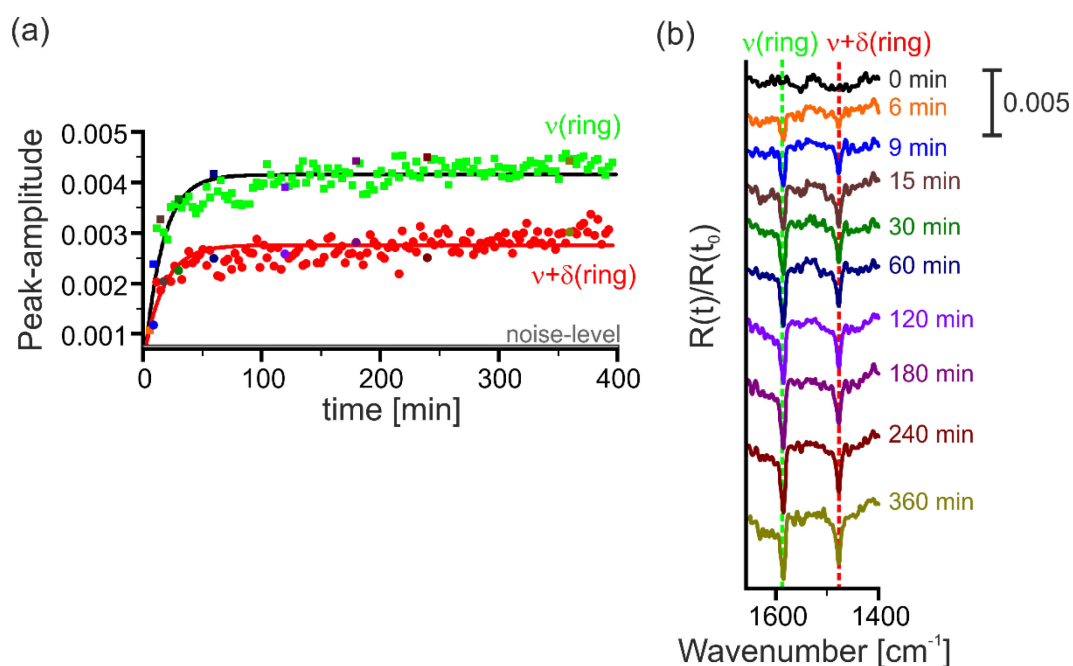


Figure 4-23: *In situ* monitoring of 4-MBN SAM formation from 1 mM solution of 4-MBN in ethanol. (a) Fitted peak-amplitude of the stretching $\nu(\text{ring})$ (■) and the combined stretching and deformation vibration $\nu+\delta(\text{ring})$ (●) of 4-MBN during monolayer formation. (b) Exemplary *in situ* IR spectra corresponding to marked points in (a). Spectra are shifted for better comparison.

Figure 4-23 (a) shows the time dependent fitted amplitudes of the two ring vibrations. Highlighted points in the graph correspond to the exemplary spectra in Figure 4-23 (b). After six minutes exposure of the gold island film to the solution characteristic vibrational bands of the 4-MBN can be identified in the spectrum. During the formation of the SAM the amplitude of the vibrational bands increases as more and more molecules are adsorbed on the surface. Completion of the SAM formation is obtained when no changes in the amplitude of the vibrational bands can be observed. Time dependent monitoring of the amplitude of these vibrational bands enables one to follow the formation process of the SAM *in situ* and to determine binding kinetics. Furthermore if a different behavior is observed for vibrational bands with different effective orientations of the dipole-moment with respect to the molecule (*e.g.* in-plane and out-of-plane orientation of the dipole-moment) this may be indicative for rearrangement processes within the SAM.^{38, 39} In the formation of the 4-MBN SAM no such differences could be observed as only vibrational modes with dipole-moments with the same orientation with respect to the molecule were accessible in the measured wavenumber region.

The development of the analyzed peak amplitude of the 4-MBN over time shows a good qualitative agreement with a first order Langmuir-type adsorption model (see section 2.4.4). Assuming no desorption of the molecule from the surface an averaged adsorption rate constant of (62 ± 6) L/(mol s) was determined from equation (2-25) for the two evaluated peaks.

The *in situ* monitoring of the SAM formation can further be used to give an estimate of the limit of detection for the molecule under investigation. In general this limit of detection will strongly depend on the vibrational properties of the molecule in particular on the strength of the dipole-moment of the investigated vibrational band.

As the surface density 4-MBN is unknown the surface density of benzene thiol was used, whose chemical structure shows a high similarity to 4-MBN. The surface density of a benzene thiol SAM on a gold island film is approx. 5.3×10^{-10} mol/ cm^2 .¹⁰⁹ Under the simplifying assumption of dilution of molecular groups in the surface layer contributing to the adsorption band, a linear correlation between

band amplitude and the number of molecules was assumed. The resulting limit of detection (LOD) defined by the noise-level corresponds to a surface density of $(1.0 \pm 0.5 \times 10^{-10})$ mol/cm², (13.5 ± 0.7) ng/cm² or less than 20% monolayer coverage. Taking into account the approx. measurement area of $(3 \pm 0.5 \times 10^{-4})$ cm² this corresponds to a limit of detection mass (LOD_M) of (4 ± 1) pg or (30 ± 16) fmol for 4-MBN.

The ability to measure the vibrational signature of the molecule prior to the complete formation of the SAM demonstrates that sub-monolayer sensitivity can be obtained with the integration of enhancement substrates in the optofluidic platform during *in situ* measurements. This possibility can in principle be used to study in addition to the adsorption kinetics *e.g.* orientation effects or interactions between the molecules during the formation of the monolayer and can increase the understanding of the processes involved in monolayer formation.

Monolayer formation of glutathione

The results presented in the following have been published in ACS Sensors: Kratz, C., Furchner, A., Oates, T. W., Janasek, D., & Hinrichs, K. (2018). Nanoliter Sensing for Infrared Bioanalytics. ACS sensors, 3(2), 299-303. DOI: 10.1021/acssensors.7b00902

As a second model molecule for the study of monolayer formation the tripeptide glutathione (GSH) was chosen. The molecule is the most abundant non-protein thiolate molecule in humans. It serves as a model for molecules with a cysteine residue which allow for surface immobilization on the gold island film surface. In contrast to 4-MBN, GSH is water soluble and is therefore also used as a model system in order to show that processes in aqueous environment can be investigated with the same sensitivity. In the experiment a 6 mM solution of GSH was pumped through the microfluidic channel (chip type I, comp. section 2.6) at a constant volume flow rate of 0.2 ml/h. Consecutive spectra were recorded over 6.5 h (3 min per measurement) under continuous flow. A spectrum recorded in DI-water prior to the experiment served as a reference in the experiment. The peak amplitude of the GSH's amide II band was evaluated. This band is the most prominent one in the vibrational spectrum of GSH; similar results for the adsorption kinetics can be obtained for all observable vibrational bands.

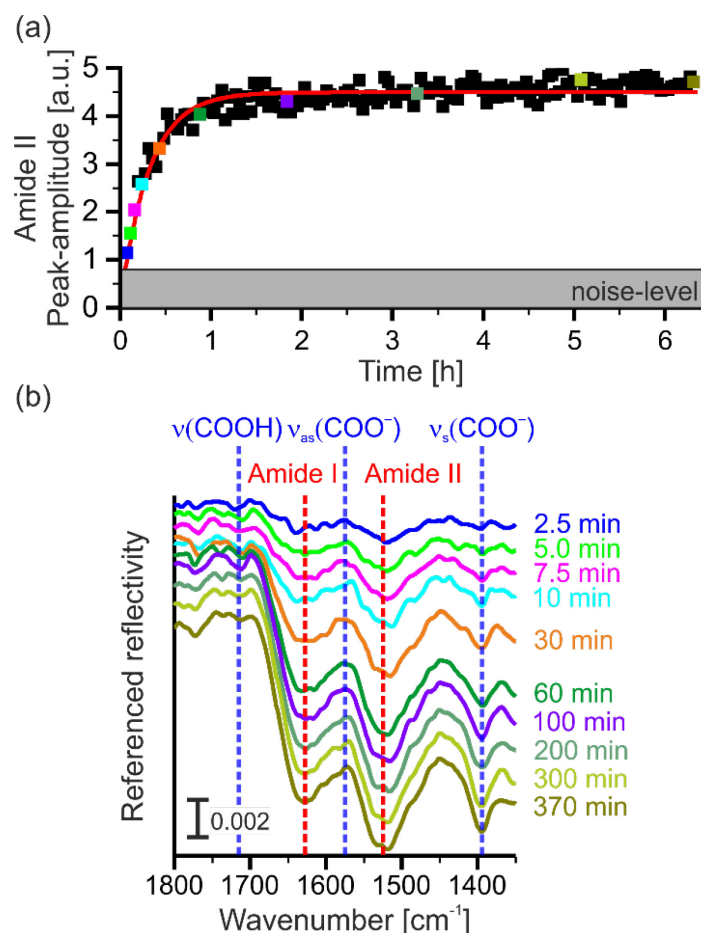


Figure 4-24: *In situ* IR monitoring of GSH monolayer formation in microfluidic flow cell. (a) Peak amplitude of amide II vibrational band during monolayer formation and fit of an exponential function corresponding to Langmuir-type adsorption (red line). (b) Exemplary *in situ* IR spectra corresponding to marked points in (a). Spectra are shifted for better comparison. Reprinted with permission from Ref. [87]

Figure 4-24 (a) shows the time dependent fitted amide II peak amplitude during monolayer formation, corresponding exemplary IR spectra are shown in Figure 4-24 (b). The adsorption of GSH on the surface is confirmed by the presence of distinct GSH vibrational bands.²⁰⁵⁻²⁰⁸ The clearly visible band of the symmetric stretching vibration of the dissociated carboxylic groups ($v_s(\text{COO}^-)$) indicates that the carboxylic groups of the GSH in the monolayer are partially dissociated under the environmental conditions present during monolayer formation.²⁰⁷ Most of the GSH adsorption occurs within the first hour of monolayer formation followed by a slow completion of the monolayer on the time scale of several hours.¹⁶⁶

The growth of the GSH monolayer shows good qualitative agreement with a first order Langmuir-type absorption model (comp. section 2.5.1). Fitting of a corresponding exponential function (equation (2-25)) yields an adsorption rate constant of $k_{ads} = (8.6 \pm 0.3) \text{ L} / (\text{mol s})$ for the formation of the GSH monolayer.

The LOD was determined in analogy to the method used for the 4-MBN SAM but taking into account the potentially increased surface area of the island film in comparison to a flat gold substrate where a surface density of $\Gamma_{\text{GSH}} = 1.2 \times 10^{-10} \text{ mol/cm}^2$ ²⁰¹ of the complete GSH monolayer has been reported. With typical dimensions of $a = 22 \text{ nm}$ and $c = 4 \text{ nm}$ (comp. chapter 2.4.4) of the presumably oblate spheroidal particles determined by AFM measurements, the surface area is increased by approx. 8%. In consequence an effective surface density of $\Gamma_{\text{GSH}} = 1.3 \times 10^{-10} \text{ mol/cm}^2$ has been assumed for the calculation. A signal which can still be evaluated by the given noise level relates to a surface density of

$(3.4 \pm 0.2) \times 10^{-11}$ mol/cm² or (10.5 ± 0.6) ng/cm² corresponding to approx. 25 % surface coverage. The limit of detection mass for GSH is (3 ± 1) pg corresponding to (10 ± 2) fmol.

The results of this second experiment support and underline the findings of the previous experiment. Measurements performed with the developed optofluidic platform using enhancement substrates provide sub-monolayer sensitivity for *in situ* studies of processes at the solid—liquid interface. This high sensitivity allows one to monitor the formation of and investigate process during the formation of monolayers. These type of studies are of high interest as monolayers are commonly used for surface functionalization of materials and their assembly and ordering plays a key role in the functionality of the obtained surfaces. The LOD obtained in both experiments was on the order of few ng/cm² and the LOD_m on the order of pg. The obtained high sensitivity is comparable to other label-free techniques used in sensing applications but in addition gives access to the vibrational information of the molecule. This additional information can be used for the identification as well as to perform further studies on the properties of the molecule adsorbed on the surface. In consequence the presented optofluidic platform may be an interesting candidate in the development of novel label-free (bio-) sensing applications.

4.2.3. *In situ* study of changes in the ionization state of glutathione dissociation in dependence on environmental pH

The results presented in this section have partially been published in ACS Sensors: Kratz, C., Furchner, A., Oates, T. W., Janasek, D., & Hinrichs, K. (2018). *Nanoliter Sensing for Infrared Bioanalytics*. ACS sensors, 3(2), 299-303. DOI: 10.1021/acssensors.7b00902

Another important aspect in the study of ultra-thin molecular films are their interactions with the experimental environment and response to external stimuli such as changes in pH, temperature or salt concentration. The possibility to study these type of effects is of great interest for investigations of *e.g.* molecular hydration, changes in protein confirmation, ligand-receptor binding and other interactions.

Monolayers of molecules containing carboxylic groups change their ionization state in response to the environmental pH.²⁰⁹ The surface ionization is of prime importance for protein binding or further surface modifications.

A monolayer of GSH was used to demonstrate the capability for *in situ* monitoring of changes in its ionization state. The monolayer was deposited from an aqueous solution (5 mM, pH 5). In order to monitor the changes in the spectra resulting from the changing environmental pH an initial spectrum of the monolayer was recorded in deionized water (pH5) after completion of the monolayer formation and rinsing. In the next step the deionized water was replaced by an alkaline solution (pH10) of sodium hydroxide (NaOH) in deionized water. Subsequently the alkaline solution was exchanged with an acidic solution (pH2) of hydrochloric acid (HCl) in deionized water.

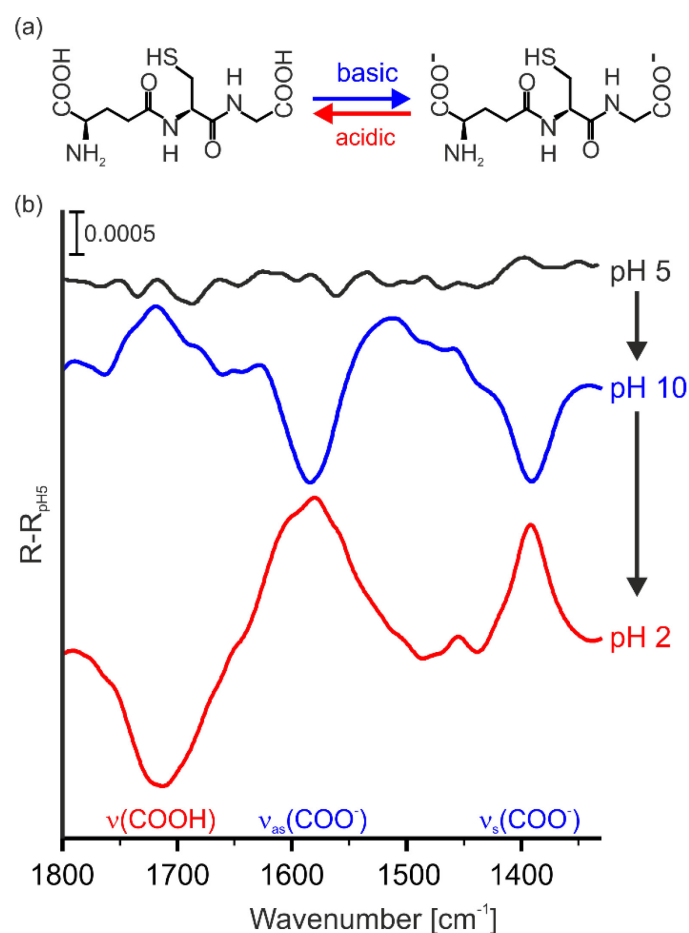


Figure 4-25: pH dependent dissociation and protonation of carboxylic groups of GSH monolayer. (a) Schematic of the reaction of carboxylic group in response to environmental pH changes. (b) *In situ* IR microscopy spectra at pH 5 (—), pH 10 (—) and pH 2 (—). All spectra are referenced to a spectrum at pH 5. Reprinted with permission from Ref. [87]

The reaction of GSH in dependence on the environmental acidity is schematically depicted in Figure 4-25 (a). The difference spectra in Figure 4-25 (b) show changes in the IR absorption spectrum of the monolayer after equilibration at the respective pH. In the difference spectra upward pointing bands indicate a decrease in absorption while downward pointing bands indicate an increase in absorption respectively. In the alkaline environment (

blue) an upward pointing band for the carboxylic group around 1725 cm^{-1} and two downward pointing bands of the asymmetric and symmetric stretching modes of the carboxylic ion around 1580 cm^{-1} and 1395 cm^{-1} were identified. The observed bands indicate that the alkaline solution led to a dissociation of carboxylic groups in the monolayer. The reversed trend was observed in the acidic environment, indicating a protonation of the carboxylic groups in the monolayer.

The difference bands are more pronounced in the acidic than in the alkaline environment. This indicates that a large fraction of the carboxylic groups in the GSH monolayer are dissociated even at the slightly acidic conditions of the growth solution (deionized water).

In agreement with Aureau *et al.*²⁰⁹ the presented study shows that the monolayer's surface equilibrium between carboxylic groups and the respective ion can be reversibly tuned by an adjustment of the environmental pH. The experiment illustrates that the ionization state of a monolayer and changes thereof can be assessed and monitored on the monolayer level.

In order to demonstrate that the observed changes can also be followed time dependently under *in situ* conditions, measurements were performed during the exchange of the alkaline to the acidic solution ($t_{\text{meas}} = 2.5$ min).

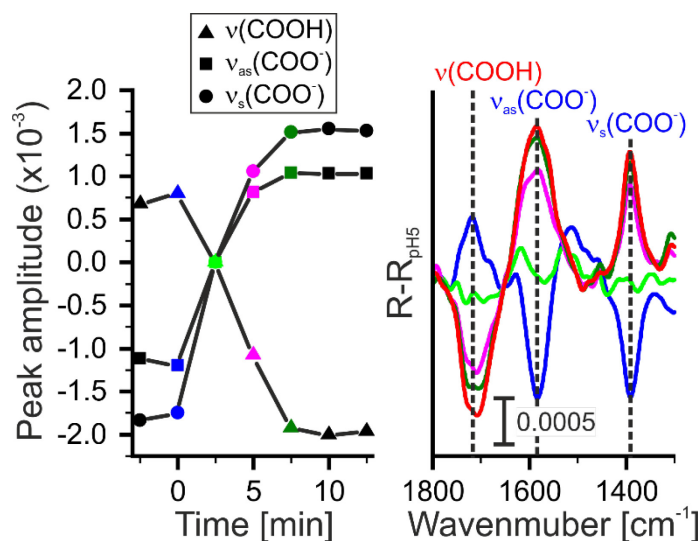


Figure 4-26: Time dependent measurement of protonation reaction of the carboxylic ions in the monolayer of GSH. (left) Time dependence of fitted peak amplitudes of the vibrational bands of the carboxylic group $\nu(\text{COOH})$ (▲), the asymmetric stretching vibration $\nu_{\text{as}}(\text{COO}^-)$ (●) and the symmetric stretching vibration $\nu_{\text{s}}(\text{COO}^-)$ (■) of the carboxylic ion. (Right) Differential IR microscopy spectra recorded during the protonation of the carboxylic ion, corresponding in color to the points marked in the left graph.

Figure 4-26 illustrates that kinetics of the protonation reaction can in principle be studied under *in situ* conditions. The fitted peak amplitudes of the vibrational bands associated with the carboxylic group and the respective ion show an exponential trend in time for the protonation of the carboxylic groups (Figure 4-26 (left)).

The presented results confirm that changes within monolayers can be studied time resolved with sub-monolayer sensitivity with the presented method. This may be of interest *e.g.* to elucidate effects of surface treatments or changes in environmental conditions as well as to investigate receptor-ligand interactions as small chemical changes can be monitored *in situ* with the presented optofluidic platform.

4.2.4. *In situ* study of surface immobilization of streptavidin on a biotinylated enhancement substrate

The results presented in this section have been published in ACS Sensors: Kratz, C., Furchner, A., Oates, T. W., Janasek, D., & Hinrichs, K. (2018). Nanoliter Sensing for Infrared Bioanalytics. ACS sensors, 3(2), 299-303. DOI: 10.1021/acssensors.7b00902

SAM's are often used as an initial surface functionalization for the further immobilization of other molecules as *e.g.* proteins or antibodies. An example often used in this route is the binding of streptavidin on a biotinylated surface.^{52, 210-212} The biotin-streptavidin couple is for example often used for the subsequent immobilization of a biotinylated antibody in biosensor concept.^{212, 213} In the following experiment the possibility to monitor the binding of streptavidin to a biotinylated surface has been investigated. The experiment also serves as an example that measurements containing information's on the secondary structure of a protein can be achieved with the presented concept.

A biotin SAM on an enhancement substrate was prepared using a biotin-SAM formation reagent kit according to the protocol provided by the supplier. An initial spectrum of the biotin monolayer in PBS buffer solution served as a reference to monitor the adsorption of streptavidin. A solution of streptavidin in the same PBS buffer with a concentration of $0.6 \mu\text{M}$ was prepared for the experiment and pumped through the channel for 6 hours at a constant volume flow-rate of 0.15 ml/h . *In situ* IR spectra were consecutively recorded (1024 Scans, $t_{\text{meas}}=5 \text{ min}$, 2 cm^{-1} resolution).

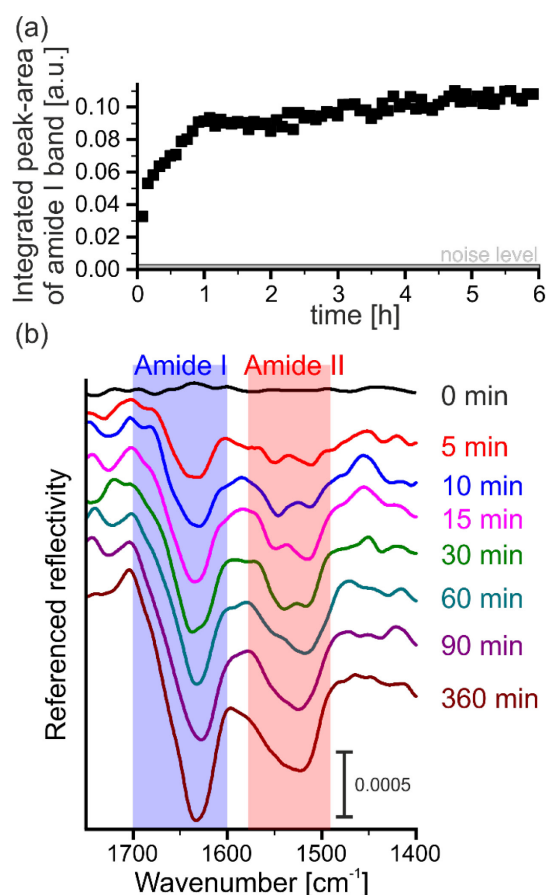


Figure 4-27: *In situ* IR monitoring of streptavidin adsorption on biotinylated surface with the optofluidic platform. (a) Time dependence of integrated peak area amide I vibrational band during adsorption (b) *In situ* IR spectra at exemplary time points during streptavidin adsorption. Spectra are shifted for better comparison and smoothed using a cubic spline interpolation. Reprinted with permission from Ref. [87]

The time dependence of the adsorption shown in Figure 4-27 (a) was monitored by integrating the peak area under the amide I band using Origin Pro. The same results can be obtained for the amide II band. Already in the first measurement after 5 min, a characteristic spectrum of streptavidin was obtained. The amide I vibrational band (around 1634 cm^{-1} with a shoulder around 1660 cm^{-1} and 1690 cm^{-1}) and the amide II vibration (two contributions around 1545 cm^{-1} and 1512 cm^{-1}) can be observed in the referenced spectra shown in Figure 4-27 (b). After 60 min the two contributions of the amide II band form a combined band with a central frequency around 1530 cm^{-1} . The observed vibrational modes of the streptavidin are in agreement with findings of Chabal *et al.*²¹⁰ and Heberle *et al.*⁵² for immobilization of streptavidin on a biotinylated substrate. After rinsing the same spectra are obtained, indicating the formation of a stable layer of streptavidin on the biotinylated gold island film.

With the integrated peak area of the amide I band of the completed monolayer adsorption as a reference a LOD for streptavidin can be calculated, following the procedures previously introduced (comp. section 4.2.2). Assuming a surface densities of streptavidin of $(3.85 \pm 0.15) \text{ pmol/cm}^2$ from literature²¹⁴ results in an effective surface density of $(4.16 \pm 0.16) \text{ pmol/cm}^2$, the noise level in

consequence corresponds to an estimated LOD of (0.12 ± 0.01) pmol/cm² or (7.1 ± 0.3) ng/cm² for streptavidin in an aqueous environment. Based on the detection area (comp. section 3.2) this corresponds to a LOD_M of (2.1 ± 0.4) pg or approx. 36 attomol of streptavidin.

The observed spectral signature of the amide I band is characteristic for the β -sheet secondary structure of streptavidin.^{52, 215} The two components of the amide II band and their changes, along with the changes in the amide I band during adsorption are indicative for structural changes of the streptavidin as a consequence of biotin binding.²¹¹ As the binding of the biotin is assumed to change the hydrogen bonding pattern within the β -barrel structure of the sub-units of the streptavidin the observed spectral signatures might potentially be used to elucidate this binding process.

In order to investigate structural changes in proteins utilizing analysis of the amide I band it has to be noted that the band is spectrally overlapping with the deformation vibration of water used as solvent in the experiment. In consequence of the changing conditions at the interface compared to the used reference the water band will result in a band with an opposite sign. Though not directly identifiable in the shown spectra the overlap between these two bands might alter the shape and amplitude of the amide I band. This effect can be resolved by proper optical modeling and will be necessary in cases where the structure of the protein is to be analyzed.

The experiment confirms high sensitivity for the investigation of binding processes on the order of few ng/cm² previously found for the formation of SAMs. It also shows that the amide I and amide II bands of a proteins can be measured as well as changes thereof. This will be of high interest in the future development of the technique as it may enable one to investigate the effect of external stimuli on the protein secondary structure and to monitor changes as a result of *e.g.* ligand binding.

4.3. Hybrid sensor substrates obtained by pairing pre-functionalized graphene with enhancement substrates

In the research of application of enhancement substrates in biosensing, surface functionalization of the enhancement substrate plays a key role to introduce target specificity.^{160, 216-218} Major obstacles may arise in the preparation of the surface functionalization as the enhancement properties of the enhancement substrate must be preserved during the functionalization process. This in consequence limits the applicable methods and types of chemicals which can be used. Furthermore the material of the metal island film itself may dictate the applicability of functionalization protocols and methods. An alternative route in the surface functionalization can be pursued by the transfer of pre-functionalized graphene to an enhancement substrate.

The general scheme of the formation of the novel hybrid sensing material is shown in Figure 4-28.

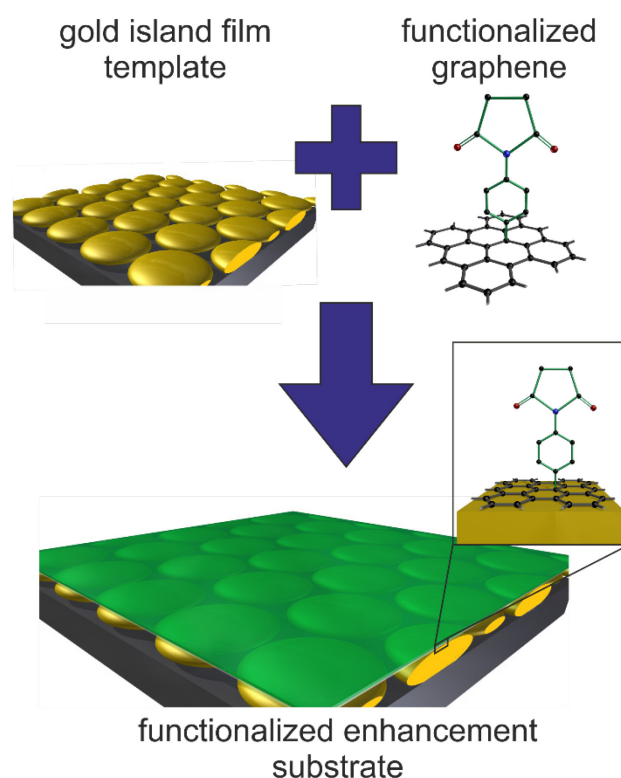


Figure 4-28: General scheme of introducing surface functionalization to an enhancement substrate by transfer of pre-functionalized graphene.

In this scheme the preparation of the functionalization can be fully separated from the enhancement substrate. The numerous protocols known for the functionalization of graphene furthermore substantially increases the possibilities in the surface functionalization.²¹⁹⁻²²¹ The so formed hybrid materials may present auspicious candidates for sensing applications as the surface modification can be covalently attached to the graphene sheet and can provide surface functionalizations where the direct preparation on the enhancement substrate itself may be difficult or impossible.

The functionalization of graphene can *e.g.* be achieved with electrochemical methods using diazonium salts.¹⁷³ Further modifications and secondary functionalization if necessary can subsequently also be performed on the graphene. The graphene with the desired functionalization is then transferred to the enhancement substrate using the method introduced in section 2.5.2¹⁷² developed at the HZB by Rösicke *et al.*^{174, 222}. In principle properties of the functionalization as *e.g.* homogeneity or presence of functional groups on the graphene can be evaluated prior to the transfer to the enhancement substrate.²²² The preparation and functionalization of the graphene as well as the transfer of the

graphene to the enhancement substrate was performed by Dr. Felix Rösicke at the Helmholtz-Zentrum Berlin.

4.3.1. Characterization of the effect of the graphene on the enhancement properties of the enhancement substrate

In the preparation of the surface functionalization the enhancement properties of the enhancement substrate must not be negatively altered. In order to examine the effect of the transferred functionalized graphene on the enhancement properties a gradient gold island film on a silicon substrate and a transfer of pre-functionalized graphene with para-(maleimidophenyl) (p-MP) residues to the substrate were used

The enhancement properties of the substrate were evaluated with IR mapping microscopy by determining the enhancement of the vibrational signature associated with the native oxide $\nu(\text{SiO}_2)$ on the silicon (comp. section 2.3.4 & section 4.1.2) before and after the transfer of the graphene.

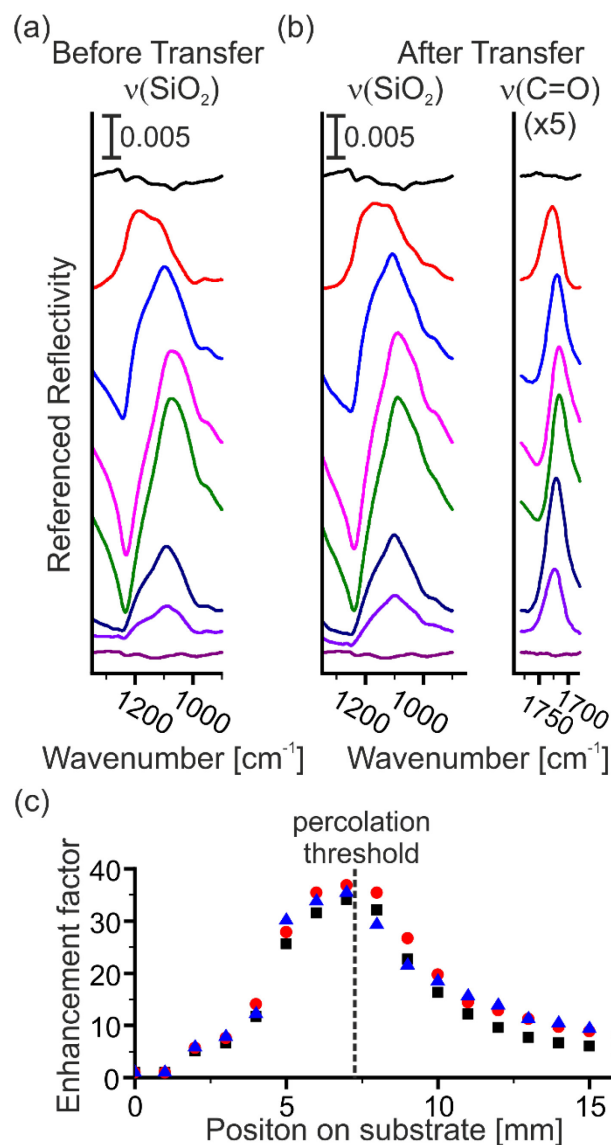


Figure 4-29: Enhancement properties of gradient gold island film substrate before and after transfer of functionalized graphene. (a) Exemplary baseline corrected IR microscopy reflection spectra of the native oxide vibrational band before transfer of graphene. (b) Exemplary baseline corrected IR microscopy reflection spectra of the native oxide vibrational band after transfer of graphene and $\nu(\text{C=O})$ of the p-MP

functionalization. (c) Mediated enhancement along gradient substrate for the native oxide band before (■) / after (●) transfer of graphene and for the $\nu(\text{C}=\text{O})$ vibration (▲) of the functionalization.

The IR reflectivity spectra in Figure 4-29 (a) and (b) show the vibrational signature of the native oxide $\nu(\text{SiO}_2)$ before and after the transfer along the gradient substrate. In addition in Figure 4-29 (b) the $\nu(\text{C}=\text{O})$ vibrational band of the p-MP residues of the functionalized graphene at the same positions are shown. The enhancement factors calculated for the $\nu(\text{SiO}_2)$ before and after the transfer as well as the enhancement factors obtained for the $\nu(\text{C}=\text{O})$ vibrational mode are depicted in Figure 4-29 (c). The enhancement factor of the $\nu(\text{C}=\text{O})$ vibrational mode was calculated using the data of the dielectric function of p-MP from Kanyong *et al.*⁴⁵.

The comparison of the amplitude and shape of the $\nu(\text{SiO}_2)$ vibrational band before and after the transfer shows no relevant changes for all different island film morphologies present along the gradient substrate. Subtle changes in the low wavenumber region are a consequence of the presence of a vibrational band of the functionalization. No negative effects of the functionalization on the enhancement performance can be identified from the enhancement factors of the $\nu(\text{SiO}_2)$ vibrational band. After the transfer the enhancement factors are even slightly increased. The analysis of the enhancement of the $\nu(\text{C}=\text{O})$ vibration shows that the enhancement mediated by the substrate is also provided for the functionalization. In the following the slight increase in the enhancement performance was investigated.

In order to gain an understanding of the changes in the optical properties of the enhancement substrates upon transfer of pre-functionalized graphene, UV-Vis ellipsometry was used for the characterization of the optical properties. The ellipsometry data gives access to the pseudo-dielectric function (comp. subsection 2.4.2) of the substrate before and after functionalization which allows to investigate the changes in the plasmonic resonance properties of the substrate.

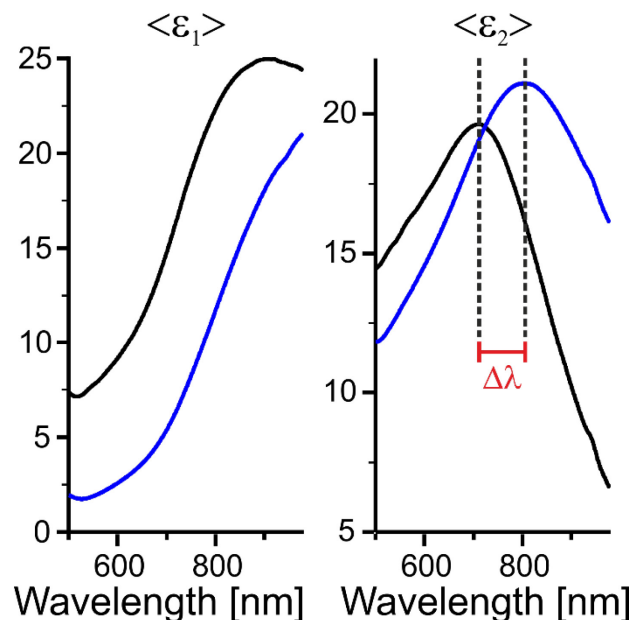


Figure 4-30: Plasmonic properties of enhancement template measured before and after graphene transfer. Exemplarily shown for the position of maximum enhancement before (black) and after (blue) transfer of the p-MP functionalized graphene. The resulting shift of λ_{max} is indicated as $\Delta\lambda$.

The real $\langle \epsilon_1 \rangle$ and the imaginary part $\langle \epsilon_2 \rangle$ of the pseudo-dielectric function of the enhancement substrate before (black) and after (blue) the graphene transfer is exemplarily shown for the position of maximum SEIRA enhancement (Figure 4-30). The deposition of the functionalized graphene on the gold island film leads to a red-shift $\Delta\lambda = (108 \pm 3)$ nm and a broadening of the resonance. Similar

results were obtained for all other positions along the gradient island film where SEIRA enhancement was observed.

The red-shift of the resonance can be used to determine the thickness of the adsorbate layer on the gold island film (comp. section 2.3.1 & 2.4.4). To determine this relationship, a simulation of the functionalized gold island film substrates was carried out and the theoretical pseudo-dielectric function was calculated. The film parameters for the simulation were obtained by fitting to the corresponding IR reflectance spectrum of the unmodified gold island film.

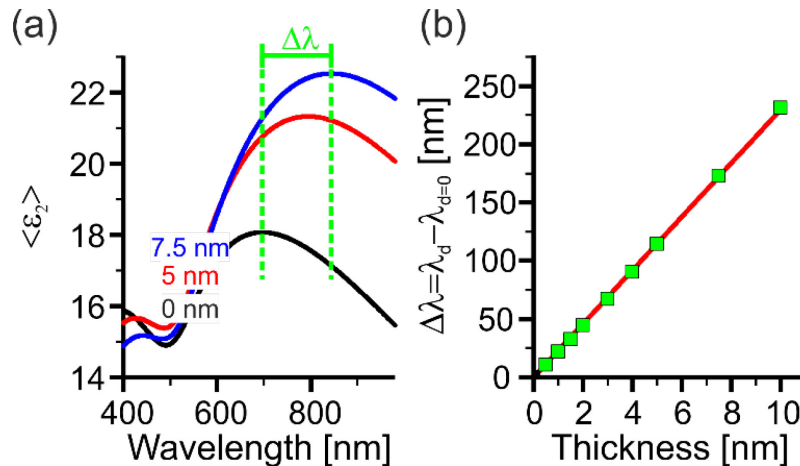


Figure 4-31: Dependence of the shift of the central wavelength of the plasmonic resonance on the thickness of adsorbed layer. (a) Imaginary part $\langle \epsilon_2 \rangle$ of the pseudo-dielectric function of metal island film close to the percolation threshold with adsorbate layer thickness of 0 nm, 5 nm and 7.5 nm (calculated using the optical model introduced in chapter 2.4.4 with exemplary parameters: $a=28.35$ nm, $c=9.7$ nm, $f=0.12$, $n_{\text{coating}}=1.5$, $n_{\text{si}}=3.42$). (b) $\Delta\lambda$ of resonance in dependence on adsorbate layer thickness.

Figure 4-31 shows in (a) the calculated plasmonic resonance for different adsorbate layer thickness and in (b) the corresponding shift in the central frequency of the plasmonic resonance of the gold island film. It has to be noted that the simulation is only qualitative as assumptions were made about the refractive index of the coating and deviations arise from the factors described in section 2.4.4.

Using a linear fit to the simulated data set in Figure 4-31 (b) and transferring this relation to the experiment, a p-MP graphene thickness of (4.7 ± 0.3) nm can be estimated. This is in good agreement with other measurements by IR-ellipsometry and AFM reporting a thickness of the p-MP graphene of (4.8 ± 0.5) nm respectively (5.8 ± 0.6) nm for a similarly prepared p-MP functionalized graphene on a gold surface.¹⁷² This result demonstrates that the analysis of the plasmonic resonance of the gold island film can serve as an additional complementary route to determine the thickness of adsorbate layers on the islands.

The model also confirms that a red-shift of the resonance and a corresponding broadening are to be expected for the deposition of the p-MP graphene. In the application of SEIRA this red-shift and broadening of the resonance is advantageous as the overlap between the plasmonic resonance and the molecular vibration is increased, resulting in an increased enhancement.¹³⁶

In summary surface functionalization via the transfer of pre-functionalized graphene has no negative influence on the enhancement properties of the enhancement substrate. In consequence this technique poses a novel way to obtain surface functionalization of enhancement substrates which does not depend on the surface chemistry of the enhancement substrate.

4.3.2. Hybrid substrates for *ex situ* applications

The functionality of the surface functionalization is as crucial in the preparation of surfaces for sensor applications as the enhancement. The functionality of the surface functionalization on the hybrid-substrate was examined by evaluating the adsorption of GSH on the p-MP residues. The hybrid substrate was exposed to an aqueous solution of GSH (5 mM) for 16 h. Afterwards the sample was thoroughly rinsed with DI-water several times and dried using dry air. IR reflectivity spectra were recorded prior and after the exposure to the solution at the position of maximum enhancement.

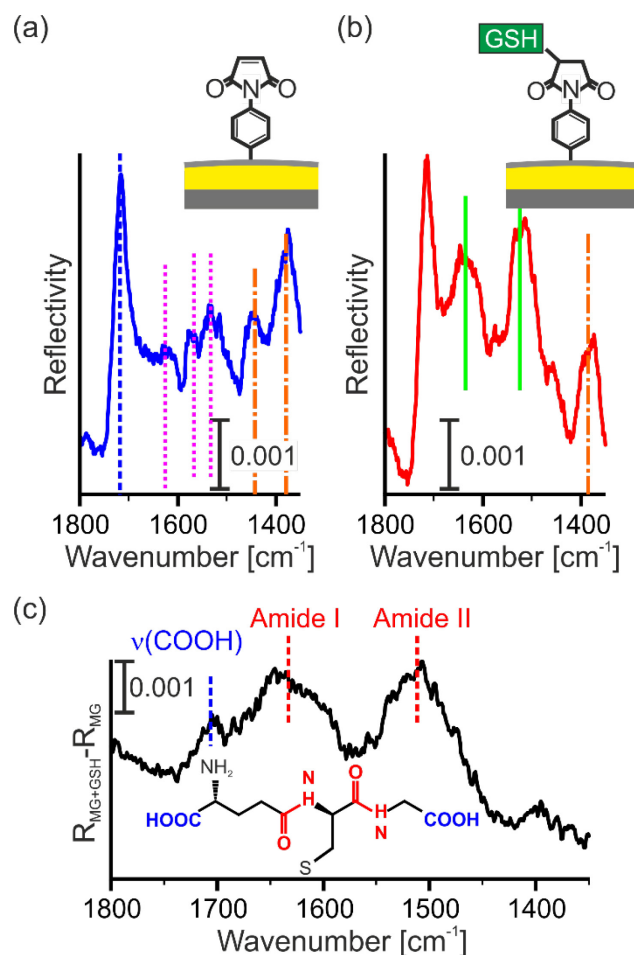


Figure 4-32: Binding of GSH to p-MP graphene functionalized gold island film. Baseline corrected IR microscope spectrum of p-MP surface (a) before binding of GSH and (b) after binding of GSH. (c) Difference spectrum of bound GSH with indication of observed vibrational modes.

In the IR reflectivity spectrum of the unexposed hybrid substrate (Figure 4-32 (a)) characteristic vibrational bands of the p-MP residues can be observed. The stretching vibration $\nu(\text{C}=\text{O})$ around 1716 cm^{-1} , the vibrational band of the phenyl-ring around 1595 cm^{-1} and bands associated with the vibration of the imide-ring around 1430 cm^{-1} and 1380 cm^{-1} .⁴⁵ After exposure to the solution two strong and broad vibrational bands indicated in Figure 4-32 (b) characteristic of GSH were observed. These bands are the amide I (around 1630 cm^{-1}) and the amide II (around 1510 cm^{-1}) vibrations of the GSH.²⁰⁶ In order to reveal the vibrational signature solely of the GSH a difference spectrum of the reflectivity recorded on the modified and unmodified sensor substrate is shown in Figure 4-32 (c). In this spectrum also the vibration associated with the carboxylic-groups of the GSH can be identified as a shoulder of the amide I band around 1705 cm^{-1} .

The adsorption of GSH on the substrate was furthermore evaluated using UV-Vis ellipsometry with the previously introduced procedure.

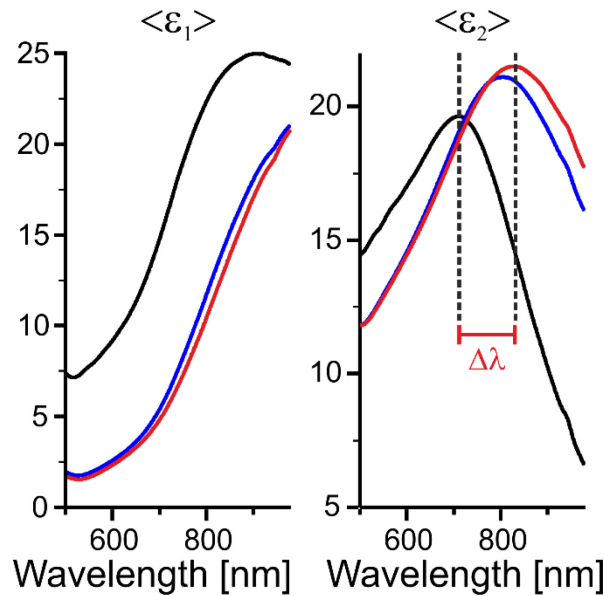


Figure 4-33 Pseudo-dielectric function of the sensor substrate before (black) and after (blue) transfer of the functionalized graphene and after exposure of the sensor substrate to GSH (red)

The binding of the GSH to the surface of the sensor substrates leads to a further red-shift of the resonance. Compared to the unmodified island film the plasmonic resonance is shifted by (131 ± 3) nm and compared to the island film after graphene functionalization by (23 ± 4) nm.

GSH has a similar refractive index as the p-MP graphene. It can therefore be assumed that the red-shift of the plasmonic resonance will show the same linear dependence on the film thickness as presented in Figure 4-31 (b). Under this assumption the red-shift of the plasmonic resonance corresponds to an increase in adsorbate layer thickness of $\approx (1.0 \pm 0.2)$ nm. This value is in good agreement with a reported thickness of a monolayer of GSH of approx. 1.2 nm.²²³

From the presented results it can be concluded that novel hybrid sensor substrates were obtained by pairing functionalized graphene with enhancement substrates. In addition it could be shown that the investigation of the LSPR and especially the shift of the resonance maximum provides a complementary access to determine the film thickness and changes thereof for adsorbate layers on the gold island film.

The presented route of functionalization is promising for obtaining target specific functionalization independent of the properties of the enhancement substrate while maintaining its enhancement properties. The detachment of the chemical preparation of the functionalization makes it possible to probe and validate the functionalization prior to the transfer²²². Moreover it allows the usage of chemicals and methods not compatible with the enhancement substrate without losing the enhancement. These type of hybrid substrates form auspicious candidates for *in situ* biosensing.

The shift in the maximum of the resonance presumably resulting from the change in the dielectric environment of the metal island film could potentially be used to gain a complementary access to information such as *e.g.* thickness of the deposited layer. The results show that this information can be used as a complementary tool to support the results from spectroscopic investigations. However, further analysis and investigations especially on island film morphologies are required in order to validate this approach.

4.3.3. Comparative study of (4-nitrobenzyl) mercaptane binding on gold island film and on p-MP graphene

The results presented in this section have in parts been published in: K. Hinrichs, T. Shaykhtudinov, C. Kratz, F. Rösicke, C. Schöniger, C. Arenz, N. H. Nickel and J. Rappich, in *Encyclopedia of Interfacial Chemistry*, ed. K. Wandelt, Elsevier, Oxford, 2018, pp. 80-94.

The applicability of the formed novel hybrid sensor substrates for *in situ* applications has been investigated. It was used to obtain evidence for a covalent binding of thiolate molecules to the imide group of the p-MP residue of the functionalized graphene *e.g.* by a Michael addition reaction. In this study the binding of an exemplary thiolate molecule ((4-nitrobenzyl) mercaptane (4-NBM)) to a p-MP functionalized enhancement substrate was compared to the adsorption process on an unfunctionalized gold island film. For the direct adsorption to the gold surface a fast Langmuir-type adsorption process is expected any deviation from this behavior in the second adsorption is indicative of a differing adsorption mechanism.

The study was performed using a gradient gold island film substrate with two SEIRA active regions on the same substrate. The enhancement in both regions was assessed before and after the transfer of the graphene. One of these regions was modified by transfer of graphene while the other was left unmodified schematically shown in Figure 4-34.

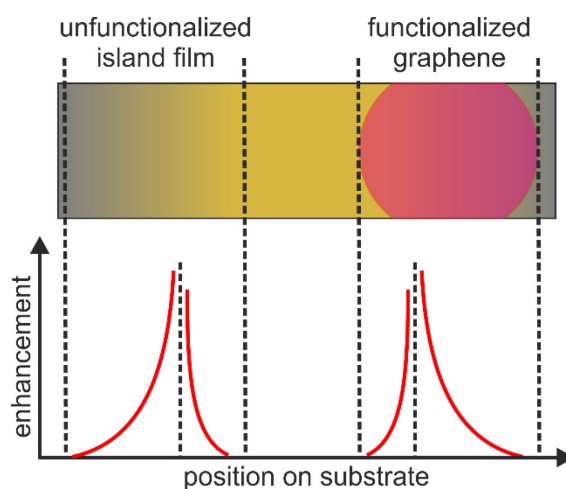


Figure 4-34: Schematic of double sided gradient gold island film substrate with one gradient functionalized with p-MP graphene and schematic of the obtained enhancement profiles.

The measurements were performed with a microfluidic chip of type I. For the experiment a 10 mM solution of 4-NBM in ethanol was prepared and flowed through the channels at a volume flow of 0.2 ml/h for 7 hours. Two measurement series were performed in two different channels of the microfluidic chip. In the first series the adsorption of the 4-NBM on the unmodified island film was monitored and in the second series the adsorption on the p-MP graphene functionalized island film.

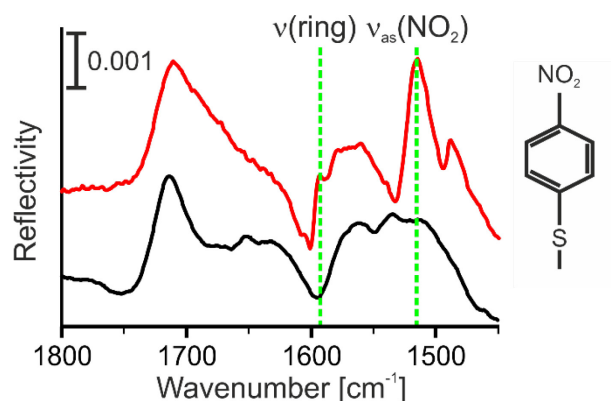


Figure 4-35: Baseline corrected *ex situ* IR-microscope reflection spectra of p-MP graphene functionalized metal island film before (black) and after (red) exposure to 4-NBM solution.

Figure 4-35 shows baseline corrected *ex situ* IR microscope reflection spectra of the p-MP graphene functionalized metal island film before and after exposure to 4-NBM solution. After the exposure to 4-NBM two characteristic vibrational bands of the 4-NBM can be identified. The ring vibration around 1598 cm^{-1} and the asymmetric stretching vibration of the nitro group $\nu_{\text{as}}(\text{NO}_2)$ around 1522 cm^{-1} . The $\nu_{\text{as}}(\text{NO}_2)$ vibration was chosen for evaluation as it shows the least overlap with the vibrational bands of the p-MP. The absorption was determined by time dependent monitoring of the peak amplitude of the asymmetric stretching vibration of the nitro-group $\nu_{\text{as}}(\text{NO}_2)$. Measurements were referenced to an initial spectrum recorded at the corresponding position in pure ethanol. In order to make the two measurements more comparable the peak-amplitudes were normalized to the maximum measured peak amplitude. Differences in the calculated peak-amplitudes may occur for different reasons as *e.g.* different enhancements or surface coverage. The latter is especially expected in this experiment as the number of binding sites for the 4-NBM may be significantly different for the two different surfaces investigated.

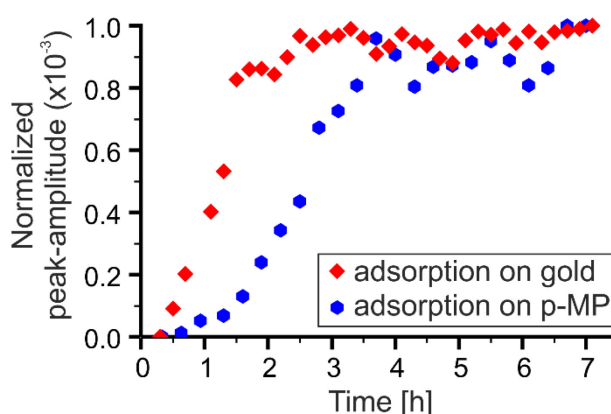


Figure 4-36: *In situ* monitoring of 4-NBM absorption process. Normalized peak amplitude of $\nu_{\text{as}}(\text{NO}_2)$ of unfunctionalized gold island film (red diamonds) and on p-MP graphene functionalized gold island film (blue hexagons). Adapted and reprinted with permission from Ref. [224]

In Figure 4-36 the normalized peak-amplitude of the $\nu_{\text{as}}(\text{NO}_2)$ vibration for the two different surfaces under investigation are shown. On the unfunctionalized gold island film a fast adsorption similar to the adsorption observed for the 4-MBN monolayer formation (comp. section 4.2.2) was observed. The adsorption kinetics shows good agreement with first order Langmuir-type adsorption and a saturation of the binding is observed after approx. 2.5 h. For the adsorption of 4-NBM on the p-MP functionalized gold island film the adsorption process is much slower as the adsorption takes 3.7 h to reach the level

Results & Discussion

of saturation. It is also to be observed that the absorption kinetics shows a strong deviation from Langmuir-type absorption.

The observed deviation from first order Langmuir-type absorption and the considerably slower binding can be interpreted as a result of a different adsorption mechanism. The form of the adsorption curve may therein be indicative for a reaction with an intermediate state or an autocatalytic reaction.^{225 174}

The experiment shows that the obtained surface functionalization of the hybrid sensor substrates can be applied for *in situ* sensing applications. The presented method for the preparation of hybrid sensor substrate forms an alternative to the direct surface modification of the enhancement substrates. It may considerably enlarge the range of possible surface modifications of enhancement substrates of metal island films as the preparation and pre-characterization of the surface modification can be done independently of the enhancement substrate.

5. Summary & conclusion

The presented experiments and results demonstrate that *in situ* SEIRA spectroscopy can be applied as a detection technique in an optofluidic device with nL sample volumes. Sub-monolayer sensitivity for measurement times in the range of minutes could be shown investigating the formation of model SAMs of 4-MBN and GSH. The high sensitivity of the proposed optofluidic platform allowed for a sufficient time resolution to monitor the formation of the SAM from approx. 25% monolayer coverage and to determine the kinetics of the formation process. Estimation of the LOD from the formation of the SAM showed that a LOD < 15 ng/cm² can be achieved translating to a LOD_M of only a few picogram. The dissociation/protonation of the carboxylic groups in the model system of an approx. 1.2 nm thick GSH SAM in response to a change in environmental pH could be measured. The experiment showed that the response to environmental stimuli could be investigated on the sub-monolayer level. The system of biotin-streptavidin served as a model that the recognition of a protein on a functionalized surface can be achieved. The binding of the streptavidin to a biotinylated enhancement substrate could be monitored and the IR spectra the expected signature of a protein. The obtained LOD may not be on the order of single molecule detection but in comparison to *e.g.* techniques sensitive only to a change in the refractive index as *e.g.* resonant cavities vibrational spectra over the full spectral range could be obtained by applying SEIRA spectroscopy for the detection. These spectra can be used for the identification of the molecule and in the case of proteins their secondary structure. Furthermore in conjunction with suitable optical models the vibrational information could in the future be used to investigate *e.g.* interaction processes, changes in the secondary structure in response to external stimuli or ligand binding. The shown concept is a versatile approach to integrate SEIRA spectroscopy in optofluidics.

The correlation between morphology, plasmonic and enhancement properties of the utilized enhancement substrates was investigated, The use of enhancement substrates with a gradient in gold film thickness allowed one further detailed insights in these properties as all different morphologies ranging from small isolated islands over island films close to the percolation threshold to closed gold films can be investigated on a single substrate. This is of large advantage as the variation in substrate properties, pre-cleaning, deposition and functionalization of the substrate can be reduced. A correlation between the enhancement and the shift of the plasmonic resonance to the infrared region with growing island size and fill-factor has been observed. Maximum enhancement was found for island films close to the percolation threshold in agreement with *e.g. Osawa et al.*⁶⁹. In agreement with Fahsold *et al.*¹¹⁶ enhancement could also be observed above the percolation threshold. In the application such substrates may be used to obtain an on substrate tunability of the enhancement allowing one to adjust the enhancement to the needs of the experiment at hand. A tunable enhancement can also be of high importance if the vibrational fingerprint is to be analyzed at different enhancements to account for the asymmetry in the vibrational bands. Furthermore these gradient substrates can be used to find the optimum film-thickness and preparation parameters for enhancement substrates with homogeneous thickness of the gold film using a single substrate.

Gradient gold island film substrates have been used to study the possibility to obtain an *a priori* and target independent assessment of the enhancement provided by gold island films. With this respect the correlation between the enhancement of the vibrational signature of the native oxide and the enhancement of the vibrational bands of SAMs of 4-MBN and 4-MBA has been investigated. The vibrational signature of the native oxide was chosen as the native oxide is an inherent feature of the silicon substrates used here for enhancement substrate preparation. It could be shown that the enhancement of the native oxide mode is not influenced by the deposition of the organic material. The enhancement of the native oxide signature is furthermore correlated with the enhancement of the

Summary & conclusion

vibrational bands of the organic SAM on top of the gold island film. The spatial correlation can be used to choose an optimized measurement position on a gradient gold island film prior to the deposition of the material of interest or to extract the optimum effective thickness for the preparation of a homogenous substrate. The correlation between the enhancement of the signature of the native oxide and the enhancement of the vibrational modes of the SAMs has been further investigated. The investigation showed that a correlation of the enhancement could potentially be deduced. The experimental results however showed a large variation and further studies will need to be performed concerning the components of the native oxide signature and the variations of the native oxide itself to clarify the correlation. Also statistical methods could be used if a larger data set were at hand.

A problem often encountered for vacuum evaporated enhancement substrates is the contamination of the substrate with “advantageous” hydrocarbons and other organic compounds. These contaminations have vibrational bands which potentially overlap with the vibrational bands of the molecule of interest. Furthermore they may block the surface for the attachment of other molecules which may prevent the formation of a SAM on the surface. In consequence the effect of these contaminations on the formation of SAMs formed from thiolate molecules on the surface of the enhancement substrates have been investigated. Two exemplary SAMs of 4-MBN and GSH have been examined. The investigation showed that the contaminations on the two substrates had a varying ratio of $-\text{CH}_2$ and $-\text{CH}_3$ functional groups on the surface before the deposition of the SAMs as determined from the ratio of the intensities of the corresponding vibrational bands. For both investigated SAMs characteristic vibrational bands of the 4-MBN and GSH could be found respectively after the deposition. After the deposition of the SAM the intensity of vibrational bands related to the contaminations was strongly reduced. In the case of 4-MBN the amplitude of the vibrational bands was reduced to less than 12 % and for GSH to less than 25 %. It has to be noted that in the case of 4-MBN the molecule itself contains neither $-\text{CH}_2$ nor $-\text{CH}_3$ functional groups while in the case of GSH the molecule itself has several $-\text{CH}_2$ groups in different chemical configurations. This may complicate the analysis of the vibrational bands in the case of GSH and result in an underestimation of the removal, as the vibrational bands of associated with $-\text{CH}_2$ functional groups may show components which overlap with the vibrational bands previously associated with $-\text{CH}_3$ functional groups. The difference in the efficiency of the removal of the contaminations may also be found in the different surface densities of the two investigated monolayers $\Gamma_{\text{GSH}} / \Gamma_{4\text{-MBN}} \approx 0.25$. The results of this analysis showed that SAMs can be successfully formed on surfaces of enhancement substrates which show vibrational signatures of contaminations and the formation of the SAMs leads to a reduction of these vibrational signatures. They also show that the contaminations of the surface must be investigated if molecules as *e.g.* lipids with vibrational modes of interest in the region of the symmetric and asymmetric stretching vibration of $-\text{CH}_2$ and $-\text{CH}_3$ functional groups are to be investigated.

The deposition of an SAM on the gold island film changes the dielectric environment of the plasmonic surface. As a result of this change a shift of the plasmonic resonance is expected. This effect has been investigated for three model SAMs of GSH, 4-MBA and 4-MBN on gradient gold island film substrates. The utilization of gradient gold island films herein allowed one to study the effect for different island film morphologies *i.e.* for different plasmonic resonances. The resonance was characterized by UV-Vis ellipsometry, calculating the pseudo-dielectric function and examining the imaginary part of the former. For all three investigated monolayer a shift in the plasmonic resonance could be observed which was the highest for the island films with a plasmonic resonance at low-wavelength values *i.e.* small isolated metal islands but could also be observed up until the percolation threshold. The degree of the shift for the three different SAMs was $\Delta\lambda_{\text{MBA}} > \Delta\lambda_{\text{GSH}} > \Delta\lambda_{\text{MBN}}$ which correlates well with the expected $n \cdot d$ values for the investigated SAMs. In summary a shift of the plasmonic resonance could be observed as a result of the deposition of an organic SAMs on the gold island film. This shift could on

Summary & conclusion

the one hand be used as a complementary source of information for the formed SAM as in LSPR sensing. On the other hand the shift in the plasmonic resonance has to be taken into account in the analysis of IR spectra as it results in a shift and change in curvature in the baseline of the IR reflection spectra.

The introduced theoretical model for the metal island films using a Bruggeman EMA with coated oblate spheroids has been implemented in MATLAB and tested for its applicability to simulate *ex situ* IR microscopic SEIRA spectra. The implemented model can reproduce the experimentally observed baseline for different island film morphologies. The simulation of a 4-MBN SAM with oscillator parameters derived from an IR ellipsometric measurement however showed that the measured enhancement cannot be reproduced by the simulation and is smaller by a factor of approx. 3. This deviation may in part result from the effect that local field enhancement cannot be accounted for by the employed EMA model. In order to account for this effect numerical calculations have to be performed. If the oscillator parameters are derived from fitting to an initial island film morphology on a gradient island film the amplitudes of the vibrational bands for other island film morphologies on the same substrate can however be modeled with good agreement. This result indicates that maybe also the chosen method to obtain the oscillator parameters has to be revised and that the vibrational properties of the SAM may be altered by the enhancement substrate. Further research has to be performed to clarify these observations. The proposed model and its implementation however work well for the qualitative description of the measured IR spectra. It can especially be used to simulate a baseline to remove the influence of the metal island film from the IR spectra for a simplified analysis of the vibrational bands. The model is so far limited to model *ex situ* IR spectra, in order to perform optical modeling of *in situ* spectra the model needs further development and modifications. For example the effect of the solvent has to be taken into account as it changes the dielectric environment of the island film which has to be accounted for.

The developed optofluidic platform allows for *in situ* IR measurements with and without enhancement. In a model experiment it was shown that the hydrolysis reaction of ethyl acetate and sodium hydroxide to ethanol and sodium acetate can be monitored in a microfluidic channel. In this experiment it could be shown that the time dependence of the hydrolysis could in principle be monitored. It was refrained from determining reaction kinetics as the initial concentrations and the degree of mixing could not be determined. However an exponential trend of the reaction could be determined as expected for the reaction. The experiment showed that without enhancement the vibrational bands of the ethyl acetate could potentially be detected down to a level of 0.6 vol. % of ethyl acetate in the solution. These results show in principle that also without using enhancement surfaces, processes within the volume of the microfluidic channel can be investigated with the presented concept.

In combination with the optimized enhancement substrates the optofluidic platform has been employed to investigate the adsorption kinetics in the formation of a 4-MBN and a GSH SAM. The 4-MBN SAM was prepared from a solution in ethanol and the GSH SAM from an aqueous solution. In both cases the adsorption of the molecules on the enhancement surface could be followed with sub-monolayer sensitivity and a time resolution of minutes. The time-dependent monitoring of the vibrational band amplitudes of the molecules showed a Langmuir-type adsorption curve. The measurement could be used to determine the kinetics of the adsorption process. In the case of 4-MBN the adsorption-rate constant was (62 ± 6) L/(mol s) and (8.6 ± 0.3) L/(mol s) for GSH respectively. The LOD was estimated under the simplifying assumption that a linear correlation between band amplitude and the number of molecules can be assumed for a dilution of molecular groups in the surface layer contributing to the adsorption band. The determined LOD was (13.5 ± 0.7) ng/cm² in the case of the 4-MBN and (10.5 ± 0.6) ng/cm² for the GSH SAM. In both cases the monolayer growth could be followed from about 25% surface coverage. Taking into account the estimated measurement area of

Summary & conclusion

$(3.0 \pm 0.5) \times 10^{-4} \text{ cm}^2$ for the used microfluidic chip the LOD_M was $(4 \pm 1) \text{ pg}$ or $(30 \pm 16) \text{ fmol}$ for 4-MBN and $(3 \pm 1) \text{ pg}$ or $(10 \pm 2) \text{ fmol}$ in the case of GSH. The performed experiments illustrate that highly sensitive *in situ* SEIRA spectroscopy at the solid—liquid interface is feasible on microfluidic volumes. The obtained sensitivity will allow for time-dependent monitoring of the vibrational bands of molecules adsorbing to the surface of the enhancement substrate.

The approximately 1.2 nm thick GSH SAM served as a model system to investigate whether processes at the solid—liquid interface could be resolved on the monolayer level. The GSH SAM served as a model system as its carboxylic groups dissociate/protonate under alkaline respectively acidic pH in the environment of the SAM.^{207, 209} A decrease respectively increase of the vibrational band associated with the carboxylic groups and the respective ions was found for the SAM in an alkaline environment compared to the as-grown state. The reversed trend could be observed in the case of an acidic environment. The experiment showed that in agreement with Bieri *et al.*²⁰⁷ the carboxylic groups of the GSH are partially dissociated in the SAM after its formation. It also showed that the SAM can be switched from a dissociated state to a protonated state by proper adjustment of the environmental pH. This switching could be monitored time-dependently showing that in principle also the time-dependence *i.e.* the kinetics of changes within a monolayer can be investigated.

The recognition of streptavidin by a biotinylated surface was used as a model system to show the possibility to investigate protein adsorption on a surface and proteins immobilized at the solid—liquid interface. In the experiment the recognition of streptavidin on a biotinylated enhancement substrate could be monitored. Characteristic vibrational bands of streptavidin^{52, 210} in the amide I and amide II region could be observed in the process of the adsorption to the surface. The LOD was determined as before and resulted in an LOD of $(7.1 \pm 0.3) \text{ ng/cm}^2$ or a LOD_M of $(2.1 \pm 0.4) \text{ pg}$. The vibrational bands in the amide regions are of high interest for the study of the secondary structure of the protein. Changes in these vibrational bands could be observed during the adsorption and further studies have to be performed to elucidate the origin of these changes. The experiment shows that small amounts of proteins immobilized on a functionalized enhancement surface can be investigated by the presented concept. This will be of high interest in the future development of the technique as it may enable one to investigate the effect of external stimuli on the protein secondary structure and may enable to monitor changes as a result of *e.g.* ligand binding.

The surface functionalization of enhancement substrates plays a key role in the immobilization of a target molecule on the surface. The possibility to obtain a novel type of hybrid sensor substrate introducing the surface functionalization to the enhancement substrate by the transfer of pre-functionalized graphene has been investigated. Electrochemically functionalized graphene with p-MP residues was transferred to a previously characterized gradient gold island film substrate at the HZB. The analysis of the vibrational signature of the native oxide before and after the transfer showed that enhancement provided by the substrate is retained after the transfer of the functionalized graphene. The same enhancement could also be observed for the vibrational band of the carbonyl group of the p-MP residues. The shift of the plasmonic resonance observed in the pseudo-dielectric function in the UV-Vis spectral region could be used to estimate a thickness of the p-MP graphene of $(4.7 \pm 0.3) \text{ nm}$. This value is in good agreement with the value obtained from simulation of IR-ellipsometry data and AFM measurements reporting a thickness of $(5 \pm 1) \text{ nm}$ for the p-MP functionalized graphene.^{174, 222, 224}

The possibility to immobilize molecules on the hybrid sensor substrates has been investigated *ex situ* by exposing the substrates to an aqueous solution of GSH. After the exposure the characteristic vibrational bands of GSH could be observed in the SEIRA spectra. The analysis of the shift in the plasmonic resonance gave a film thickness of $(1.0 \pm 0.2) \text{ nm}$ for the GSH layer, in good agreement with values of 1.2 nm film thickness reported for GSH monolayers by Fang *et al.*²⁰¹. The experiment showed

Summary & conclusion

that the introduced surface functionalization can be used for the immobilization of molecules on the surface of the enhancement substrate.

The hybrid substrates have also been tested for their applicability for *in situ* measurements. A study has been performed to compare the adsorption kinetics of 4-NBM on a gold island film to the adsorption of the same molecule on p-MP graphene. In this study a double sided gradient was used where one side of the substrate was left blank and the other was functionalized by transfer of p-MP-graphene. The study showed that the adsorption of the 4-NBM is much slower on the p-MP than on the gold island film. Different adsorption kinetic were observed in the two investigated cases where the adsorption on the gold island film had a Langmuir-type adsorption curve while the adsorption on the p-MP showed a distinct deviation from a Langmuir-type adsorption curve. This differences were identified as an indicator that the adsorption of the 4-NBM on the p-MP is more likely a binding reaction of the molecule to the imido-group of the p-MP than a physisorption process.^{222, 224}

In summary several experimental studies have been successfully performed to investigate processes at the solid—liquid interface using microfluidic volumes. The results of the experiments highlight the potential of the developed concept for different applications. It combines the highly sensitive *in situ* molecular detection and access to structural information of SEIRA spectroscopy with the possibility handle and manipulate nL to μ L volumes on microfluidic chips for the analysis. This development can be of high interest for the analysis of molecular interaction as protein-protein interactions, receptor-ligand binding or processes at lipid-membranes as it distinctively reduces sample consumption. The high sensitivity may also be of interest in the development of novel label-free structure-sensitive biosensing concept. The presented approach for the formation of hybrid sensor substrates pairing functionalized graphene and enhancement substrates opens up a vast potential for novel surface functionalization.

In the future the adaption of an optical model for the simulation of the enhancement substrates under *in situ* conditions has to be made to allow one for a detailed analysis *e.g.* of interaction processes at the solid—liquid interface. To this point only qualitative simulations of *ex situ* spectra are possible. In the pursuit of developing a suitable optical model the effects of the *in situ* condition on the optical and plasmonic properties of the metal islands in the experiments have to be investigated and appropriately accounted for in the optical model.

The investigation of processes at the solid—liquid interface processes as already demonstrated can be further improved for detailed analysis of adsorption/desorption kinetics at the solid—liquid interface or to study structural changes in peptides or proteins. The immobilization route for biotinylated biomolecules demonstrated using the biotin-streptavidin system should be further investigated to enable a translation towards biosensing applications. Furthermore alternative routes for the immobilization of bio relevant molecules on the enhancement surface should be explored. A promising route for the immobilization of biomolecule are metal-chelated surfaces as *e.g.* nickel chelated nitrilotriacetic acid (Ni-NTA) SAMs which bind the biomolecule via a histidine-tag. This route may be of great interest as it is widely used in the isolation and enrichment of proteins from biological samples in the Ni-NTA based enrichment. The molecules isolated by this method could be directly used for the analysis in the optofluidic platform and different protocols for the formation of Ni-NTA SAMs on SEIRA substrates already exist.^{20, 74, 76, 226} In comparison to the biotin-streptavidin system a Ni-NTA SAM could directly immobilize the protein of interest and interferences resulting from the relatively large protein streptavidin in the measurement could be avoided. In addition the Ni-NTA system would provide the possibility to use established protocols to (partly) remove the modified and characterized biomolecules *e.g.* by use of ethylene diaminetetraacetic acid (EDTA) or imidazole from the surface. This property could be used on the one hand to make the enhancement substrates reusable if the Ni-NTA surfaces

Summary & conclusion

can be recharged. For this possibility the knowledge from the Ni-NTA chromatography could be employed where Ni-NTA columns are routinely reused. On the other hand by collecting the aliquot with the characterized biomolecule it would be available for further analysis with complementary downstream analytical techniques as *e.g.* mass spectrometry or NMR spectroscopy. Another interesting approach for the targeted binding of molecules on the surface is given by the development of aptamers, which may show an even higher affinity towards the target molecule than antibodies and may bind a large variety of targets ranging in size from small molecules over proteins to cells. In consequence aptamers would be highly interesting for the surface immobilization.

In the instrumental development of the concept several further developments could be pursued.

A temperature control system *e.g.* using a Peltier element based temperature control should be integrated on the optofluidic platform. Such a system would be highly beneficial to increase temperature stability during the experiment which so far is ensured by temperature control of the lab itself. It would furthermore open up the possibility to investigate temperature dependent effects as the response of thermo-responsive polymer brushes or temperature dependent denaturation processes of proteins.

In the second place the developed gradient enhancement substrates can potentially be used for SERS and SEIRA enhancement²²⁷. By changing the observation window from silicon to an UV-Vis and IR transparent material as CaF₂ complementary studies with SERS and SEIRA giving access to complementary vibrational information could be made feasible. On the one hand this combination may provide two fingerprints of the molecule under investigation for the identification of the molecule potentially increasing the identification rate. On the other hand such a combined setup can provide complementary information *e.g.* on inter- and intramolecular processes. The implementation of UV-Vis transparent substrates could furthermore be used to implement further complementary online measurement techniques as *e.g.* LSPR or fluorescence spectroscopy providing additional information which can be used for further analysis or to verify the obtained results. These integrations would realize a “multi-spectroscopy” optofluidic platform enabling multimodal analysis of nL to μ L volumes on a single chip.

In the further development for SEIRA spectroscopy the possibility to perform SEIRA ellipsometry measurements could be highly beneficial. This method is a reference free measurement technique and can provide a more detailed access to molecular information *e.g.* molecular orientation and anisotropies within the thin films. The combination of the optofluidic platform with novel high brilliance light source as *e.g.* quantum cascade lasers (QCL), also in the context of performing IR ellipsometry, will be beneficial for the detection as the higher photon-flux may drastically decrease measurement times and may increase sensitivity by improving the signal-to-noise ratio. Such an ellipsometer could furthermore allow one to have a better defined angle of incidence and to change the angle of incidence to the needs of the experiment. This may potentially also increase sensitivity and may be advantageous for the optical simulations as multiple data sets under different angles of incidence can be used for analysis.

6. Outlook

The presented concept of an optofluidic platform for IR and SEIRA spectroscopy on a microfluidic chip may have numerous further applications. In the following a few ideas are shown where the general possibilities have been briefly investigated.

Chemical imaging of microfluidic channels and components

Microfluidic chips *e.g.* for lab-on-a-chip (LOC) or organ-on-chip applications may contain numerous components *e.g.* for fluid manipulation, reaction and control on a single chip. On such complex systems it may be of advantage to obtain vibrational information at different locations of the chip to gain access to information on *e.g.* reactions or interactions in the different compartments of the chip during the experiment. This may also be of potential interest *e.g.* in the screening of drug targets or enable multi analyte analysis on a single chip by evaluating the vibrational signal obtained from different channels. As an example the measurement of different sample solutions on a single multi-channel microfluidic chip has been examined.

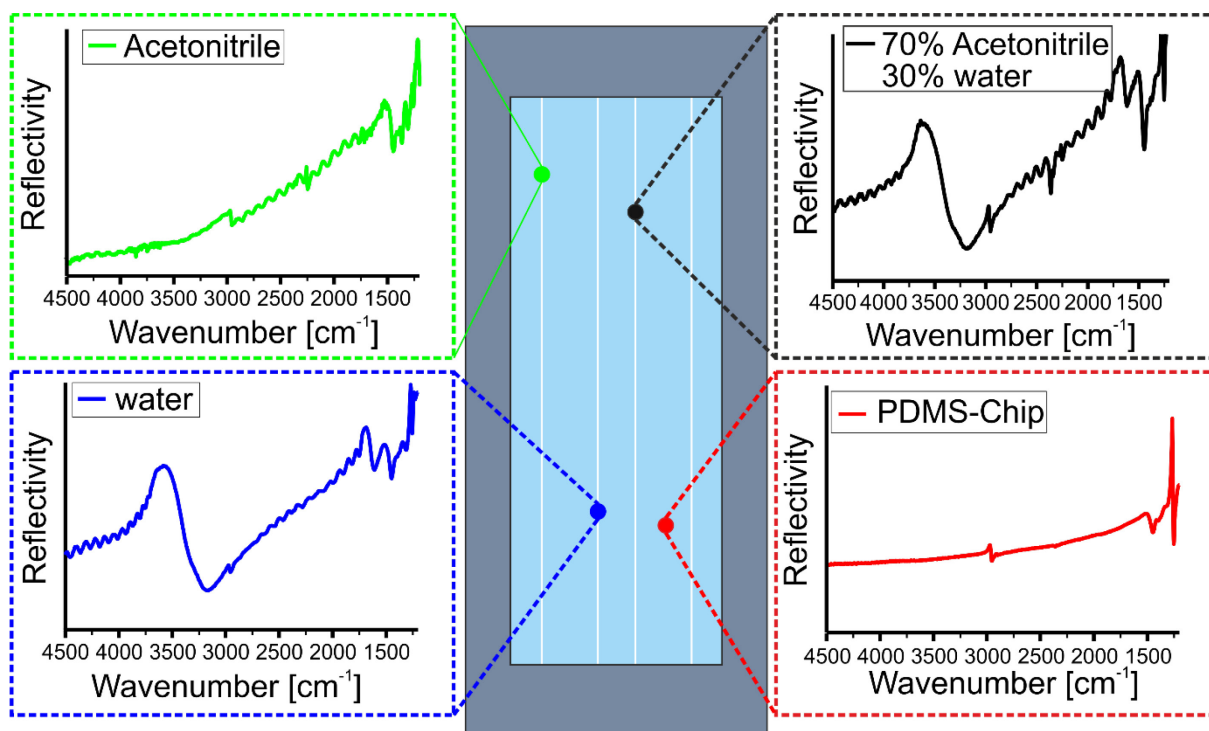


Figure 6-1 Accessible measurement area of optofluidic platform. Exemplary IR reflectivity spectra recorded on a Type I microfluidic chip. Channels contain different analytes as indicated in the corresponding spectra.

In consequence of the large accessible measurement area of the optofluidic platform different channels and their respective analyte can be evaluated on a single chip. The distance between the channels may be further reduced or other design adaptations of the microfluidic chip can be made to allow for analysis of high numbers of samples on a single chip.

A high resolution mapping across the microfluidic channel was performed once with an aperture defined spot-size of $10 \times 10 \mu\text{m}^2$ at the IRIS beamline at the BESSY II synchrotron and once with the IR microscope employed in this thesis with a spot-size of $160 \times 160 \mu\text{m}^2$. At the IRIS beamline a cover glass ($d \approx 50 \mu\text{m}$) has been used as an IR window to enable for a visual control. In both experiments the channel was filled with deionized water.

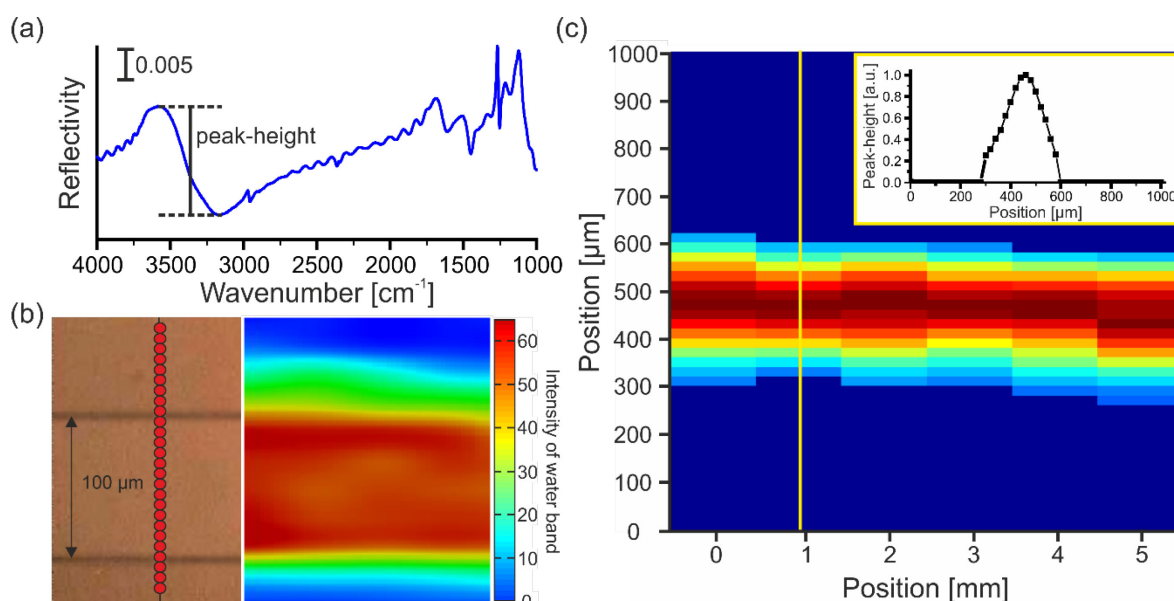


Figure 6-2: Chemical map of microfluidic channel on type I microfluidic chip using the optofluidic platform system. (a) Exemplary IR-spectrum used for evaluation with indication of peak-height as measured quantity. (b) High resolution chemical map recorded with 10 μm spatial resolution at the IRIS Beamline at BESSY II (c) Chemical map along microfluidic channel. Coloring according to peak height of water stretching vibration (3450 cm⁻¹) Inset: Line-scan across 100 μm wide channel recorded with 160 μm spatial resolution and 10 μm step-size along yellow line.

Figure 6-2 shows the results of the performed chemical mappings across and along the channel. From the measurement shown in Figure 6-2 (a) it can be deduced that for application in the Hyperion IR microscope a minimum separation > 300 μm between the channels would be required to ensure that the signal obtained is solely from the channel under investigation.

In principle with a scan along the channel a high temporal resolution in mixing or other reproducible processes as demonstrated *e.g.* by Lendl *et al.*⁵⁷⁻⁵⁹ could be obtained.

The performed experiments show that the optofluidic platform could be used in the future for chemical mapping and for measurements at different positions *i.e.* components of microfluidic chips.

Combination with commercially available microfluidic chips

The detection scheme of the presented optofluidic platform potentially allows to use microfluidic chip of arbitrary material. PDMS based microfluidic chips may be widely used in numerous different research applications and are mainly used in this thesis. On the other hand polymeric materials as *e.g.* poly (methyl methacrylate) (PMMA), polyethylene (PE), cyclic olefin copolymers (COC) or polytetrafluoroethylene (PTFE) may be beneficial for the dissemination of IR spectroscopy for other applications. Microfluidic chips from these material can be produced cost-effectively and are commercially available. The different materials provide different mechanical, physical and chemical properties resulting in *e.g.* compatibility to different solvents, chemical stability or lower thermal expansion. The different chemical structure of these polymers may also allow for less perturbation of the measurements in spectral regions where the absorption of PDMS is high. In particular in the region of (-CH_x) absorption bands (≈3000-2800 cm⁻¹), being of high interest in lipid analysis or in the region where Si-O and Si-O-Si bonds (≈1100-1000 cm⁻¹) may complicate the analysis of fingerprint features.

The possibility for *in situ* measurements on a microfluidic chip fabricated from a material other than PDMS has been investigated with a rhombic chamber microfluidic chip (Figure 6-3). The chip was

fabricated by injection molding with TOPAS[®], a COC polymer, supplied by Microfluidic ChipShop GmbH. The observation window in the experiment was a blank silicon substrate ($d = 0.8$ mm).

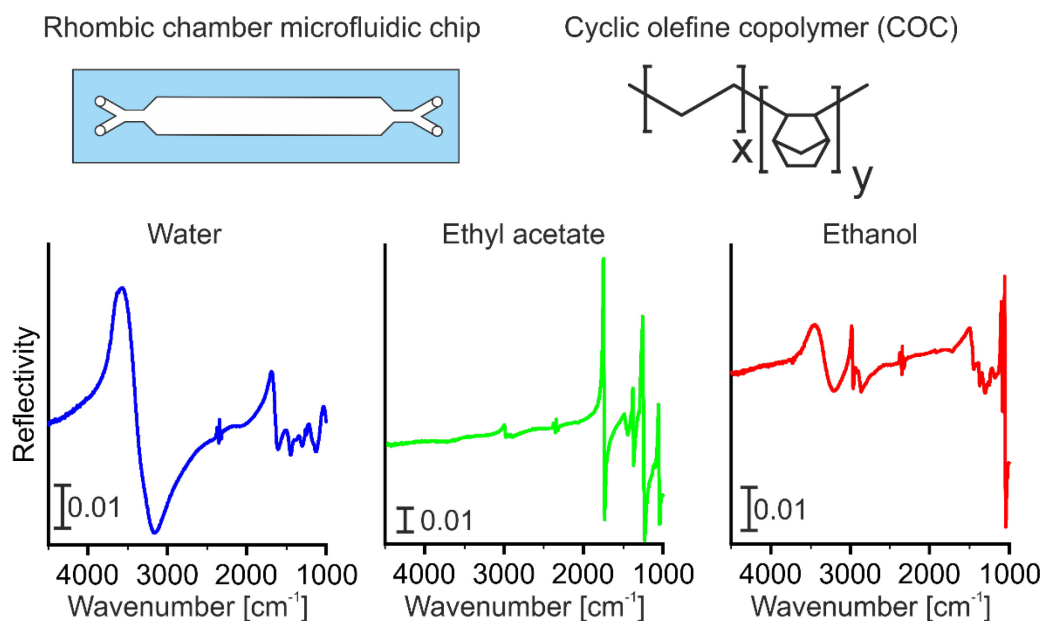


Figure 6-3: Layout of commercially available, rhombic chamber microfluidic chip (TOPAS[®], Microfluidic ChipShop GmbH, (12-0902-0172-02), $d_{\text{channel}} = 500$ μm). Schematic of the general chemical structure of COC polymers and exemplary IR reflectivity spectra of different solvent measured with the optofluidic platform on the TOPAS[®] microfluidic chip at the center of the rhombic chamber.

Three different solvents (water, ethyl acetate and ethanol) commonly applied in the experiments have been exemplary measured in the commercially available microfluidic chip. For all three analyte the characteristic vibrational bands can be identified (Figure 6-3). In addition, the measurements show that presented technique can also be applied to microfluidic channels with differing channel dimensions. It has to be noted that in consequence of the larger channel depth of 500 μm no oscillations connected to the multi-beam interference in the channel can be observed.

The performed experiment demonstrates the possibility to perform *in situ* IR spectroscopy on commercially available microfluidic chips. Even though only TOPAS[®] has been tested as an alternative material, potentially, many other materials can be applied for the fabrication of the microfluidic chip. This may make the optofluidic platform interesting for numerous application as the microfluidic chip material and design does not generally dictate the performance of the system.

***In situ* biosensing and investigation of protein-protein interactions**

The experiment performed in section 4.2.4 showed that the adsorption of streptavidin on a biotinylated enhancement substrate can be investigated and that a characteristic vibrational signature of proteins can be obtained. In principle the surface immobilized streptavidin could be used for the further immobilization of a biotinylated molecule *e.g.* a biotinylated antibody. The biotinylated antibody in turn could be used for target specific binding of another molecule as schematically shown in Figure 6-4. On the one hand this concept could be used for biosensing applications and on the other hand it could be used to study the interactions between the antibody and the target molecule. One of the questions which such an experiment raises is if the enhancement of the enhancement substrate has a sufficiently large spatial extend to detect the binding of the molecules.

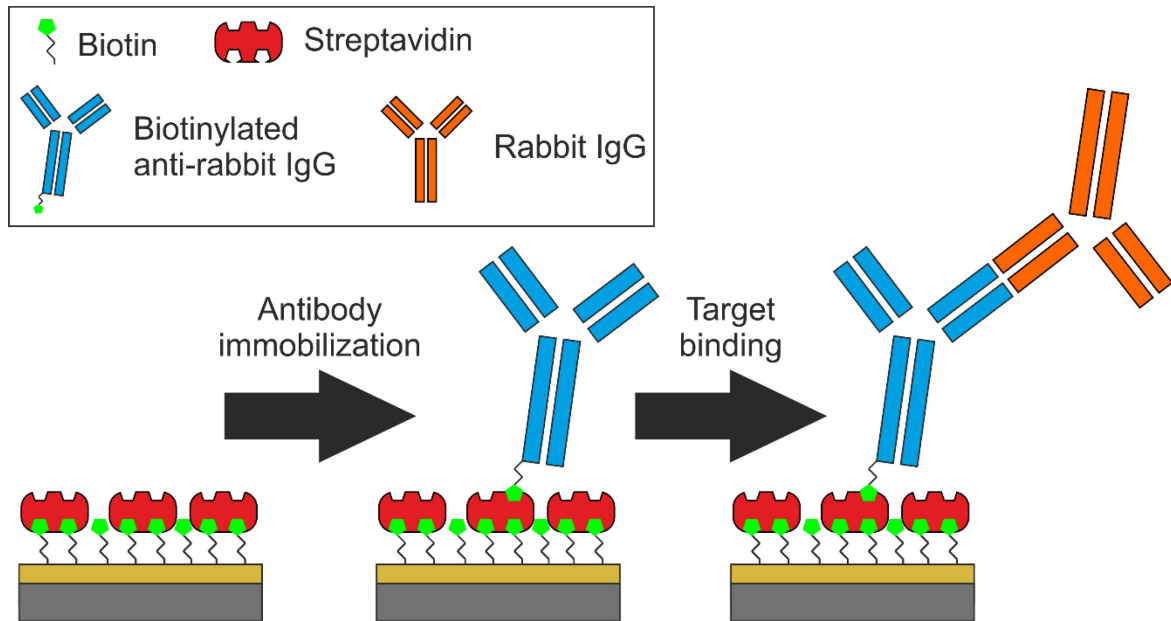


Figure 6-4: Schematic drawing of surface immobilization of a biotinylated antibody and binding of a target molecule on the example of anti-rabbit IgG and rabbit IgG.

The general possibility to perform such experiments has been investigated. A biotinylated enhancement substrate was used for the experiment and subsequently exposed to streptavidin anti-rabbit IgG and rabbit IgG in a PBS buffer solution. After each exposure the sample was rinsed for 2 hours with the pure buffer solution and *in situ* IR spectra were recorded. The obtained spectra were referenced to an initial spectrum of the biotinylated enhancement substrate with pure buffer in the channel (Figure 6-5).

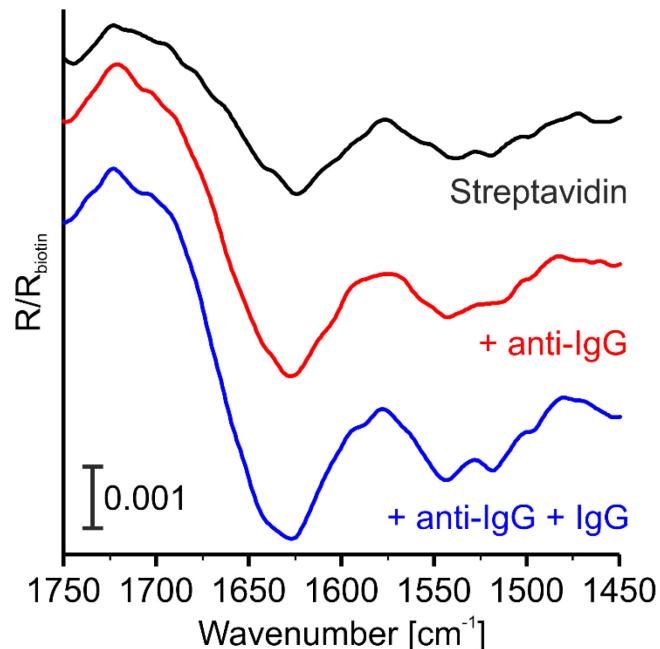


Figure 6-5: In situ SEIRA spectra of a biotinylated enhancement substrate obtained after subsequent exposure to streptavidin (black), anti-rabbit IgG (red) and rabbit IgG (blue). The spectra are shifted for better comparison and have been smoothed using a cubic spline interpolation.

In the *in situ* SEIRA spectra shown in Figure 6-5 an increase in the amplitude of the amide I and amide II bands and changes in the measured vibrational signature could be detected after each exposure

Outlook

step. In order to evaluate the interactions and possibly identify the different molecules by their vibrational signature optical modeling must however be performed. In a simple biosensor which just aims to register a change in the amplitude of the vibrational bands these measurements could be sufficient. However in this case the advantage of using SEIRA spectroscopy would be lost.

The experiment demonstrates that in principle the enhancement provided by the enhancement substrate extends far enough to obtain information on the subsequent binding of molecules using a biotin-streptavidin modified surface. In the future further developments of the optical modeling have to be developed to allow for an analysis of the obtained spectra.

The presented concept of an optofluidic platform offers the possibility to integrate further optical measurement techniques within the same platform. Complementary vibrational spectroscopy techniques as surface enhanced Raman (SERS) or coherent anti-stokes Raman (CARS) but also techniques sensitive to changes in the refractive index as SPR and LSPR sensing or label based techniques as fluorescence spectroscopy could be integrated. Adding these techniques to the optofluidic platform would create a unique multimethod analysis platform and would create a powerful tool with an unmatched information content for further research and applications. In addition also non-optical detection techniques could furthermore be combined with the optofluidic platform in the down-stream analytics as mass spectrometry or nuclear magnetic resonance to even further increase the possibilities of the analysis.

The access to the structural information of proteins and the possibility to investigate changes in this structure in response to external stimuli as well as the possibility to analyze interaction processes between molecules in detail has numerous applications in many fields. In particular the ability to study minute sample volumes fast, label-free and non-destructive will make it an interesting technique in the emerging field of personalized medicine for the analysis of *e.g.* body fluids. The concept could be used in the development of novel strategies for structure-sensitive biosensors enabling to determine the presence and the structure of the protein under investigations. The presented concept can also be of high interest in the search for novel drugs and drug-targets as interactions can be studied in detail which possibly allows one to determine and optimize the drug or the mode of action of a treatment. It could furthermore be used to investigate the underlying interaction processes and mechanisms involved in the progression and development of diseases and to identify potential new targets for treatment or diagnostic.

References

1. Psaltis, D.; Quake, S. R.; Yang, C., Developing optofluidic technology through the fusion of microfluidics and optics. *nature* 2006, 442, 381.
2. Kühn, S.; Phillips, B.; Lunt, E. J.; Hawkins, A.; Schmidt, H., Ultralow power trapping and fluorescence detection of single particles on an optofluidic chip. *Lab on a Chip* 2010, 10, 189-194.
3. Fan, X.; White, I. M., Optofluidic microsystems for chemical and biological analysis. *Nature photonics* 2011, 5, 591-597.
4. Chen, Y.-F.; Jiang, L.; Mancuso, M.; Jain, A.; Oncescu, V.; Erickson, D., Optofluidic opportunities in global health, food, water and energy. *Nanoscale* 2012, 4, 4839-4857.
5. Pang, L.; Chen, H. M.; Freeman, L. M.; Fainman, Y., Optofluidic devices and applications in photonics, sensing and imaging. *Lab on a Chip* 2012, 12, 3543-3551.
6. Minzioni, P.; Osellame, R.; Sada, C.; Zhao, S.; Omenetto, F.; Gylfason, K. B.; Haraldsson, T.; Zhang, Y.; Ozcan, A.; Wax, A., Roadmap for optofluidics. *Journal of Optics* 2017, 19, 093003.
7. Ozcelik, D.; Cai, H.; Leake, K. D.; Hawkins, A. R.; Schmidt, H., Optofluidic bioanalysis: fundamentals and applications. *Nanophotonics* 2017, 6, 647-661.
8. Dukor, R.; Chalmers, J.; Griffiths, P., Handbook of Vibrational Spectroscopy. *Vibrational Spectroscopy in the Detection of Cancer* John Wiley and Sons, New York 2001.
9. Griffiths, P. R.; Chalmers, J. M., *Handbook of vibrational spectroscopy*. J. Wiley.: 2002.
10. Aroca, R., *Surface-enhanced vibrational spectroscopy*. John Wiley & Sons: 2006.
11. Röseler, A.; Korte, E. H., Infrared spectroscopic ellipsometry. *Handbook of vibrational spectroscopy* 2006.
12. White, I. M.; Yazdi, S. H.; Wei, W. Y., Optofluidic SERS: synergizing photonics and microfluidics for chemical and biological analysis. *Microfluid Nanofluid* 2012, 13, 205-216.
13. Yazdi, S. H.; White, I. M., Optofluidic surface enhanced Raman spectroscopy microsystem for sensitive and repeatable on-site detection of chemical contaminants. *Analytical chemistry* 2012, 84, 7992-7998.
14. Oh, Y.-J.; Jeong, K.-H., Optofluidic SERS chip with plasmonic nanoprobe self-aligned along microfluidic channels. *Lab on a Chip* 2014, 14, 865-868.
15. Kauffmann, E.; Darnton, N. C.; Austin, R. H.; Batt, C.; Gerwert, K., Lifetimes of intermediates in the beta-sheet to alpha-helix transition of beta-lactoglobulin by using a diffusional IR mixer. *Proceedings of the National Academy of Sciences of the United States of America* 2001, 98, 6646-6649.
16. Kauffmann, E.; Darnton, N. C.; Austin, R. H.; Batt, C.; Gerwert, K., Lifetimes of intermediates in the β -sheet to α -helix transition of β -lactoglobulin by using a diffusional IR mixer. *Proceedings of the National Academy of Sciences* 2001, 98, 6646-6649.
17. Byler, D. M.; Susi, H., Examination of the secondary structure of proteins by deconvolved FTIR spectra. *Biopolymers* 1986, 25, 469-487.
18. Caughey, B. W.; Dong, A.; Bhat, K. S.; Ernst, D.; Hayes, S. F.; Caughey, W. S., Secondary structure analysis of the scrapie-associated protein PrP 27-30 in water by infrared spectroscopy. *Biochemistry* 1991, 30, 7672-7680.
19. Van Stokkum, I.; Lindsell, H.; Hadden, J.; Haris, P.; Chapman, D.; Bloemendal, M., Temperature-induced changes in protein structures studied by Fourier transform infrared spectroscopy and global analysis. *Biochemistry* 1995, 34, 10508-10518.
20. Ataka, K.; Richter, B.; Heberle, J., Orientational Control of the Physiological Reaction of Cytochrome c Oxidase Tethered to a Gold Electrode. *The Journal of Physical Chemistry B* 2006, 110, 9339-9347.
21. Baldassarre, M.; Li, C.; Eremina, N.; Goormaghtigh, E.; Barth, A., Simultaneous Fitting of Absorption Spectra and Their Second Derivatives for an Improved Analysis of Protein Infrared Spectra. *Molecules* 2015, 20, 12599-12622.
22. Surewicz, W. K.; Mantsch, H. H.; Chapman, D., Determination of protein secondary structure by Fourier transform infrared spectroscopy: a critical assessment. *Biochemistry* 1993, 32, 389-394.

References

23. Wong, P.; Wong, R. K.; Caputo, T. A.; Godwin, T. A.; Rigas, B., Infrared spectroscopy of exfoliated human cervical cells: evidence of extensive structural changes during carcinogenesis. *Proceedings of the National Academy of Sciences* 1991, 88, 10988-10992.
24. Schultz, C. P.; Liu, K.-z.; Johnston, J. B.; Mantsch, H. H., Study of chronic lymphocytic leukemia cells by FT-IR spectroscopy and cluster analysis. *Leukemia research* 1996, 20, 649-655.
25. Holman, H.-Y. N.; Bechtel, H. A.; Hao, Z.; Martin, M. C., Synchrotron IR spectromicroscopy: chemistry of living cells. *Analytical chemistry* 2010, 82, 8757-8765.
26. Marcsisin, E. J. S.; Uttero, C. M.; Miljković, M.; Diem, M., Infrared microspectroscopy of live cells in aqueous media. *Analyst* 2010, 135, 3227-3232.
27. Vaccari, L.; Birarda, G.; Businaro, L.; Pacor, S.; Greci, G., Infrared Microspectroscopy of Live Cells in Microfluidic Devices (MD-IRMS): Toward a Powerful Label-Free Cell-Based Assay. *Analytical Chemistry* 2012, 84, 4768-4775.
28. Vaccari, L.; Birarda, G.; Greci, G.; Pacor, S.; Businaro, L. In *Synchrotron radiation infrared microspectroscopy of single living cells in microfluidic devices: advantages, disadvantages and future perspectives*, Journal of Physics: Conference Series, IOP Publishing: 2012; p 012007.
29. Chan, K. A.; Kazarian, S. G., Aberration-free FTIR spectroscopic imaging of live cells in microfluidic devices. *Analyst* 2013, 138, 4040-4047.
30. Miller, L. M.; Bourassa, M. W.; Smith, R. J., FTIR spectroscopic imaging of protein aggregation in living cells. *Biochimica et Biophysica Acta (BBA) - Biomembranes* 2013, 1828, 2339-2346.
31. Sandt, C.; Frederick, J.; Dumas, P., Profiling pluripotent stem cells and organelles using synchrotron radiation infrared microspectroscopy. *Journal of biophotonics* 2013, 6, 60-72.
32. Baker, M. J.; Trevisan, J.; Bassan, P.; Bhargava, R.; Butler, H. J.; Dorling, K. M.; Fielden, P. R.; Fogarty, S. W.; Fullwood, N. J.; Heys, K. A.; Hughes, C.; Lasch, P.; Martin-Hirsch, P. L.; Obinaju, B.; Sockalingum, G. D.; Sulé-Suso, J.; Strong, R. J.; Walsh, M. J.; Wood, B. R.; Gardner, P.; Martin, F. L., Using Fourier transform IR spectroscopy to analyze biological materials. *Nat. Protocols* 2014, 9, 1771-1791.
33. Birarda, G.; Ravasio, A.; Suryana, M.; Maniam, S.; Holman, H.-Y.; Greci, G., IR-Live: Fabrication of a low-cost plastic microfluidic device for infrared spectromicroscopy of living cells. *Lab on a Chip* 2016.
34. Hinrichs, K.; Gensch, M.; Esser, N., Analysis of organic films and interfacial layers by infrared spectroscopic ellipsometry. *Applied spectroscopy* 2005, 59, 272A-282A.
35. Ionov, L.; Sidorenko, A.; Eichhorn, K.-J.; Stamm, M.; Minko, S.; Hinrichs, K., Stimuli-responsive mixed grafted polymer films with gradually changing properties: direct determination of chemical composition. *Langmuir* 2005, 21, 8711-8716.
36. Mikhaylova, Y.; Ionov, L.; Rappich, J.; Gensch, M.; Esser, N.; Minko, S.; Eichhorn, K.-J.; Stamm, M.; Hinrichs, K., In Situ Infrared Ellipsometric Study of Stimuli-Responsive Mixed Polyelectrolyte Brushes. *Analytical Chemistry* 2007, 79, 7676-7682.
37. Hinrichs, K.; Roseler, A.; Roodenko, K.; Rappich, J., Surface-enhanced infrared absorption: Infrared ellipsometry of an evaporated ultrathin organic films. *Applied Spectroscopy* 2008, 62, 121-124.
38. Rosu, D. M.; Jones, J. C.; Hsu, J. W. P.; Kavanagh, K. L.; Tsankov, D.; Schade, U.; Esser, N.; Hinrichs, K., Molecular Orientation in Octanedithiol and Hexadecanethiol Monolayers on GaAs and Au Measured by Infrared Spectroscopic Ellipsometry. *Langmuir* 2009, 25, 919-923.
39. Angelova, P. N.; Hinrichs, K.; Philipova, I. L.; Kostova, K. V.; Tsankov, D. T., Monolayer Orientation of ω -Substituted Amide-Bridged Alkanethiols on Gold. *The Journal of Physical Chemistry C* 2010, 114, 1253-1259.
40. Hoy, O.; Zdyrko, B.; Lupitsky, R.; Sheparovych, R.; Aulich, D.; Wang, J.; Bittrich, E.; Eichhorn, K. J.; Uhlmann, P.; Hinrichs, K., Synthetic hydrophilic materials with tunable strength and a range of hydrophobic interactions. *Advanced Functional Materials* 2010, 20, 2240-2247.
41. Hinrichs, K.; Levichkova, M.; Wynands, D.; Walzer, K.; Eichhorn, K. J.; Bauerle, P.; Leo, K.; Riede, M., Morphology and molecular orientation of ethyl-substituted dicyanovinyl-sexithiophene films for photovoltaic applications. *Thin Solid Films* 2012, 525, 97-105.

References

42. Hinrichs, K.; Roodenko, K.; Rappich, J.; Chehimi, M. M., Analytical methods for the characterization of aryl layers. *Aryl Diazonium Salts: New Coupling Agents and Surface Science* 2012, 1247.
43. Hinrichs, K., In Situ Infrared Spectroscopy. In *Encyclopedia of Microfluidics and Nanofluidics*, Li, D., Ed. Springer US: Boston, MA, 2013; pp 1-4.
44. Zhang, X.; Tretjakov, A.; Hovestaedt, M.; Sun, G.; Syritski, V.; Reut, J.; Volkmer, R.; Hinrichs, K.; Rappich, J., Electrochemical functionalization of gold and silicon surfaces by a maleimide group as a biosensor for immunological application. *Acta biomaterialia* 2013, 9, 5838-5844.
45. Kanyong, P.; Sun, G.; Rösicke, F.; Syritski, V.; Panne, U.; Hinrichs, K.; Rappich, J., Maleimide functionalized silicon surfaces for biosensing investigated by in-situ IRSE and EQCM. *Electrochemistry Communications* 2015, 51, 103-107.
46. Ayankojo, A. G.; Tretjakov, A.; Reut, J.; Boroznjak, R.; Öpik, A.; Rappich, J. r.; Furchner, A.; Hinrichs, K.; Syritski, V., Molecularly Imprinted Polymer Integrated with a Surface Acoustic Wave Technique for Detection of Sulfamethizole. *Analytical chemistry* 2016, 88, 1476-1484.
47. Kroning, A.; Furchner, A.; Adam, S.; Uhlmann, P.; Hinrichs, K., Probing carbonyl–water hydrogen-bond interactions in thin polyoxazoline brushes. *Biointerphases* 2016, 11, 019005.
48. Rösicke, F.; Sun, G.; Neubert, T.; Janietz, S.; Hinrichs, K.; Rappich, J., Electrochemical functionalization of Au by aminobenzene and 2-aminotoluene. *Journal of Physics: Condensed Matter* 2016, 28, 094004.
49. Furchner, A.; Kroning, A.; Rauch, S.; Uhlmann, P.; Eichhorn, K.-J.; Hinrichs, K., Molecular Interactions and Hydration States of Ultrathin Functional Films at the Solid–Liquid Interface. *Analytical Chemistry* 2017, 89, 3240-3244.
50. Shaykhutdinov, T.; Furchner, A.; Rappich, J.; Hinrichs, K., Mid-infrared nanospectroscopy of Berreman mode and epsilon-near-zero local field confinement in thin films. *Optical Materials Express* 2017, 7, 3706-3714.
51. Badura, A.; Esper, B.; Ataka, K.; Grunwald, C.; Wöll, C.; Kuhlmann, J.; Heberle, J.; Rögner, M., Light - Driven Water Splitting for (Bio -) Hydrogen Production: Photosystem 2 as the Central Part of a Bioelectrochemical Device. *Photochemistry and photobiology* 2006, 82, 1385-1390.
52. Jiang, X.; Zuber, A.; Heberle, J.; Ataka, K., In situ monitoring of the orientated assembly of strep-tagged membrane proteins on the gold surface by surface enhanced infrared absorption spectroscopy. *Physical Chemistry Chemical Physics* 2008, 10, 6381-6387.
53. Perro, A.; Lebourdon, G.; Henry, S.; Lecomte, S.; Servant, L.; Marre, S., Combining microfluidics and FT-IR spectroscopy: towards spatially resolved information on chemical processes. *Reaction Chemistry & Engineering* 2016, 1, 577-594.
54. Kulka, S.; Kaun, N.; Baena, J. R.; Frank, J.; Svasek, P.; Moss, D.; Vellekoop, M. J.; Lendl, B., Mid-IR synchrotron radiation for molecular specific detection in microchip-based analysis systems. *Anal Bioanal Chem* 2004, 378, 1735-1740.
55. Kaun, N.; Kulka, S.; Frank, J.; Schade, U.; Vellekoop, M. J.; Harasek, M.; Lendl, B., Towards biochemical reaction monitoring using FT-IR synchrotron radiation. *Analyst* 2006, 131, 489-494.
56. Schleege, M.; Wagner, C.; Vellekoop, M.; Lendl, B.; Heberle, J., Time-resolved flow-flash FT-IR difference spectroscopy: the kinetics of CO photodissociation from myoglobin revisited. *Anal Bioanal Chem* 2009, 394, 1869-1877.
57. Buchegger, W.; Wagner, C.; Lendl, B.; Kraft, M.; Vellekoop, M., A highly uniform lamination micromixer with wedge shaped inlet channels for time resolved infrared spectroscopy. *Microfluid Nanofluid* 2011, 10, 889-897.
58. Buchegger, W.; Wagner, C.; Svasek, P.; Lendl, B.; Kraft, M.; Vellekoop, M. J., Fabrication and characterization of a vertical lamination micromixer for mid-IR spectroscopy. *Sensors and Actuators B: Chemical* 2011, 159, 336-341.
59. Wagner, C.; Buchegger, W.; Vellekoop, M.; Kraft, M.; Lendl, B., Time-resolved mid-IR spectroscopy of (bio)chemical reactions in solution utilizing a new generation of continuous-flow micro-mixers. *Anal Bioanal Chem* 2011, 400, 2487-2497.

References

60. Polshin, E.; Verbruggen, B.; Witters, D.; Sels, B.; De Vos, D.; Nicolaï, B.; Lammertyn, J., Integration of microfluidics and FT-IR microscopy for label-free study of enzyme kinetics. *Sensors and Actuators B: Chemical* 2014, 196, 175-182.
61. Kazarian, S. G.; Chan, K. L. A., Applications of ATR-FTIR spectroscopic imaging to biomedical samples. *Biochimica et Biophysica Acta (BBA) - Biomembranes* 2006, 1758, 858-867.
62. Kazarian, S., Enhancing high-throughput technology and microfluidics with FTIR spectroscopic imaging. *Anal Bioanal Chem* 2007, 388, 529-532.
63. Chan, K. L. A.; Gulati, S.; Edel, J. B.; de Mello, A. J.; Kazarian, S. G., Chemical imaging of microfluidic flows using ATR-FTIR spectroscopy. *Lab on a Chip* 2009, 9, 2909-2913.
64. Chan, K. A.; Niu, X.; deMello, A.; Kazarian, S., Generation of chemical movies: FT-IR spectroscopic imaging of segmented flows. *Analytical chemistry* 2011, 83, 3606-3609.
65. Chan, K. L. A.; Kazarian, S. G., FT-IR Spectroscopic Imaging of Reactions in Multiphase Flow in Microfluidic Channels. *Analytical Chemistry* 2012, 84, 4052-4056.
66. Osawa, M.; Ikeda, M., SURFACE-ENHANCED INFRARED-ABSORPTION OF PARA-NITROBENZOIC ACID DEPOSITED ON SILVER ISLAND FILMS - CONTRIBUTIONS OF ELECTROMAGNETIC AND CHEMICAL MECHANISMS. *Journal of Physical Chemistry* 1991, 95, 9914-9919.
67. Osawa, M.; Ataka, K.-i., Electromagnetic mechanism of enhanced infrared absorption of molecules adsorbed on metal island films. *Surface science* 1992, 262, L118-L122.
68. Osawa, M.; Ataka, K.; Yoshii, K.; Nishikawa, Y., SURFACE-ENHANCED INFRARED-SPECTROSCOPY - THE ORIGIN OF THE ABSORPTION ENHANCEMENT AND BAND SELECTION RULE IN THE INFRARED-SPECTRA OF MOLECULES ADSORBED ON FINE METAL PARTICLES. *Applied Spectroscopy* 1993, 47, 1497-1502.
69. Osawa, M., Surface-enhanced infrared absorption. In *Near-Field Optics and Surface Plasmon Polaritons*, Springer: 2001; pp 163-187.
70. Röseler, A.; Korte, E.-H., Infrared-Optical Characterization of Metallic Island Films. *Applied Spectroscopy* 1997, 51, 902-904.
71. Röseler, A.; Korte, E.-H., The optical constants of metallic island films as used for surface enhanced infrared absorption. *Thin Solid Films* 1998, 313-314, 732-736.
72. Roseler, A.; Korte, E. H., Surface enhanced infrared absorption observed with attenuated total reflection (ATR-SEIRA): modeling the optical response. *Fresenius Journal of Analytical Chemistry* 1998, 362, 51-57.
73. Korte, E. H.; Roseler, A.; Buskuhl, M., Ellipsometric studies related to surface-enhanced infrared absorption. *Talanta* 2000, 53, 9-16.
74. Ataka, K.; Giess, F.; Knoll, W.; Naumann, R.; Haber-Pohlmeier, S.; Richter, B.; Heberle, J., Oriented attachment and membrane reconstitution of his-tagged cytochrome c oxidase to a gold electrode: In situ monitoring by surface-enhanced infrared absorption spectroscopy. *Journal of the American Chemical Society* 2004, 126, 16199-16206.
75. Ataka, K.; Heberle, J., Biochemical applications of surface-enhanced infrared absorption spectroscopy. *Anal Bioanal Chem* 2007, 388, 47-54.
76. Ataka, K.; Stripp, S. T.; Heberle, J., Surface-enhanced infrared absorption spectroscopy (SEIRAS) to probe monolayers of membrane proteins. *Biochimica et Biophysica Acta (BBA) - Biomembranes* 2013, 1828, 2283-2293.
77. Srajer, J.; Schwaighofer, A.; Ramer, G.; Rotter, S.; Guenay, B.; Kriegner, A.; Knoll, W.; Lendl, B.; Nowak, C., Double-layered nanoparticle stacks for surface enhanced infrared absorption spectroscopy. *Nanoscale* 2014, 6, 127-131.
78. Adato, R.; Yanik, A. A.; Amsden, J. J.; Kaplan, D. L.; Omenetto, F. G.; Hong, M. K.; Erramilli, S.; Altug, H., Ultra-sensitive vibrational spectroscopy of protein monolayers with plasmonic nanoantenna arrays. *Proceedings of the National Academy of Sciences* 2009, 106, 19227-19232.
79. Wu, C. H.; Khanikaev, A. B.; Adato, R.; Arju, N.; Yanik, A. A.; Altug, H.; Shvets, G., Fano-resonant asymmetric metamaterials for ultrasensitive spectroscopy and identification of molecular monolayers. *Nature Materials* 2012, 11, 69-75.

References

80. Cetin, A. E.; Etezadi, D.; Altug, H., Accessible nearfields by nanoantennas on nanopedestals for ultrasensitive vibrational spectroscopy. *Advanced Optical Materials* 2014, 2, 866-872.
81. Adato, R.; Aksu, S.; Altug, H., Engineering mid-infrared nanoantennas for surface enhanced infrared absorption spectroscopy. *Materials Today* 2015, 18, 436-446.
82. Rodrigo, D.; Limaj, O.; Janner, D.; Etezadi, D.; García de Abajo, F. J.; Pruneri, V.; Altug, H., Mid-infrared plasmonic biosensing with graphene. *Science* 2015, 349, 165-168.
83. Limaj, O.; Etezadi, D.; Wittenberg, N. J.; Rodrigo, D.; Yoo, D.; Oh, S.-H.; Altug, H., Infrared Plasmonic Biosensor for Real-Time and Label-Free Monitoring of Lipid Membranes. *Nano Letters* 2016, 16, 1502-1508.
84. Etezadi, D.; Iv, J. B. W.; Ruggeri, F. S.; Dietler, G.; Lashuel, H. A.; Altug, H., Nanoplasmonic mid-infrared biosensor for in vitro protein secondary structure detection. *Light: Science and Applications* 2017, 6.
85. Neubrech, F.; Pucci, A.; Cornelius, T. W.; Karim, S.; García-Etxarri, A.; Aizpurua, J., Resonant plasmonic and vibrational coupling in a tailored nanoantenna for infrared detection. *Physical review letters* 2008, 101, 157403.
86. Neubrech, F.; Pucci, A., Plasmonic enhancement of vibrational excitations in the infrared. *Selected Topics in Quantum Electronics, IEEE Journal of* 2013, 19, 4600809-4600809.
87. Kratz, C.; Furchner, A.; Oates, T. W.; Janasek, D.; Hinrichs, K., Nanoliter Sensing for Infrared Bioanalytics. *ACS sensors* 2018, 3, 299-303.
88. Kratz, C.; Oates, T.; Hinrichs, K., Optimization and quantification of surface enhanced infrared absorption using gradient gold island films. *Thin Solid Films* 2016, 617, 33-37.
89. Stuart, B., *Infrared Spectroscopy: Fundamental and Applications*. John Wiley & Sons, Ltd: 2004.
90. Pradier, C.-M.; Chabal, Y. J., *Biointerface characterization by advanced IR spectroscopy*. Elsevier: 2011.
91. Roeseler, A. *Infrared Spectroscopic Ellipsometry, Akademie-Verlag, Berlin*; ISBN 3-05-500623-2: 1990.
92. Tompkins, H.; Irene, E. A., *Handbook of ellipsometry*. William Andrew: 2005.
93. Azzam, R.; Bashara, N., *Ellipsometry and polarized light*. North-Holland Publishing Company. Amsterdam, New York, Oxford 1977.
94. Furchner, A., *Spectroscopic infrared ellipsometry on functional polymer films*. 2014.
95. Kneipp, K.; Wang, Y.; Kneipp, H.; Perelman, L. T.; Itzkan, I.; Dasari, R. R.; Feld, M. S., Single molecule detection using surface-enhanced Raman scattering (SERS). *Physical review letters* 1997, 78, 1667.
96. Kneipp, K.; Kneipp, H.; Bohr, H. G., Single-molecule SERS spectroscopy. In *Surface-Enhanced Raman Scattering*, Springer: 2006; pp 261-277.
97. Osawa, M., Surface-enhanced infrared absorption. *Near-Field Optics and Surface Plasmon Polaritons* 2001, 81, 163-187.
98. Aroca, R. F.; Ross, D. J.; Domingo, C., Surface-enhanced infrared spectroscopy. *Applied Spectroscopy* 2004, 58, 324A-338A.
99. Neubrech, F.; Beck, S.; Glaser, T.; Hentschel, M.; Giessen, H.; Pucci, A., Spatial Extent of Plasmonic Enhancement of Vibrational Signals in the Infrared. *ACS nano* 2014.
100. Dong, L.; Yang, X.; Zhang, C.; Cerjan, B.; Zhou, L.; Tseng, M. L.; Zhang, Y.; Alabastri, A.; Nordlander, P.; Halas, N. J., Nanogapped Au Antennas for Ultrasensitive Surface-Enhanced Infrared Absorption Spectroscopy. *Nano Letters* 2017, 17, 5768-5774.
101. Adato, R.; Altug, H., In-situ ultra-sensitive infrared absorption spectroscopy of biomolecule interactions in real time with plasmonic nanoantennas. *Nature communications* 2013, 4.
102. Wang, L.-X.; Jiang, X.-E., Bioanalytical Applications of Surface-enhanced Infrared Absorption Spectroscopy. *Chinese Journal of Analytical Chemistry* 2012, 40, 975-982.
103. Chekhun, V. F.; Solyanik, G. I.; Kulik, G. I.; Tryndiak, V. P.; Todor, I. N.; Dovbeshko, G. I.; Repnytska, O. P., The Seira spectroscopy data of nucleic acids and phospholipids from sensitive- and drug-resistant rat tumours. *Journal of Experimental & Clinical Cancer Research* 2002, 21, 599-607.

References

104. Brown, C. W.; Li, Y.; Seelenbinder, J. A.; Pivarnik, P.; Rand, A. G.; Letcher, S. V.; Gregory, O. J.; Platek, M. J., Immunoassays Based on Surface-Enhanced Infrared Absorption Spectroscopy. *Analytical Chemistry* 1998, 70, 2991-2996.
105. Repnytska, O. P.; Dovbeshko, G. I.; Tryndiak, V. P.; Todor, I. M.; Kosenkov, D. V., Structural organisation of nucleic acids from tumour cells. *Faraday Discussions* 2004, 126, 61-76.
106. Hartstein, A.; Kirtley, J. R.; Tsang, J. C., ENHANCEMENT OF THE INFRARED-ABSORPTION FROM MOLECULAR MONOLAYERS WITH THIN METAL OVERLAYERS. *Physical Review Letters* 1980, 45, 201-204.
107. Chen, K.; Duy Dao, T.; Nagao, T., Tunable Nanoantennas for Surface Enhanced Infrared Absorption Spectroscopy by Colloidal Lithography and Post-Fabrication Etching. *Scientific Reports* 2017, 7, 44069.
108. Ataka, K.; Osawa, M., In situ infrared study of water-sulfate coadsorption on gold(111) in sulfuric acid solutions. *Langmuir* 1998, 14, 951-959.
109. Wan, L.-J.; Terashima, M.; Noda, H.; Osawa, M., Molecular Orientation and Ordered Structure of Benzenethiol Adsorbed on Gold(111). *The Journal of Physical Chemistry B* 2000, 104, 3563-3569.
110. Miyake, H.; Ye, S.; Osawa, M., Electroless deposition of gold thin films on silicon for surface-enhanced infrared spectroelectrochemistry. *Electrochemistry Communications* 2002, 4, 973-977.
111. Heaps, D. A.; Griffiths, P. R., Band shapes in the infrared spectra of thin organic films on metal nanoparticles. *Vibrational Spectroscopy* 2006, 42, 45-50.
112. Sinther, M.; Pucci, A.; Otto, A.; Priebe, A.; Diez, S.; Fahsold, G., Enhanced Infrared Absorption of SERS-Active Lines of Ethylene on Cu. *physica status solidi (a)* 2001, 188, 1471-1476.
113. Bjerke, A. E.; Griffiths, P. R.; Theiss, W., Surface-enhanced infrared absorption of CO on platinumized platinum. *Analytical Chemistry* 1999, 71, 1967-1974.
114. Lu, G.-Q.; Sun, S.-G.; Cai, L.-R.; Chen, S.-P.; Tian, Z.-W.; Shiu, K.-K., In situ FTIR spectroscopic studies of adsorption of CO, SCN⁻, and poly (o-phenylenediamine) on electrodes of nanometer thin films of Pt, Pd, and Rh: Abnormal infrared effects (AIREs). *Langmuir* 2000, 16, 778-786.
115. Wang, H.-C.; Sun, S.-G.; Yan, J.-W.; Yang, H.-Z.; Zhou, Z.-Y., In situ STM studies of electrochemical growth of nanostructured Ni films and their anomalous IR properties. *The Journal of Physical Chemistry B* 2005, 109, 4309-4316.
116. Fahsold, G.; Bartel, A.; Krauth, O.; Magg, N.; Pucci, A., Infrared optical properties of ultrathin Fe films on MgO(001) beyond the percolation threshold. *Physical Review B* 2000, 61, 14108-14113.
117. Krauth, O.; Fahsold, G.; Magg, N.; Pucci, A., Anomalous infrared transmission of adsorbates on ultrathin metal films: Fano effect near the percolation threshold. *The Journal of Chemical Physics* 2000, 113, 6330-6333.
118. Enders, D.; Nagao, T.; Pucci, A.; Nakayama, T., Reversible adsorption of Au nanoparticles on SiO₂/Si: An in situ ATR-IR study. *Surface Science* 2006, 600, L71-L75.
119. Enders, D.; Rupp, S.; Küller, A.; Pucci, A., Surface enhanced infrared absorption on Au nanoparticle films deposited on SiO₂/Si for optical biosensing: Detection of the antibody-antigen reaction. *Surface Science* 2006, 600, L305-L308.
120. Noguez, C., Surface plasmons on metal nanoparticles: the influence of shape and physical environment. *The Journal of Physical Chemistry C* 2007, 111, 3806-3819.
121. Petryayeva, E.; Krull, U. J., Localized surface plasmon resonance: Nanostructures, bioassays and biosensing—A review. *Analytica Chimica Acta* 2011, 706, 8-24.
122. Hergert, W.; Wriedt, T., *The Mie Theory: basics and applications*. Springer: 2012; Vol. 169.
123. Draine, B. T.; Flatau, P. J., Discrete-dipole approximation for scattering calculations. *JOSA A* 1994, 11, 1491-1499.
124. Mogensen, K. B.; Kneipp, K., Size-Dependent Shifts of Plasmon Resonance in Silver Nanoparticle Films Using Controlled Dissolution: Monitoring the Onset of Surface Screening Effects. *The Journal of Physical Chemistry C* 2014, 118, 28075-28083.
125. Xiang, H.; Zhang, X.; Neuhauser, D.; Lu, G., Size-dependent plasmonic resonances from large-scale quantum simulations. *The journal of physical chemistry letters* 2014, 5, 1163-1169.

References

126. Willets, K. A.; Van Duyne, R. P., Localized surface plasmon resonance spectroscopy and sensing. *Annu. Rev. Phys. Chem.* 2007, 58, 267-297.
127. Mayer, K. M.; Hafner, J. H., Localized surface plasmon resonance sensors. *Chemical reviews* 2011, 111, 3828-3857.
128. Brolo, A. G., Plasmonics for future biosensors. *Nature Photonics* 2012, 6, 709.
129. Granqvist, C.; Hunderi, O., Conductivity of inhomogeneous materials: Effective-medium theory with dipole-dipole interaction. *Physical Review B* 1978, 18, 1554.
130. Gkogkou, D.; Shaykhutdinov, T.; Oates, T. W.; Gernert, U.; Schreiber, B.; Facsko, S.; Hildebrandt, P.; Weidinger, I. M.; Esser, N.; Hinrichs, K., Characterization of anisotropically shaped silver nanoparticle arrays via spectroscopic ellipsometry supported by numerical optical modeling. *Applied Surface Science* 2017, 421, 460-464.
131. Su, K. H.; Wei, Q. H.; Zhang, X.; Mock, J. J.; Smith, D. R.; Schultz, S., Interparticle Coupling Effects on Plasmon Resonances of Nanogold Particles. *Nano Letters* 2003, 3, 1087-1090.
132. Venables, J., *Introduction to surface and thin film processes*. Cambridge University Press: 2000.
133. Ohring, M., *Materials science of thin films*. Elsevier: 2001.
134. Schwartzkopf, M.; Buffet, A.; Körstgens, V.; Metwalli, E.; Schlage, K.; Benecke, G.; Perlich, J.; Rawolle, M.; Rothkirch, A.; Heidmann, B., From atoms to layers: in situ gold cluster growth kinetics during sputter deposition. *Nanoscale* 2013, 5, 5053-5062.
135. Bergman, D. J.; Stroud, D., Physical properties of macroscopically inhomogeneous media. *Solid state physics* 1992, 46, 147-269.
136. Priebe, A.; Sinther, M.; Fahsold, G.; Pucci, A., The correlation between film thickness and adsorbate line shape in surface enhanced infrared absorption. *The Journal of Chemical Physics* 2003, 119, 4887-4890.
137. Fano, U., Effects of configuration interaction on intensities and phase shifts. *Physical Review* 1961, 124, 1866.
138. Luk'yanchuk, B.; Zheludev, N. I.; Maier, S. A.; Halas, N. J.; Nordlander, P.; Giessen, H.; Chong, C. T., The Fano resonance in plasmonic nanostructures and metamaterials. *Nature materials* 2010, 9, 707.
139. Ross, D.; Aroca, R., Effective medium theories in surface enhanced infrared spectroscopy: The pentacene example. *The Journal of Chemical Physics* 2002, 117, 8095-8103.
140. Norrman, S.; Andersson, T.; Granqvist, C.; Hunderi, O., Optical properties of discontinuous gold films. *Physical Review B* 1978, 18, 674.
141. Andersson, T., The initial growth of vapour deposited gold films. *Gold Bull* 1982, 15, 7-18.
142. Granqvist, C.; Hunderi, O., Optical properties of ultrafine gold particles. *Physical Review B* 1977, 16, 3513.
143. Jackson, J. D., *Classical electrodynamics*. John Wiley & Sons: 2007.
144. Li, H., Refractive index of alkaline earth halides and its wavelength and temperature derivatives. *Journal of Physical and Chemical Reference Data* 1980, 9, 161-290.
145. Chandler-Horowitz, D.; Amirtharaj, P. M., High-accuracy, midinfrared (450 cm⁻¹ ≤ ω ≤ 4000 cm⁻¹) refractive index values of silicon. *Journal of Applied physics* 2005, 97, 123526.
146. Schubert, M., *Infrared Ellipsometry on semiconductor layer structures: Phonons, Plasmons, and Polaritons*. Springer Science & Business Media: 2004.
147. Oates, T.; Wormeester, H.; Arwin, H., Characterization of plasmonic effects in thin films and metamaterials using spectroscopic ellipsometry. *Progress in Surface Science* 2011, 86, 328-376.
148. Jackson, J. D., *Electrodynamics*. Wiley Online Library: 1975.
149. Garnett, J. C. M., Colours in Metal Glasses and in Metallic Films. *Philosophical Transactions of the Royal Society of London. Series A, Containing Papers of a Mathematical or Physical Character* 1904, 203, 385-420.
150. Bruggeman, D. A. G., Berechnung verschiedener physikalischer Konstanten von heterogenen Substanzen. I. Dielektrizitätskonstanten und Leitfähigkeiten der Mischkörper aus isotropen Substanzen. *Annalen der Physik* 1935, 416, 636-664.
151. Niklasson, G. A.; Granqvist, C. G., Optical Properties and Solar Selectivity of Coevaporated Co-Al₂O₃ Composite Films. *Journal of Applied Physics* 1984, 55, 3382-3410.

References

152. Eagen, C. F., Nature of the enhanced optical absorption of dye-coated Ag island films. *Applied Optics* 1981, 20, 3035-3042.
153. Stoner, E. C., XCVII. The demagnetizing factors for ellipsoids. *Philosophical Magazine* 1945, 36, 803-821.
154. Rakic, A. D.; Djurišić, A. B.; Elazar, J. M.; Majewski, M. L., Optical properties of metallic films for vertical-cavity optoelectronic devices. *Applied optics* 1998, 37, 5271-5283.
155. Tolstoy, V. P.; Chernyshova, I.; Skryshevsky, V. A., *Handbook of infrared spectroscopy of ultrathin films*. John Wiley & Sons: 2003.
156. Schwartz, D. K., Mechanisms and kinetics of self-assembled monolayer formation. *Annual Review of Physical Chemistry* 2001, 52, 107-137.
157. Love, J. C.; Estroff, L. A.; Kriebel, J. K.; Nuzzo, R. G.; Whitesides, G. M., Self-assembled monolayers of thiolates on metals as a form of nanotechnology. *Chemical reviews* 2005, 105, 1103-1170.
158. Sabatani, E.; Cohen-Boulakia, J.; Bruening, M.; Rubinstein, I., Thioaromatic monolayers on gold: a new family of self-assembling monolayers. *Langmuir* 1993, 9, 2974-2981.
159. Prats-Alfonso, E.; Albericio, F., Functionalization of gold surfaces: recent developments and applications. *J Mater Sci* 2011, 46, 7643-7648.
160. Mizutani, F., Biosensors utilizing monolayers on electrode surfaces. *Sensors and Actuators B: Chemical* 2008, 130, 14-20.
161. Hoa, X. D.; Kirk, A. G.; Tabrizian, M., Towards integrated and sensitive surface plasmon resonance biosensors: A review of recent progress. *Biosensors and Bioelectronics* 2007, 23, 151-160.
162. Frasconi, M.; Mazzei, F.; Ferri, T., Protein immobilization at gold-thiol surfaces and potential for biosensing. *Anal Bioanal Chem* 2010, 398, 1545-1564.
163. Bain, C. D.; Biebuyck, H. A.; Whitesides, G. M., Comparison of self-assembled monolayers on gold: coadsorption of thiols and disulfides. *Langmuir* 1989, 5, 723-727.
164. Zharnikov, M.; Grunze, M., Spectroscopic characterization of thiol-derived self-assembling monolayers. *Journal of Physics-Condensed Matter* 2001, 13, 11333-11365.
165. Masel, R. I., *Principles of adsorption and reaction on solid surfaces*. John Wiley & Sons: 1996; Vol. 3.
166. Bieri, M.; Bürgi, T., Adsorption kinetics of L-glutathione on gold and structural changes during self-assembly: an in situ ATR-IR and QCM study. *Physical Chemistry Chemical Physics* 2006, 8, 513-520.
167. Brunauer, S.; Emmett, P. H.; Teller, E., Adsorption of gases in multimolecular layers. *Journal of the American chemical society* 1938, 60, 309-319.
168. Norde, W.; Lyklema, J., Thermodynamics of protein adsorption. Theory with special reference to the adsorption of human plasma albumin and bovine pancreas ribonuclease at polystyrene surfaces. *Journal of Colloid and Interface Science* 1979, 71, 350-366.
169. Rabe, M.; Verdes, D.; Seeger, S., Understanding protein adsorption phenomena at solid surfaces. *Advances in Colloid and Interface Science* 2011, 162, 87-106.
170. Sánchez-Varretti, F. O.; García, G. D.; Ramirez-Pastor, A. J., Modeling multilayer adsorption of interacting polyatomic species on heterogeneous surfaces. *Physica A: Statistical Mechanics and its Applications* 2012, 391, 1158-1171.
171. Foo, K. Y.; Hameed, B. H., Insights into the modeling of adsorption isotherm systems. *Chemical Engineering Journal* 2010, 156, 2-10.
172. Rösicke, F.; Gluba, M. A.; Shaykhutdinov, T.; Sun, G.; Kratz, C.; Rappich, J.; Hinrichs, K.; Nickel, N. H., Functionalization of any substrate using covalently modified large area CVD graphene. *Chemical Communications* 2017.
173. Rösicke, F.; Gluba, M. A.; Hinrichs, K.; Sun, G.; Nickel, N. H.; Rappich, J., Quantifying the electrochemical maleimidation of large area graphene. *Electrochemistry Communications* 2015, 57, 52-55.
174. Rösicke, F., Elektrochemische Funktionalisierung von großflächigem CVD-Graphen: Transfer, Charakterisierung und Anwendung. 2017.
175. Whitesides, G. M., The origins and the future of microfluidics. *Nature* 2006, 442, 368.

References

176. Tian, W.-C.; Finehout, E., *Microfluidics for biological applications*. Springer Science & Business Media: 2009; Vol. 16.
177. Berthier, J.; Silberzan, P., *Microfluidics for biotechnology*. Artech House: 2010.
178. Mark, D.; Haeberle, S.; Roth, G.; von Stetten, F.; Zengerle, R., Microfluidic lab-on-a-chip platforms: requirements, characteristics and applications. *Chemical Society Reviews* 2010, 39, 1153-1182.
179. Khademhosseini, A.; Demirci, U.; Langer, R., *Microfluidic technologies for human health*. World Scientific: 2012.
180. Tu, Q.; Pang, L.; Zhang, Y.; Yuan, M.; Wang, J.; Wang, D.; Liu, W.; Wang, J., Microfluidic Device: A Miniaturized Platform for Chemical Reactions. *Chinese Journal of Chemistry* 2013, 31, 304-316.
181. TermehYousefi, A.; Bagheri, S.; Adib, N., Integration of biosensors based on microfluidic: a review. *Sensor Review* 2015, 35, 190-199.
182. and, Y. X.; Whitesides, G. M., SOFT LITHOGRAPHY. *Annual Review of Materials Science* 1998, 28, 153-184.
183. Anderson, J. R.; Chiu, D. T.; Wu, H.; Schueller, O.; Whitesides, G. M., Fabrication of microfluidic systems in poly (dimethylsiloxane). *Electrophoresis* 2000, 21, 27-40.
184. Song, Y.; Cheng, D.; Zhao, L., *Microfluidics: Fundamentals, Devices, and Applications*. John Wiley & Sons: 2018.
185. Hinsmann, P.; Frank, J.; Svasek, P.; Harasek, M.; Lendl, B., Design, simulation and application of a new micromixing device for time resolved infrared spectroscopy of chemical reactions in solution. *Lab on a Chip* 2001, 1, 16-21.
186. Hinsmann, P.; Haberkorn, M.; Frank, J.; Svasek, P.; Harasek, M.; Lendl, B., Time-resolved FT-IR spectroscopy of chemical reactions in solution by fast diffusion-based mixing in a micromachined flow cell. *Applied Spectroscopy* 2001, 55, 241-251.
187. Kazarian, S. G.; Chan, K., Micro-and macro-attenuated total reflection Fourier transform infrared spectroscopic imaging. *Applied spectroscopy* 2010, 64, 135A-152A.
188. Janasek, D.; Hinrichs, K.; Kratz, C.; Oates, T. W. H. Vorrichtung zur Detektion und Charakterisierung von organischen Molekülen in einem flüssigen Probenvolumen. 21.01.2016, 2016.
189. Gauglitz, G.; Brecht, A.; Kraus, G.; Mahm, W., Chemical and biochemical sensors based on interferometry at thin (multi-) layers. *Sensors and Actuators B: Chemical* 1993, 11, 21-27.
190. Gauglitz, G., Direct optical sensors: principles and selected applications. *Anal Bioanal Chem* 2005, 381, 141-155.
191. Leopold, N.; Busche, S.; Gauglitz, G.; Lendl, B., IR absorption and reflectometric interference spectroscopy (RIFS) combined to a new sensing approach for gas analytes absorbed into thin polymer films. *Spectrochimica Acta Part A: Molecular and Biomolecular Spectroscopy* 2009, 72, 994-999.
192. Schkolnik, G.; Salewski, J.; Millo, D.; Zebger, I.; Franzen, S.; Hildebrandt, P., Vibrational Stark effect of the electric-field reporter 4-mercaptobenzonitrile as a tool for investigating electrostatics at electrode/SAM/solution interfaces. *International journal of molecular sciences* 2012, 13, 7466-7482.
193. Lautenschlager, P.; Garriga, M.; Vina, L.; Cardona, M., Temperature dependence of the dielectric function and interband critical points in silicon. *Physical Review B* 1987, 36, 4821.
194. Wormeester, H.; Kooij, E. S.; Poelsema, B., Effective dielectric response of nanostructured layers. *Physica Status Solidi a-Applications and Materials Science* 2008, 205, 756-763.
195. Sönnichsen, C.; Franzl, T.; Wilk, T.; Von Plessen, G.; Feldmann, J., Plasmon resonances in large noble-metal clusters. *New Journal of Physics* 2002, 4, 93.
196. Wartewig, S., *IR and Raman spectroscopy: fundamental processing*. John Wiley & Sons: 2006.
197. Shimanouchi, T., Tables of Molecular Vibrational Frequencies Part 5. *Journal of Physical and Chemical Reference Data* 1972, 1, 189-216.
198. Jensen, T.; Van Duyne, R.; Johnson, S.; Maroni, V., Surface-enhanced infrared spectroscopy: a comparison of metal island films with discrete and nondiscrete surface plasmons. *Applied Spectroscopy* 2000, 54, 371-377.

References

199. Polubotko, A., Dipole-Quadrupole Theory of Surface Enhanced Infrared Absorption and Appearance of Forbidden Lines in the SEIRA Spectra of Symmetrical Molecules. *arXiv preprint arXiv:1204.1652* 2012.
200. Gunde, M. K., Vibrational modes in amorphous silicon dioxide. *Physica B: Condensed Matter* 2000, 292, 286-295.
201. Fang, C.; Zhou, X., Voltammetry and EQCM investigation of glutathione monolayer and its complexation with Cu²⁺. *Electroanalysis* 2003, 15, 1632-1638.
202. Rai, V.; Srivastava, A.; Mukherjee, C.; Deb, S., Localized surface plasmon resonance and refractive index sensitivity of vacuum-evaporated nanostructured gold thin films. *Indian Journal of Physics* 2016, 90, 107-116.
203. Hiroo, T.; Hakuai, I., The Reaction Rate of the Alkaline Hydrolysis of Ethyl Acetate. *Bulletin of the Chemical Society of Japan* 1966, 39, 1837-1842.
204. Herzig-Marx, R.; Queeney, K. T.; Jackman, R. J.; Schmidt, M. A.; Jensen, K. F., Infrared Spectroscopy for Chemically Specific Sensing in Silicon-Based Microreactors. *Analytical Chemistry* 2004, 76, 6476-6483.
205. Qian, W.; Krimm, S., Vibrational analysis of glutathione. 1994.
206. Picquart, M.; Grajcar, L.; Baron, M. H.; Abedinzadeh, Z., Vibrational spectroscopic study of glutathione complexation in aqueous solutions. *Biospectroscopy* 1999, 5, 328-337.
207. Bieri, M.; Bürgi, T., L-Glutathione Chemisorption on Gold and Acid/Base Induced Structural Changes: A PM-IRRAS and Time-Resolved in Situ ATR-IR Spectroscopic Study. *Langmuir* 2005, 21, 1354-1363.
208. Singh, G.; Dogra, S. D.; Kaur, S.; Tripathi, S. K.; Prakash, S.; Rai, B.; Saini, G. S. S., Structure and vibrations of glutathione studied by vibrational spectroscopy and density functional theory. *Spectrochimica Acta Part A: Molecular and Biomolecular Spectroscopy* 2015, 149, 505-515.
209. Aureau, D.; Ozanam, F.; Allongue, P.; Chazalviel, J.-N., The titration of carboxyl-terminated monolayers revisited: In situ calibrated Fourier transform infrared study of well-defined monolayers on silicon. *Langmuir* 2008, 24, 9440-9448.
210. Lapin, N. A.; Chabal, Y. J., Infrared characterization of biotinylated silicon oxide surfaces, surface stability, and specific attachment of streptavidin. *The Journal of Physical Chemistry B* 2009, 113, 8776-8783.
211. Weber, P. C.; Ohlendorf, D.; Wendoloski, J.; Salemme, F., Structural origins of high-affinity biotin binding to streptavidin. *Science* 1989, 243, 85-88.
212. Diamandis, E. P.; Christopoulos, T. K., The biotin-(strept)avidin system: principles and applications in biotechnology. *Clinical Chemistry* 1991, 37, 625-636.
213. Dundas, C. M.; Demonte, D.; Park, S., Streptavidin-biotin technology: improvements and innovations in chemical and biological applications. *Applied Microbiology and Biotechnology* 2013, 97, 9343-9353.
214. Peluso, P.; Wilson, D. S.; Do, D.; Tran, H.; Venkatasubbaiah, M.; Quincy, D.; Heidecker, B.; Poindexter, K.; Tolani, N.; Phelan, M., Optimizing antibody immobilization strategies for the construction of protein microarrays. *Analytical biochemistry* 2003, 312, 113-124.
215. Venyaminov, S. Y.; Kalnin, N., Quantitative IR spectrophotometry of peptide compounds in water (H₂O) solutions. II. Amide absorption bands of polypeptides and fibrous proteins in α -, β -, and random coil conformations. *Biopolymers* 1990, 30, 1259-1271.
216. Förch, R.; Schönherr, H.; Schonherr, H.; Jenkins, A. T. A., *Surface design: applications in bioscience and nanotechnology*. John Wiley & Sons: 2009.
217. Zeng, S.; Yong, K.-T.; Roy, I.; Dinh, X.-Q.; Yu, X.; Luan, F., A review on functionalized gold nanoparticles for biosensing applications. *Plasmonics* 2011, 6, 491.
218. Holzinger, M.; Le Goff, A.; Cosnier, S. Nanomaterials for biosensing applications: a review *Front Chem* [Online], 2014, p. 63. PubMed. (accessed 2014).
219. Georgakilas, V.; Otyepka, M.; Bourlinos, A. B.; Chandra, V.; Kim, N.; Kemp, K. C.; Hobza, P.; Zboril, R.; Kim, K. S., Functionalization of graphene: covalent and non-covalent approaches, derivatives and applications. *Chemical reviews* 2012, 112, 6156-6214.

References

220. Kuila, T.; Bose, S.; Mishra, A. K.; Khanra, P.; Kim, N. H.; Lee, J. H., Chemical functionalization of graphene and its applications. *Progress in Materials Science* 2012, 57, 1061-1105.
221. Liu, J.; Tang, J.; Gooding, J. J., Strategies for chemical modification of graphene and applications of chemically modified graphene. *Journal of Materials Chemistry* 2012, 22, 12435-12452.
222. Rösicke, F.; Gluba, M. A.; Shaykhutdinov, T.; Sun, G.; Kratz, C.; Rappich, J.; Hinrichs, K.; Nickel, N. H., Functionalization of any substrate using covalently modified large area CVD graphene. *Chemical Communications* 2017, 53, 9308-9311.
223. Kanagaraja, S.; Alaeddine, S.; Eriksson, C.; Lausmaa, J.; Tengvall, P.; Wennerberg, A.; Nygren, H., Surface characterization, protein adsorption, and initial cell–surface reactions on glutathione and 3-mercapto-1,2,-propanediol immobilized to gold. *Journal of Biomedical Materials Research* 1999, 46, 582-591.
224. Hinrichs, K.; Shaykhutdinov, T.; Kratz, C.; Rösicke, F.; Schöniger, C.; Arenz, C.; Nickel, N. H.; Rappich, J., Electrochemical Modification of Large Area Graphene and Characterization by Vibrational Spectroscopy. In *Encyclopedia of Interfacial Chemistry*, Wandelt, K., Ed. Elsevier: Oxford, 2018; pp 80-94.
225. Atkins, P. W.; De Paula, J.; Ralf, L.; Appelhagen, A., *Kurzlehrbuch Physikalische Chemie*. Wiley-VCH Weinheim: 2008; Vol. 3.
226. Lee, J. K.; Kim, Y.-G.; Chi, Y. S.; Yun, W. S.; Choi, I. S., Grafting Nitrilotriacetic Groups onto Carboxylic Acid-Terminated Self-Assembled Monolayers on Gold Surfaces for Immobilization of Histidine-Tagged Proteins. *The Journal of Physical Chemistry B* 2004, 108, 7665-7673.
227. Gkogkou, D. Anisotropic plasmonic nanoparticle arrays for surface-enhanced biosensors. Technical University Berlin, 2017.

List of abbreviations

4-MBN	4-mercaptobenzonitrile
4-NBM	(4-nitrobenzyl) mercaptane
4-MBA	4-mercaptobenzoic acid
AFM	Atomic force microscopy
ATR	Attenuated total internal reflection
CaF ₂	Calcium difluoride
COC	cyclic olefin copolymer
CVD	Chemical vapor deposition
EF	Enhancement factor
EM	Electro magnetic
EMA	Effective medium approximation
FEM	Finite element method
FT-IR	Fourier transform infrared
GSH	Glutathione
IgG	Immunoglobulin G
IR	Infrared
LOC	Lab-on-Chip
LOD	Limit of detection
LOD _m	Limit of detection mass
LSPR	Localized surface plasmon resonance
SAM	Self-assembled monolayer
SEIRA	Surface enhanced infrared absorption
SEM	Scanning electron microscopy
SERS	Surface enhanced Raman scattering
SiC	Silicon Carbide
SPR	Surface plasmon resonance
PDMS	Polydimethylsiloxane
PE	Polyethylene
PMMA	Poly(methyl methacrylate)
p-MP	Para-(maleimidophenyl)
PTFE	Polytetrafluoroethylene
UTHI	Ureido (tetrahydroimidizalone) tetrahydrothiophene
UV-Vis	Ultraviolet to visible spectral range

List of figures

1. Motivation: In situ μ-IR spectroscopy	Page
Figure 1-1: General concept of an optofluidic platform for enhanced IR spectroscopy.....	2
Figure 2-1: Schematic drawing of a FT-IR-microscope using a Cassegrain objective for light focusing..	6
Figure 2-2: Measurement principle of recording relative or referenced reflectivity spectra. (top left) Intensity spectrum recorded on a reference silicon substrate. (bottom left) Intensity spectrum measured on gold island film substrate with an organic SAM of 4-mercaptobenzonitrile. (right) Resulting relative or referenced reflectivity spectrum.	7
Figure 2-3: Different states of polarizations of an EM wave expressed by its decomposition in E_s and E_p field components, depending on amplitude-ratio E_{p0}/E_{s0} and phase difference ($\Delta = \delta_p - \delta_s$).	8
Figure 2-4: Basic principle of ellipsometric measurement. Reflection at an interface changes the polarization state of light in dependence on the dielectric properties ϵ and geometry e.g. film thickness of the sample. Adapted from [34]	9
Figure 2-5: Schematic setup of an ellipsometer with a PSCA configuration. The incidence angle of the radiation on the sample is denoted by φ	10
Figure 2-6: Extinction cross-section of Mie scattering for a single spherical gold nano particle. (a) Extinction cross section for different radii of the gold nano particle. (b) Extinction cross section of a 65 nm gold nanoparticle with different surrounding media. (Calculated by MiePlot v4.5 @Philip Laven).	12
Figure 2-7: Dependence of the extinction cross-section of Mie scattering of a single gold nanoparticle on the thickness of a homogeneous layer with $n_{\text{layer}} = 1.5$ coating the nanoparticle. (a) Extinction coefficient for a single gold sphere ($r=65$ nm) with varying coating thickness d . (b) Shift of maximum position of the plasmonic resonance in dependence on film thickness for gold spheres with $r = 55$ nm and $r = 65$ nm. λ_{max} was determined by fitting of a Gaussian curve to the spectrum. (Calculated with MiePlot v4.5 @Philip Laven).	13
Figure 2-8: Schematics of evaporator setup	15
Figure 2-9: Schematic of emission profile of the electron beam evaporator	15
Figure 2-10: Measured distribution of effective film thickness in the area of the substrate holder. The effective film thickness of the gold island film was determined by UV-Vis ellipsometry using bulk optical constants from literature for the materials in a 3-layer model of Si/SiO ₂ /gold.....	16
Figure 2-11: Schematic of realizable types of enhancement substrates depending on positioning within the emission cone of the evaporator.	16
Figure 2-12: Schematic of different types of enhancement substrates realizable on observation windows for the optofluidic platform. Dashed line in the graph of gold-layer thickness indicates percolation threshold.	17
Figure 2-13 Changes in the line shape of vibrational bands in SEIRA spectroscopy in dependence of the morphology of the gold island film on the example of a 4-mercaptobenzonitrile SAM on a gradient gold island film substrate. (a) IR microscopic reflection spectra obtained by a line scan along the gradient substrate. A measurement on a silicon substrate was used as a reference. (b) Baseline corrected zoom into the region of the vibrational band of the stretching vibration of the C≡N-group of 4-MBN. The spectra were baseline corrected using a linear baseline and shifted for a better comparison. (c) Baseline corrected zoom into the region of the vibrational band of the combined stretching and deformation vibration of the phenylene ring of 4-MBN. The spectra were baseline corrected using a linear baseline and shifted for a better comparison.	18

List of figures

Figure 2-14: Peak-amplitudes of exemplary vibrational band measured in IR microscope (Cassegrain objective, angle of incidence 17.125°) on metal island film (left) and simulated on bulk gold for an angle of incidence of 17.13° for the $\nu(\text{C}\equiv\text{N})$ vibrational mode of 4-Mercaptobenzonitrile.	19
Figure 2-15: Schematic drawing of enlarged surface area of a metal island in comparison to flat gold surface.	20
Figure 2-16: Schematic layer-model representation of a sample with two layers on a substrate for the optical modeling of measurements in reflection geometry.	22
Figure 2-17: Schematic of multi-beam interference in layered structure.	23
Figure 2-18: Schematic of the optical model employed in the calculation of reflectance spectra. The gold island film is therein described by a uniaxial film.	23
Figure 2-19: Optical properties of metal-island film determined by FEM calculation from SEM image converted with a spatial resolution of 1 nm. (a) Near-field E-field density map for s-polarized light. (b) Nearfield E-field density map for p-polarized light. (c) Far-field spectrum calculated for simplified structures in the region of the SiO_2 -vibrational band. FEM simulations were performed by Timur Shaykhutdinov.	25
Figure 2-20: Schematic representation of an oblate spheroid used in the model to describe the individual adsorbate coated metal island.	27
Figure 2-21: Imaginary part of the pseudo-dielectric function of exemplary gold island film on silicon substrate with fixed fill-factor f , length of major and minor axis of gold islands and variation of the adsorbate layer thickness.	28
Figure 2-22: Schematic drawing of a substrate surface functionalized with a SAM.	29
Figure 2-23: SAM formation following a first order Langmuir adsorption model.	30
Figure 2-24: Schematic of preparation and transfer of functionalized graphene to the enhancement substrate.	32
Figure 2-25: Schematic top and cross section view of the employed microfluidic chips and channels. Type I: Microfluidic chip with four straight channels (dimensions 42 mm x 0.1 mm x 0.037 mm (L x w x d). Type II: Microfluidic chip with T-junction.	33
Figure 2-26: General scheme of master-replica fabrication method for microfluidic chips.	33
Figure 2-27: Simulation of flow-velocity distribution in the vicinity of the inlet of the microfluidic chip of type I with a volume flow rate of 0.2 ml/h at the inlet. (Left inset) Flow velocity profile in 2 mm distance from the inlet. (Right inset) Zoom in the transition zone between the inlet and the microfluidic channel.	34
Figure 3-1: Schematic drawing of optofluidic platform. (a) Assembly drawing of optofluidic platform. (b) Cross-sectional view of optofluidic platform. Inset: Zoom on detection layer.	37
Figure 3-2: Dependence of measurement spot-size on focus depth. Assumed spot diameter $160\ \mu\text{m}$ in air, thickness of substrate 0.8 mm, refractive index of IR window $n_{\text{Silicon}} = 3.42$	38
Figure 3-3: Measurement area on microfluidic channel during <i>in situ</i> measurements with the optofluidic platform marked in green and indication of defining dimensions used for the calculation.	38
Figure 3-4: Exemplary IR microscopic reflectivity spectra of a microfluidic channel filled with acetonitrile (left) and water (right).	39
Figure 3-5: <i>In situ</i> SEIRA microscopic reflectivity spectrum of a 4-MBN monolayer on a gold island film in ethanol recorded with the optofluidic flow cell and indication of vibrational bands associated with the SAM.	40
Figure 4-1: Gold island film with gradient thickness of gold. (a) Thickness map along the gradient substrate measured with (■) AFM and (●) fitted effective thickness from UV-Vis ellipsometry. (b) Exemplary SEM pictures recorded along the gradient (2mm step size). The shown SEM images were	

recorded by Dr. Dimitra Gkogkou at the ZELMI – Zentraleinrichtung Elektronenmikroskopie at the Technische Universität Berlin. Reprinted with permission from Ref. [88].	43
Figure 4-2: Thickness dependent evolution of the real $\langle \epsilon_1 \rangle$ and imaginary $\langle \epsilon_2 \rangle$ component of the pseudo-dielectric function from bare substrate to gold-film. Indicated thickness values of the solid lines are effective thicknesses determined by UV-Vis ellipsometry. Light grey lines show the development in steps of 2 nm increase in effective film thickness. Reprinted with permission from Ref. [88].	44
Figure 4-3: IR microscopic reflectance spectra recorded along a gradient substrate. Colored spectra correspond to effective dielectric function in Figure 4-2.	45
Figure 4-4: Evaluation of SEIRA activity of gradient island film substrate. (a) Schematic setup of IR measurements with a SAM of 4-MBN on a gold island film. (b) IR-microscope reflection spectra of unmodified and modified gradient substrate at position of maximum SEIRA activity. (c) Baseline corrected IR-microscope reflection spectra of MBN film on gradient substrate with maximum SEIRA enhancement with identification of central frequencies of vibrational bands of 4-MBN. Baseline correction was performed using a “rubber-band” method. ¹⁹⁶ For better comparison the spectrum in the spectral range of the native oxide band (dashed box) was scaled down by a factor of 10. Reprinted with permission from Ref. [88].	46
Figure 4-5: SEIRA activity quantified by measured band amplitude of the nitrile vibrational band $\nu(\text{C}\equiv\text{N})$ of a SAM of 4-MBN in dependency of film thickness. Adapted from Ref. [88].	47
Figure 4-6: Normalized peak-intensity of vibrational modes of $\nu(\text{C}\equiv\text{N})$ of 4-MBN (red dots) and vibrational band of the native oxide (black squares). Reprinted with permission from Ref. [88].	49
Figure 4-7: Position dependent enhancement on a gradient gold island film at four different positions along the gradient. (black) Spectra recorded prior to SAM deposition and (red) spectra recorded after SAM deposition	49
Figure 4-8: Molecular structure of and IR microscopic SEIRA spectra of (a) 4-MBN and (b) 4-MBA with indication of the vibrational bands used for the analysis.	50
Figure 4-9: Normalized peak amplitude of molecular vibrations of 4-MBN after and of the native oxide vibration before SAM formation in dependence of the measurement position on three different gradient substrates. The colors of the symbols correspond to the indication of the vibrational bands in Figure 4-8.	51
Figure 4-10: Normalized peak amplitude of molecular vibrations of 4-MBA after and of the native oxide vibration before SAM formation in dependence of the measurement position on three different gradient substrates. The colors of the symbols correspond to the indication of the vibrational bands in Figure 4-8.	51
Figure 4-11: Correlation between the amplitude of the vibrational band of the native oxide before the deposition of the SAM and the ring vibration of (▪) 4-MBN around 1579 cm^{-1} and (●) 4-MBA around 1583 cm^{-1} of the SAMs.	52
Figure 4-12: Correlation between the enhancement of the vibrational bands of 4-MBN and the enhancement of the vibrational signature of the native oxide	52
Figure 4-13: Formation of 4-MBN SAM on contaminated gold island film substrate. SEIRA spectra of the enhancement substrate before (—) and after (—) deposition of 4-MBN SAM from solution.	54
Figure 4-14: Formation of GSH SAM on a contaminated gold island film substrate. SEIRA spectra of the enhancement substrate before (—) and after (—) deposition of 4-MBN SAM from solution. Spectra were smoothed using a cubic spline interpolation.	55
Figure 4-15: Shift of in the resonance of gold island films upon absorption of different SAMs. (—) Measurement before SAM deposition (—) measurement after SAM deposition. (left column) real part $\langle \epsilon_1 \rangle$ of pseudo-dielectric function; (middle column) imaginary part $\langle \epsilon_2 \rangle$ of pseudo-dielectric function; (right column) corresponding IR reflectivity spectra.	57

Figure 4-16: $\Delta\lambda$ in dependence of the initially observed resonance wavelength λ_0 for the three investigated SAMs. Dashed lines correspond to linear fit of the data.....	58
Figure 4-17: Simulation of SEIRA spectra using EMA model. (a) Fit of ellipsometric measurement of 4-MBN SAM on gold ($d_{\text{gold}} = 200$ nm). The ellipsometric measurement was performed at 65° incidence angle. (b) Measured and simulated IR reflectivity spectra of 4-MBN SAM on gold island film substrate. (c) Measured and simulated IR reflectivity spectra of 4-MBN SAM baseline corrected using simulation of gold island film substrate without oscillators as baseline.	60
Figure 4-18: Simulation of IR reflectivity spectra of different island film morphologies. (a) Measured (full lines) and simulated (dashed lines) IR reflectivity spectra measured at different positions on a GSH modified gradient gold island film substrate. (b) Zoom into region of CH_x stretching vibrations.	61
Figure 4-19: Schematic of the ethyl acetate hydrolysis reaction	63
Figure 4-20: Schematic of employed microfluidic chip. Inlet 1 (0.1 ml/h) and 3 (0.1 ml/h) were used for the delivery of sodium hydroxide solution and ethyl acetate was supplied via Inlet 2 (0.2 ml/h). The measurement position was chosen approx. 1 cm after the T-junction to ensure for sufficient mixing.	63
Figure 4-21: <i>In situ</i> monitoring of ethyl acetate hydrolysis. (a) Exemplary IR reflectivity spectra recorded during the experiment at the start (black line), the end (green line) and at 3 time points in between (red, blue and pink lines). The vibrational bands monitored for the analysis are indicated. (b) Time dependent development of the peak amplitude of the $\nu(\text{OH})$ (blue), $\nu(\text{C}=\text{O})$ (red) and $\nu(\text{H}_3\text{C}-\text{C}=\text{O})$ (green) vibrational bands.	64
Figure 4-22: <i>In situ</i> IR spectra recorded on the microfluidic chip of pure ethyl (blue), the mixture after the flow was stopped (green) and at the end of the measurement (red). Respective vibrational bands of ethyl acetate and the educts of the reaction are indicated color-coded in the spectra.	64
Figure 4-23: <i>In situ</i> monitoring of 4-MBN SAM formation from 1 mM solution of 4-MBN in ethanol. (a) Fitted peak-amplitude of the stretching ν (ring) (\blacksquare) and the combined stretching and deformation vibration $\nu+\delta$ (ring) (\bullet) of 4-MBN during monolayer formation. (b) Exemplary <i>in situ</i> IR spectra corresponding to marked points in (a). Spectra are shifted for better comparison.....	67
Figure 4-24: <i>In situ</i> IR monitoring of GSH monolayer formation in microfluidic flow cell. (a) Peak amplitude of amide II vibrational band during monolayer formation and fit of an exponential function corresponding to Langmuir-type adsorption (red line). (b) Exemplary <i>in situ</i> IR spectra corresponding to marked points in (a). Spectra are shifted for better comparison. Reprinted with permission from Ref. [87].....	69
Figure 4-25: pH dependent dissociation and protonation of carboxylic groups of GSH monolayer. (a) Schematic of the reaction of carboxylic group in response to environmental pH changes. (b) <i>In situ</i> IR microscopy spectra at pH 5 (—), pH 10 (—) and pH 2 (—). All spectra are referenced to a spectrum at pH 5. Reprinted with permission from Ref. [87].....	71
Figure 4-26: Time dependent measurement of protonation reaction of the carboxylic ions in the monolayer of GSH. (left) Time dependence of fitted peak amplitudes of the vibrational bands of the carboxylic group $\nu(\text{COOH})$ (\blacktriangle), the asymmetric stretching vibration $\nu_{\text{as}}(\text{COO}^-)$ (\bullet) and the symmetric stretching vibration $\nu_{\text{s}}(\text{COO}^-)$ (\blacksquare) of the carboxylic ion. (Right) Differential IR microscopy spectra recorded during the protonation of the carboxylic ion, corresponding in color to the points marked in the left graph.....	72
Figure 4-27: <i>In situ</i> IR monitoring of streptavidin adsorption on biotinylated surface with the optofluidic platform. (a) Time dependence of integrated peak area amide I vibrational band during adsorption (b) <i>In situ</i> IR spectra at exemplary time points during streptavidin adsorption. Spectra are shifted for better comparison and smoothed using a cubic spline interpolation. Reprinted with permission from Ref. [87]	73

Figure 4-28: General scheme of introducing surface functionalization to an enhancement substrate by transfer of pre-functionalized graphene.	75
Figure 4-29: Enhancement properties of gradient gold island film substrate before and after transfer of functionalized graphene. (a) Exemplary baseline corrected IR microscopy reflection spectra of the native oxide vibrational band before transfer of graphene. (b) Exemplary baseline corrected IR microscopy reflection spectra of the native oxide vibrational band after transfer of graphene and $\nu(\text{C}=\text{O})$ of the p-MP functionalization. (c) Mediated enhancement along gradient substrate for the native oxide band before (■) / after (●) transfer of graphene and for the $\nu(\text{C}=\text{O})$ vibration (▲) of the functionalization.....	76
Figure 4-30: Plasmonic properties of enhancement template measured before and after graphene transfer. Exemplarily shown for the position of maximum enhancement before (black) and after (blue) transfer of the p-MP functionalized graphene. The resulting shift of λ_{max} is indicated as $\Delta\lambda$	77
Figure 4-31: Dependence of the shift of the central wavelength of the plasmonic resonance on the thickness of adsorbed layer. (a) Imaginary part $\langle\epsilon_2\rangle$ of the pseudo-dielectric function of metal island film close to the percolation threshold with adsorbate layer thickness of 0 nm, 5 nm and 7.5 nm (calculated using the optical model introduced in chapter 2.4.4 with exemplary parameters: $a=28.35$ nm, $c=9.7$ nm, $f=0.12$, $n_{\text{coating}}=1.5$, $n_{\text{Si}}=3.42$). (b) $\Delta\lambda$ of resonance in dependence on adsorbate layer thickness.....	78
Figure 4-32: Binding of GSH to p-MP graphene functionalized gold island film. Baseline corrected IR microscope spectrum of p-MP surface (a) before binding of GSH and (b) after binding of GSH. (c) Difference spectrum of bound GSH with indication of observed vibrational modes.	79
Figure 4-33 Pseudo-dielectric function of the sensor substrate before (black) and after (blue) transfer of the functionalized graphene and after exposure of the sensor substrate to GSH (red)	80
Figure 4-34: Schematic of double sided gradient gold island film substrate with one gradient functionalized with p-MP graphene and schematic of the obtained enhancement profiles.	81
Figure 4-35: Baseline corrected <i>ex situ</i> IR-microscope reflection spectra of p-MP graphene functionalized metal island film before (black) and after (red) exposure to 4-NBM solution.....	82
Figure 4-36: <i>In situ</i> monitoring of 4-NBM absorption process. Normalized peak amplitude of $\nu_{\text{as}}(\text{NO}_2)$ of unfunctionalized gold island film (red diamonds) and on p-MP graphene functionalized gold island film (blue hexagons). Adapted and reprinted with permission from Ref. [224]	82
Figure 6-1 Accessible measurement area of optofluidic platform. Exemplary IR reflectivity spectra recorded on a Type I microfluidic chip. Channels contain different analyts as indicated in the corresponding spectra.....	91
Figure 6-2: Chemical map of microfluidic channel on type I microfluidic chip using the optofluidic platform system. (a) Exemplary IR-spectrum used for evaluation with indication of peak-height as measured quantity. (b) High resolution chemical map recorded with 10 μm spatial resolution at the IRIS Beamline at BESSY II (c) Chemical map along microfluidic channel. Coloring according to peak height of water stretching vibration (3450 cm^{-1}) Inset: Line-scan across 100 μm wide channel recorded with 160 μm spatial resolution and 10 μm step-size along yellow line.	92
Figure 6-3: Layout of commercially available, rhombic chamber microfluidic chip (TOPAS®, Microfluidic ChipShop GmbH, (12-0902-0172-02), $d_{\text{channel}} = 500\text{ }\mu\text{m}$). Schematic of the general chemical structure of COC polymers and exemplary IR reflectivity spectra of different solvent measured with the optofluidic platform on the TOPAS® microfluidic chip at the center of the rhombic chamber.....	93
Figure 6-4: Schematic drawing of surface immobilization of a biotinylated antibody and binding of a target molecule on the example of anti-rabbit IgG and rabbit IgG.....	94

List of figures

Figure 6-5: In situ SEIRA spectra of a biotinylated enhancement substrate obtained after subsequent exposure to streptavidin (black), anti-rabbit IgG (red) and rabbit IgG (blue). The spectra are shifted for better comparison and have been smoothed using a cubic spline interpolation..... 94

List of tables

Table 4-1: Integrated area of vibrational bands of the contamination before and after deposition of the 4-MBN SAM.....	54
Table 4-2: Integrated area of vibrational bands of the contamination before and after deposition of the GSH monolayer on gold island film substrate.....	55
Table 4-3: Oscillator parameters of harmonic oscillator model representing the averaged properties of a 4-MBN SAM on gold. The parameters were determined by optical modeling of IR ellipsometry data using SpectraRay3 (Sentech Instruments GmbH)	59
Table 4-4: Parameters of oscillators in the region between 3000 cm^{-1} - 2800 cm^{-1} . Values where determined by a best fit to the measurement data of measurement #2 (see Figure 4-18).....	60
Table 4-5: Resulting EMA parameters of the optical simulation of different morphologies of gold islands films on a single gradient substrate.	61

List of chemicals

		Purchased from
4-mercaptobenzoic acid	99%	Sigma-Aldrich
4-mercaptobenzonitrile	purity 95%	Synchem UG & Co. KG
(4-nitrobenzyl) mercaptane	purity 95%	Sigma-Aldrich
Acetonitrile	for DNA synthesis, 99.9%	Merck KGaA
Anti-rabbit immunoglobulin G	(whole molecule)–Peroxidase antibody produced in goat, MW: 42 kDa	Sigma-Aldrich
Biotin-SAM formation reagent Kit		Dojindo Molecular Technologies Inc.
Dimethyl sulfoxide	Anhydrous 99.9%	Sigma-Aldrich
Ethanol	Emsure® absolute for analysis	Merck KGaA
Ethyl acetate	LiChrosolv® for spectroscopy >99.8%	Merck KGaA
Glutathione	L-Glutathione reduced ≥98.0%)	Sigma-Aldrich
Gold	99.99% purity	EVOCHEM GmbH
Hydrochloric acid	Suprapur®, 30%	Merck KGaA
Hydrogen peroxide	Hydrogen peroxide solution Green Alternative contains inhibitor, 30 wt. % in H ₂ O, ACS reagent	Sigma-Aldrich
Phosphate buffered saline	Tablet, pH 7.4	Sigma-Aldrich
Polydimethylsiloxane and curer	Sylgard® 184	Dow Corning Corp.
Sodium hydroxide	≥ 99%	Carl Roth GmbH + Co. KG
Streptavidin	from Streptomyces avidinii, essentially salt-free, lyophilized powder, ≥13 units/mg protein	Sigma-Aldrich
Sulfuric acid	Emsure®, ACS, ISO, 95-97%	Merck KGaA
Rabbit immunoglobulin G	IgG from rabbit serum, reagent grade, ≥95% (SDS-PAGE)	Sigma-Aldrich

Acknowledgements

First of all I want to express my sincere gratitude and thanks to my supervisor PD Dr. Karsten Hinrichs for his grate support at all times during my PhD work. Without his guidance, help and trust in me and my work this thesis would not have been possible. It has been highly inspiring to work with him and his way of thinking has greatly influenced myself.

I want to thank Prof Dr. Norbert Esser for the opportunity to conduct my research at the ISAS and for reviewing this work. I also want to thank Prof. Dr. Joachim Heberle from the physics department of the Freie Universität for agreeing to review this thesis. Furthermore I also want to thank Prof. Dr. Peter Hildebrandt for accepting to be the head of the committee.

Many thanks go to Dr. Tom W. H. Oates who was a great supervisor and is a good friend who introduced me to the idea of surface enhancement substrates and made the start in the thesis so much better. I also want to thank Dr. Dirk Janasek from the ISAS in Dortmund for his support with the microfluidics in the project. Without the two of them and their vast knowledge it would not have been possible to realize the work performed in this thesis.

I also want to thank the members of the In situ IR spectroscopy group at the ISAS. Dr. Andreas Furchner for the many interesting discussion we had during our coffee breaks and the experiments we conducted together. Özgür Savas and Illona Engler for their technical support and their patience with me. And the rest of the team Timur Shaykhutdinov, Dr. Guoguang Sun and Dr. Cordula Walder for their help and the good working atmosphere.

Many thanks also go to my scientific partner in crime Dr. Dimitra Gkogkou with whom I had and have the honor to work with. I also want to express my gratitude to the team at the ISAS workshop for their work in manufacturing the components. Furthermore I want to thank Dr. Jörg Rappich and Dr. Felix Rösicke from the Helmholtz Zentrum Berlin for their work and help in the cooperation concerning the functionalization and transfer of the functionalized graphene.

I deeply want to thank my wonderful family, especially my wife and also my two children who are the most inspiring and supporting team I could have wished for and without whom I could not be who I am. They were always there for me to show me that there is a life besides science and that one can be both a family father and a scientist. I also want to thank my parents for supporting me throughout the whole pursuit of becoming a scientist.

Statement of authorship

This doctoral thesis has been submitted for the degree of Doctor rerum naturalium to the Fakultät II— Mathematik und Naturwissenschaften of the Technischen Universität Berlin. I hereby declare, that the thesis has been composed by myself and describes my own work, unless stated otherwise in the text. All references have been quoted, and all sources of information have been specifically acknowledged. The thesis does not contain work extracted from a thesis, dissertation, or research paper previously presented for another degree at this or any other university. I have prepared this thesis specifically for the degree of Dr. rer. nat., while under supervision of PD Dr. Karsten Hinrichs at the Leibniz-Institut für Analytische Wissenschaften – ISAS – e. V. between March 2014 and August 2018.

Place, Date

Christoph Andreas Kratz